

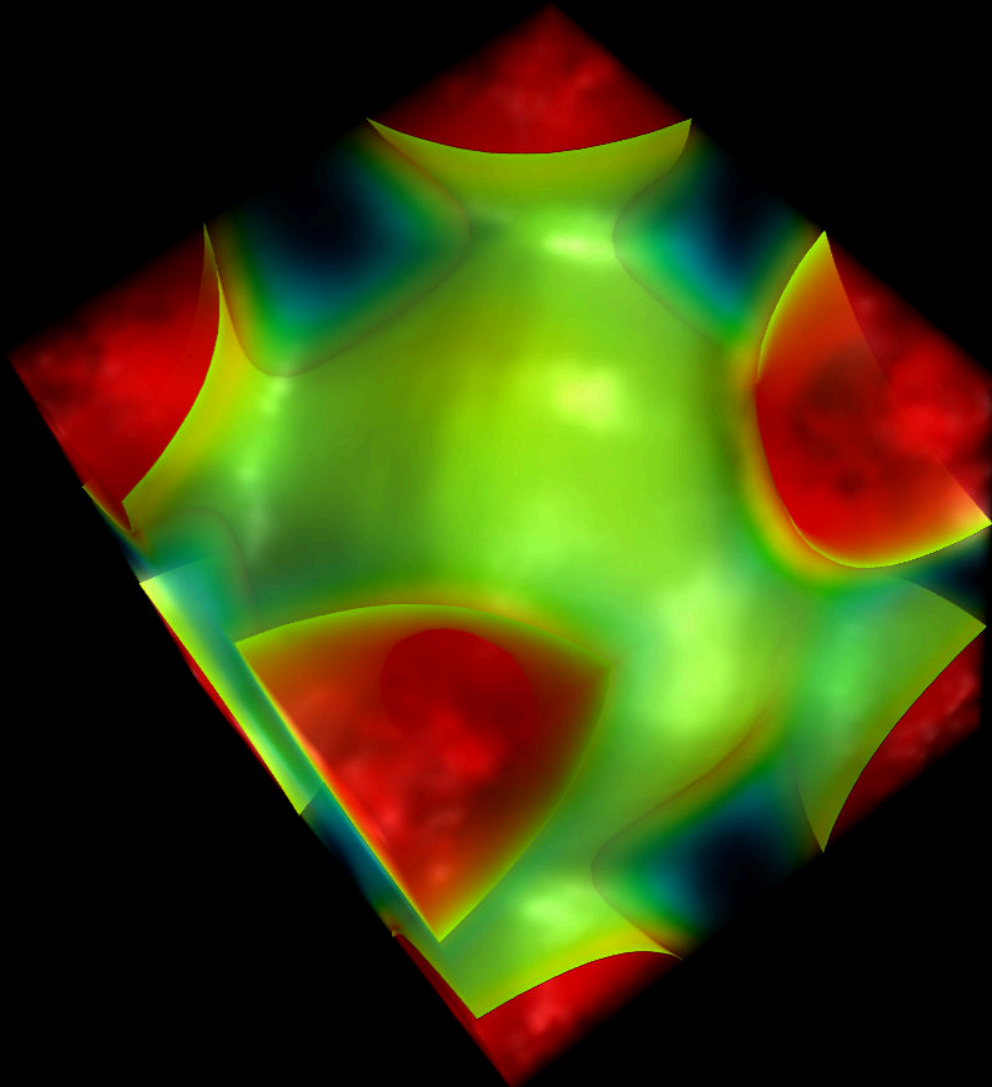


**Physics Department**

Research Area

Strongly Correlated Electron Systems

**Annual Report 2011 / 2012**



**Title image:** 3D-reconstruction of the Fermi-surface of Cu from five 2D-projections obtained by the measurement of the angular correlation (ACAR) of the positron-electron annihilation radiation. Courtesy of Josef Weber, see contribution on the electronic structure of Cu measured with the new 2D-ACAR spectrometer on page 29.



# **Annual Report 2011 / 2012**

## **of the Research Area**

### **Strongly Correlated Electron Systems**

#### **Annual Report 2011/2012**

of the Research Area Strongly Correlated Electron Systems  
(formerly Institute E21)

Chair for Neutron Scattering: Prof. Dr. Peter Böni  
Group for Magnetic Materials: Prof. Dr. Christian Pfleiderer

Technische Universität München  
Physics Department  
James-Franck-Straße 1  
85748 Garching bei München  
Germany

Date of Issue: April 2013  
Editor: Tobias Weber

© Technische Universität München, 2013  
The copyrights of all individual articles remain with their respective authors.



# Contents

<b>Preface</b>	<b>1</b>
<b>1 Magnetism and Superconductivity</b>	<b>3</b>
Rotating Skyrmion Lattices by Spin Torques & Field or Temperature Gradients . . . . .	5
Fluctuation-Induced First-Order Phase Transition In DM-Helimagnets . . . . .	6
Phase Diagram of MnSi Inferred from Magnetization and ac Susceptibility . . . . .	7
Coherent Helimagnons and Gilbert Damping in an Itinerant Magnet . . . . .	8
First Order Metamagnetic Transition in Ho <sub>2</sub> Ti <sub>2</sub> O <sub>7</sub> Observed by Vibrating Coil Magnetometry at Milli-Kelvin Temperatures . . . . .	9
Vibrating-Coil Magnetometry of the Spin Liquid Properties of Tb <sub>2</sub> Ti <sub>2</sub> O <sub>7</sub> . . . . .	10
Emergent Electrodynamics of Skyrmions in a Chiral Magnet . . . . .	11
Direct Manipulation of the Uncompensated Antiferromagnetic Spins in Exchange Coupled System by GeV Ion Irradiation . . . . .	12
Symmetric Magnetization Reversal in Polycrystalline Exchange Coupled Systems via Simultaneous Processes of Coherent Rotation and Domain Nucleation . . . . .	13
Biofunctionalized Magnetic FePt Nanoparticles . . . . .	14
Investigating Bragg Peaks and Heavy-Fermions Using Spin Torque . . . . .	15
Time Resolved Stroboscopic Neutron Scattering of Vortex Lattice Dynamics in Superconducting Niobium	16
Long-Range Crystalline Nature of the Skyrmion Lattice in MnSi . . . . .	17
Long-Wavelength Helimagnetic Order and Skyrmion Lattice Phase in Cu <sub>2</sub> OSeO <sub>3</sub> . . . . .	18
<b>2 Nuclear and Fundamental Physics</b>	<b>21</b>
$\beta$ -Emitter Bremsstrahlung in $\gamma$ -Spectroscopy . . . . .	23
<b>3 Positron Physics</b>	<b>25</b>
A Precise Measurement of the Decay Rate of the Negative Positronium Ion Ps <sup>-</sup> . . . . .	27
Temperature Dependent 2D-ACAR Measurements on Cr . . . . .	28
The Electronic Structure of Cu Measured with the New 2D-ACAR Spectrometer . . . . .	29
High-Intensity Source of Moderated Positrons Using a Brilliant $\gamma$ -Beam . . . . .	30
Quantum Confinement of Positrons in Au Clusters . . . . .	31
Thin Film Alloying Studied by CDBS with the NEPOMUC Positron Beam . . . . .	32
<b>4 Radiography and Tomography</b>	<b>33</b>
Scatter Correction Method by Temporal Primary Modulation in X-ray CT . . . . .	35
Neutron Depolarisation Imaging: Stress Measurements by Magnetostriction Effects in Ni Foils . . . . .	36
Application of Neutron Radiography to Study Material Processes during Hypothetical Severe Accidents in Nuclear Reactors . . . . .	37
Advances in High-Resolution Neutron Computed Tomography . . . . .	38
Laboratory Simulations of Tensile Fracture Development in a Volcanic Conduit via Cyclic Magma Pressurisation . . . . .	39
<b>5 Instrument Development</b>	<b>41</b>
Triple-Axis Option of MIRA . . . . .	43
Tests of Modulated Intensity Small Angle Scattering in Time of Flight Mode . . . . .	44
The Instrument Design of KOMPASS – the New, Polarized TAS at FRM II . . . . .	45
Polarisation Devices for the Spin-Echo Spectrometer RESEDA . . . . .	46
The Upgrade of the Neutron Induced Positron Source NEPOMUC . . . . .	47
Monte-Carlo Simulations for the Optimisation of a TOF-MIEZE Instrument . . . . .	48
Study of a Focusing, Low-Background Neutron Delivery System . . . . .	49

Wavelength Frame Multiplication Chopper System for a Multi-Purpose Imaging Beamline at the European Spallation Source . . . . .	50
<b>6 Activities</b>	<b>51</b>
Lectures, Courses and Seminars . . . . .	53
Publications . . . . .	56
Conferences, Workshops and Seminar Contributions . . . . .	60
Seminar “Neutronen in Industrie und Forschung” 2011 . . . . .	68
Seminar “Neutronen in Industrie und Forschung” 2012 . . . . .	69
Services to the Community . . . . .	70
Accomplished Ph.D. Theses . . . . .	71
Accomplished Master’s and Diploma Theses . . . . .	71
Accomplished Bachelor’s Theses . . . . .	71
Accomplished Term Papers . . . . .	72
Accomplished Extended Essays / “Facharbeiten” . . . . .	72
Accomplished “Zulassungsarbeiten” . . . . .	72
E21 Members . . . . .	73
Secretary . . . . .	73
Professors . . . . .	73
Scientists . . . . .	73
PhD Students . . . . .	73
Students . . . . .	74
Technical Personnel . . . . .	74
Guests . . . . .	74
Professors Emeriti . . . . .	74
Alumni . . . . .	75
Facilities . . . . .	75
FRM II Instruments . . . . .	75
E21 Laboratories . . . . .	75
Group Photo . . . . .	76

# Preface

In the name of all members of the Institute on Strongly Correlated Electron Systems (formerly Institute E21) at the Physik-Department of the Technical University of Munich we are pleased to present the biannual report 2011/12 highlighting some of the exciting research performed during the last two years. Our research concentrated mostly on the effects of strong correlations in magnetic and superconducting materials and on technical developments for our beam lines at the neutron source FRM II as well as our crystal growth and low temperature laboratories.

In our scientific studies we succeeded to achieve again several major breakthroughs. As in the years before the non-centrosymmetric B20 compounds provided thereby a “drosophila” comprising the observation of giant spin torque effects and the identification of a fluctuation-induced first-order phase transition as predicted by Brasovskii over 25 years ago. As part of the projects funded by the Collaborative Transregional Research Network (TRR 80) we succeeded to install a new beam line for ACAR (angular correlation of the annihilation radiation) by the positron group at NEPOMUC that allows us to determine the momentum density of the electrons even in multicomponent materials and at high temperature. ACAR will provide complementary information to interpret the results from our bulk and microscopic techniques. In addition, we conducted first in-situ reflectivity measurements of the preparation of magnetic monolayers using polarized neutrons at the beamline REFSANS at FRM II.

Despite these successes our neutron scattering studies were somewhat constrained by the long-planned shutdown of FRM II in 2011, which was efficiently used to upgrade the beamlines of our institute. At the positron facility NEPOMUC the beam tube and the inserted positron source were exchanged due to the burn-up of the gamma producing cadmium cap. The new source has a longer live time and the positron beams are again operational with even higher quality. The diffractometer MIRA 2 is now equipped with a graphite analyser making high resolution cold triple-axis spectroscopy from small samples possible. The primary spectrometer of RESEDA could be improved greatly by moving the velocity selector from the TREFF monochromator shielding to its own housing. Moreover, the installation of a new generation of RF-coils offers now Larmor diffraction at RESEDA providing an unprecedented momentum resolution. In addition, members of our institute actively contributed to design studies for future beam lines at the European Spallation Source ESS.

An unexpected constraint of our work at FRM II was caused by technical problems at the neutron guides NL5 and NL6, which severely limited the number of operational days of MIRA and RESEDA. Further, the relocation of the imaging beamline ANTARES due to the installation of the neutron guides for the fundamental physics beam line PERC precluded its use altogether. Here we thank the imaging group at PSI for providing beam time at the ICON beam line at SINQ.

We would finally like to thank all funding agencies, namely DFG, BMBF, and the European Union under NMI3 for their continued generous financial support. As a highlight and a result of the highly successful series of experimental studies of topological spin textures at our institute, we are now even able to conduct a research program on topological spin solitons for information technology in the framework of an Advanced Grant of the European Research Council.

Last but not least, we congratulate Dr. Christoph Hugenschmidt for completing his habilitation in the field of positron physics and the large number of research students for completing their bachelor, master, diploma and doctoral thesis. It is with great pleasure and a good deal of pride that we thank all members of our institute for their enthusiastic efforts in teaching and research. Without their outstanding commitment it would not have been possible to advance the large number of highly ambitious projects. The unique combination of hard work and ‘intense’ social events (mostly initiated by our young scientists) have been essential in creating an excellent atmosphere for everybody.

Garching, February 2013

Peter Böni

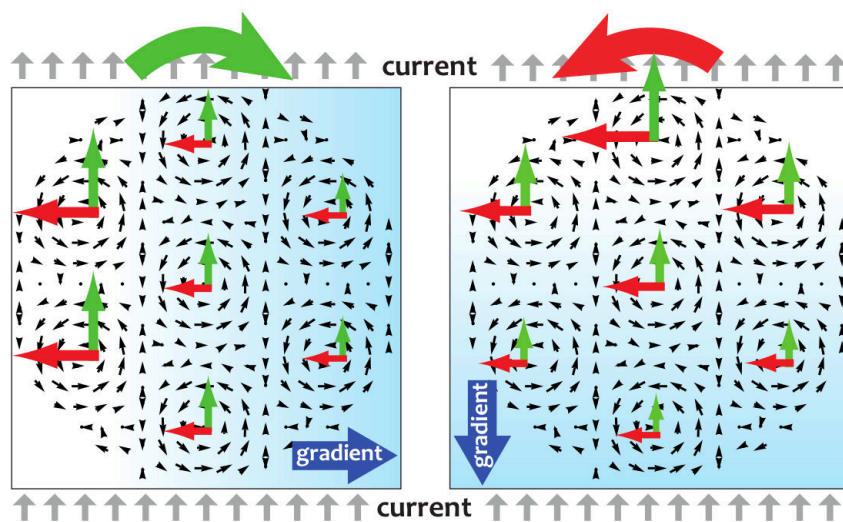
Christian Pfleiderer

Klaus Schreckenbach



# Chapter 1

# Magnetism and Superconductivity



**Skyrmion Lattice**  
(by Achim Rosch, see page 5)



# Rotating Skyrmion Lattices by Spin Torques & Field or Temperature Gradients

Karin Everschor<sup>1,2</sup>, Markus Garst<sup>1</sup>, Benedikt Binz<sup>1</sup>, Florian Jonietz<sup>2</sup>,  
Sebastian Mühlbauer<sup>3</sup>, Christian Pfleiderer<sup>2</sup>, Achim Rosch<sup>1</sup>

<sup>1</sup>Institut für Theoretische Physik, Universität zu Köln, D-50937 Köln, Germany.

<sup>2</sup>Physik-Department E21, Technische Universität München, D-85748 Garching, Germany.

<sup>3</sup>Forschungsneutronenquelle Heinz Maier-Leibnitz (FRM II), Technische Universität München, D-85748 Garching, Germany.

Chiral magnets like MnSi form lattices of skyrmions, i.e. magnetic whirls, which react sensitively to small electric currents  $j$  above a critical current density  $j_c$ . The interplay of these currents with tiny gradients of either the magnetic field or the temperature induce a rotation of the magnetic pattern for  $j > j_c$ . Either a rotation by a finite angle of up to  $15^\circ$  or – for larger gradients – a continuous rotation with a finite angular velocity is induced. We use Landau-Lifshitz-Gilbert equations extended by extra damping terms in combination with a phenomenological treatment of pinning forces to develop a theory of the relevant rotational torques [1] by extending the method used by Thiele [2].

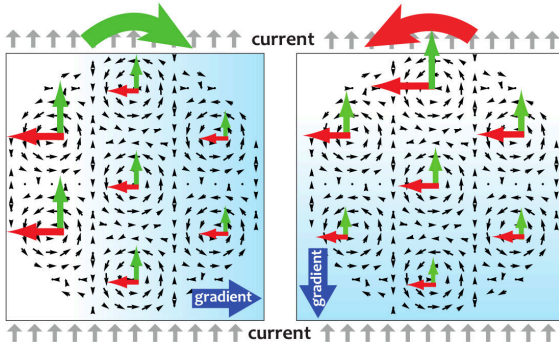


Figure 1: Schematic plot of forces on skyrmion lattice perpendicular and parallel to the current. In the presence of a temperature or field gradient, these forces change smoothly across a domain, thereby inducing rotational torques.

The discovery [3] of the skyrmion lattice in chiral magnets provides new opportunities for investigating the coupling of electric-, thermal- or spin currents to magnetic textures: (i) the coupling by Berry phases to the quantized winding number provides a universal mechanism to create efficiently Magnus forces, (ii) the skyrmion lattice can be manipulated by extremely small forces induced by ultralow currents [4, 5], (iii) the small currents imply that also new types of experiments are possible.

Studying the rotational dynamics of skyrmion domains allows to learn in more detail which forces affect the dynamics of the magnetic texture. The basic idea underlying the theoretical analysis for the rotational motion is sketched in Fig. 1. In the presence of an electric current first, dissipative forces try to drag the skyrmion lattice parallel to the (spin-) current. Second, the interplay of dissipationless spin-currents circulating around each skyrmion and the spin-currents induced by the electric current lead to a Magnus force oriented perpendicular to the current for a static skyrmion lattice (for the realistic case of moving skyrmions the situation is more complicated). In the presence of any gradient across the system (e.g. a temperature or field gradient), indicated by the color gradient, these forces vary in strength across a skyrmion domain and lead to rotational torques. Whether the torque arises from the Magnus forces or the dissipative forces depends, however, on the relative orientation of current and gradient and also on the direction in which the skyrmion lattice drifts.

So far only temperature gradients parallel to the current have been studied experimentally [4]. The observed behaviour for the rotation angle, Fig. 2a), can be modeled within our theory when assuming a weak temperature dependence of Gilbert damping (green curve in Fig. 2b)). In our theory we expect a jump of the rotation angle at  $j_c$ , depending on the domain size. This appears to be consistent with the observed steep increase of the rotation angle at  $j_c$ , when taking into account that the experimental results are subject to a distribution of domain sizes. Furthermore we predict that for even larger currents a continuous rotation will occur. The measured distribution of rotation angles shown in Fig. 2 extends up to the maximally possible value of  $15^\circ$  for static domains, suggesting that continuously rotating domains are either already present in the system or may be reached by using slightly larger currents or temperature gradients.

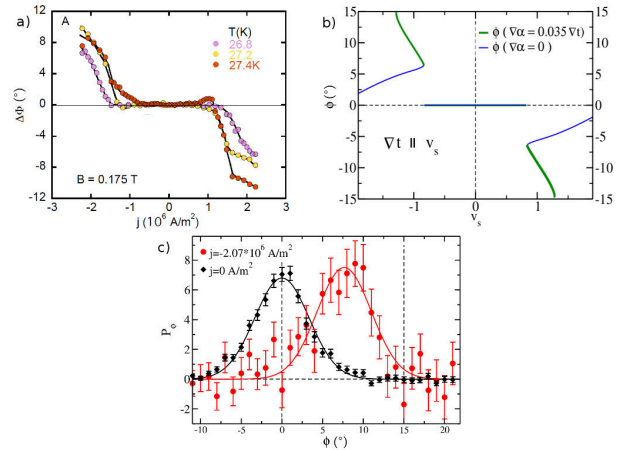


Figure 2: a) Average rotation angle  $\Delta\phi$  of skyrmion lattice in MnSi measured by neutron scattering [4]. b) Rotation angle  $\phi$  as function of effective spin velocity  $v_s$ . As in experiment the temperature gradient  $\nabla t$  grows with the square of the applied current. Assumption for thin blue curve: damping constants are independent of  $t$ . For thick green curve we assumed a weak temperature dependence of the Gilbert damping constant  $\alpha$  to reflect the experimental observation. c) Angular distribution  $P_\phi$  of the intensity for currents of strength  $j = 0$  and  $j \approx -2.07 \cdot 10^6 \text{ A/m}^2$ .

We acknowledge discussions with M. Halder, M. Mochizuki, and T. Nattermann and financial support of the DFG through SFB 608, TRR80, and FOR960, as well as the European Research Council through ERC-AdG (Grant No. 291079). K.E. thanks the Deutsche Telekom Stiftung and the Bonn Cologne Graduate School.

## References

- [1] K. Everschor et al., Phys. Rev. B **86**, 054432 (2012).
- [2] A. A. Thiele Phys. Rev. Lett. **30**, 230 (1973).
- [3] S. Mühlbauer et al., Science **323**, 915 (2009).
- [4] F. Jonietz et al., Science **330**, 1648 (2010).
- [5] T. Schulz et al., Nat. Phys. **8**, 301 (2012).

# Fluctuation-Induced First-Order Phase Transition in DM-Helimagnets

Marc Janoschek<sup>1, 2, 3</sup>, Markus Garst<sup>4</sup>, Andreas Bauer<sup>1</sup>, Pascal Krautscheid<sup>4</sup>,  
Robert Georgii<sup>1, 5</sup>, Peter Böni<sup>1</sup>, Christian Pfleiderer<sup>1</sup>

<sup>1</sup>Physik-Department E21, Technische Universität München, D-85748 Garching, Germany.

<sup>2</sup>Department of Physics, University of California, San Diego, La Jolla, CA 92093-0354, USA

<sup>3</sup>Los Alamos National Laboratory, Los Alamos, New Mexico 87545, USA

<sup>4</sup>Institute for Theoretical Physics, Universität zu Köln, D-50937 Köln, Germany

<sup>5</sup>Forschungsneutronenquelle Heinz Maier-Leibnitz (FRM II), Technische Universität München, D-85748 Garching, Germany.

In 1972 Nobel prize laureate P. W. Anderson argued that “more is different”; complex systems often possess qualities going beyond the properties of their well-understood constituents and emerge due to collective interactions [1]. Particularly fascinating are continuous transitions of such complex systems representing a smooth macroscopic change of state (e.g from nonmagnetic to magnetic). At the transition collective fluctuations extend over macroscopic length scales resulting in spectacular cooperative phenomena like critical opalescence. Here, it has long been noticed theoretically that an excess of such fluctuations changes the character of these transitions profoundly driving them discontinuous, i.e., first-order. Notably, such fluctuation-induced first-order transitions are of interest for a wide range of topics like liquid crystals, superconductors, cold atom systems or even phase transitions in the early universe (see references in Ref. [2]). Experimentally, however, few such systems have been identified because the relevant fluctuations are hard to resolve.

Using neutron scattering we directly probe the magnetic fluctuations of the prototypical cubic helimagnet MnSi, and demonstrate that cubic helimagnets stabilized by the Dzyaloshinskii-Moriya (DM) interaction represent a new model system for fluctuation-induced first-order transitions [2]. This, for the first time, paves the way for more detailed experimental investigations of this relevant class of phase transitions. We observe the emergence of abundant fluctuations on the surface of a sphere in the vicinity of the paramagnetic-helimagnetic transition. Our high-resolution measurements quantitatively agree with a theory by Brazovskii according to which the strong interactions between the fluctuations that abound on the sphere drive the transition first-order [3]. The nature of the helimagnetic transition in MnSi at  $T_c = 29$  K has been elusive previous to our study because on the one hand extensive magnetic fluctuations typical for a continuous phase transition are observed, but on the other hand specific-heat measurements show the hallmark of a first-order transition: the release of latent heat. An additional broad feature that is observed in the specific heat at  $T^* = T_c + 1$  K led several groups to propose the presence of an intermediate phase enclosed between  $T_c$  and  $T^*$  with a complex form of magnetic order (see references in Ref. [2]), however, without attempting a quantitative comparison to the data. Neutron scattering directly couples to the magnetic fluctuations and measures their inverse correlation length  $\kappa = 2\pi/\xi$ , allowing us to solve the conundrum of the helimagnetic transition in MnSi. Notably, we have for the first time mapped the fluctuations near  $T_c$  in three dimensions and were able to show that they emerge not at a single point in momentum space as for a ferromagnet but rather on the surface of a sphere with a radius  $Q = 2\pi/\lambda$  (center inset of Fig. 1) resulting in a large phase space for fluctuations. The interaction of fluctuations with such a lar-

ge phase space suppresses the correlation length  $\xi = 2\pi/\kappa$  resulting in a peculiar temperature dependence of  $\kappa$  (see Fig. 1) that is quantitatively described by our theory based on previous work by Brazovskii [3]. Furthermore, it inhibits the condensation of long-range order giving rise to a unique fluctuation-disordered regime for  $T_c < T < T^*$  until it realizes a first-order transition at  $T_c$ . Finally, as shown in the full article [2] the Brazovskii theory also accounts for the feature at  $T^*$  as observed in the specific heat and the magnetic susceptibility that is induced by interacting helimagnetic fluctuations.

In conclusion, this work solves the riddle about the nature of the paramagnetic-helimagnetic phase transition in cubic B20 helimagnets, where notably Brazovskii fluctuations may be important for the stabilization of topological magnetic textures that offer promising routes towards multiferroic [4] or spintronic applications [5].

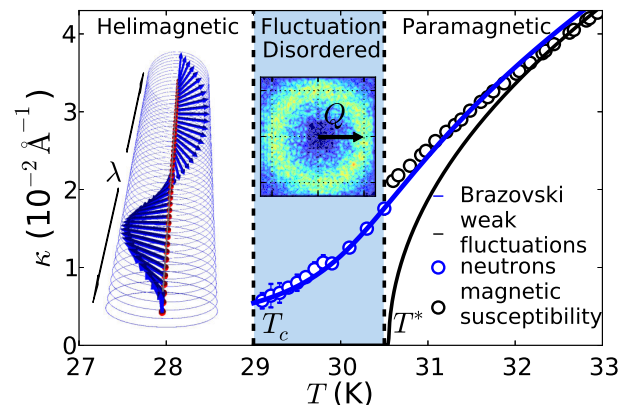


Figure 1: Brazovskii-type phase transition between the paramagnetic and helimagnetic phase of MnSi. Below  $T_c = 29$  K, MnSi forms a magnetic helix with a period  $\lambda$  as shown in the left inset. Above  $T_c$  MnSi is paramagnetic and shows magnetic fluctuations as expected for a second-order phase transition. However, below  $T^*$ , the fluctuations form on a sphere in momentum space with a radius  $Q = 2\pi/\lambda$  prototypical for a Brazovskii transition (center inset shows a cut through the sphere). For a second-order phase transition with weak fluctuations the inverse correlation length  $\kappa$  should go to zero at  $T^*$  (black curve). However, the strong and abundant fluctuations on the sphere lead to a fluctuation-disordered regime (blue shaded region) and renormalize the observed  $\kappa$  (circles) near the phase transition, leading to a fluctuation-induced first-order transition (see text). The blue line is a fit to the Brazovskii theory.

## References

- [1] P. W. Anderson, *Science* **177** 393-396 (1972).
- [2] M. Janoschek *et al.*, arXiv:1205.4780 (2012).
- [3] S. A. Brazovskii, *Sov. Phys. JETP* **41**, 85 (1975).
- [4] S. Seki *et al.*, *Science* **336**, 198 (2012).
- [5] T. Schulz *et al.*, *Science* **2231** (2012).

# Magnetic Phase Diagram of MnSi Inferred from Magnetization and ac Susceptibility

Andreas Bauer<sup>1</sup>, Christian Pfleiderer<sup>1</sup>

<sup>1</sup> Physik-Department E21, Technische Universität München, D-85748 Garching, Germany.

We report simultaneous measurements of the magnetization and the ac susceptibility across the magnetic phase diagram of single-crystal MnSi.[1] In our study we explore the importance of the excitation frequency, excitation amplitude, sample shape, and crystallographic orientation, see Fig. 1 and Fig. 2.

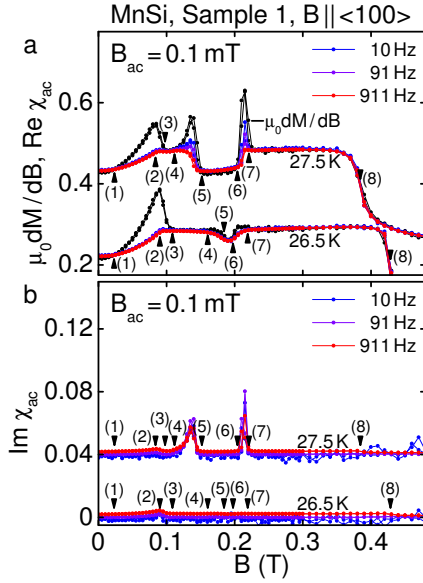


Figure 1: AC susceptibility of MnSi for different excitation frequencies as a function of field along the  $\langle 110 \rangle$  axis.  $\mu_0 dM/dB$  represents the susceptibility calculated from the dc magnetization. (a) Real Part. (b) Imaginary Part.

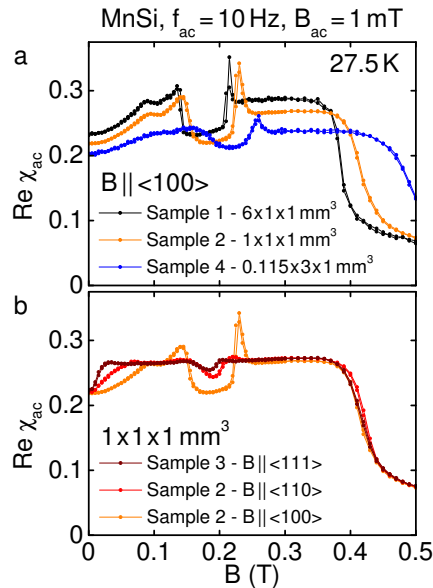


Figure 2: AC susceptibility of MnSi as a function of applied field. (a) For field along  $\langle 110 \rangle$  and different sample geometries and hence demagnetization factors. (b) For field along the major crystallographic directions while keeping demagnetization unchanged.

The susceptibility,  $\mu_0 dM/dB$ , calculated from the magnetization, is dominated by pronounced maxima at the transition from the helical to the conical and the conical to the skyrmion lattice phase. The maxima in  $\mu_0 dM/dB$  are not tracked by the ac susceptibility, which in addition varies sensitively with the excitation amplitude and frequency at the transition from the conical to the skyrmion lattice phase. The same differences between  $\mu_0 dM/dB$  and the ac susceptibility exist for  $\text{Mn}_{1-x}\text{Fe}_x\text{Si}$  ( $x = 0.04$ ) and  $\text{Fe}_{1-x}\text{Co}_x\text{Si}$  ( $x = 0.20$ ).

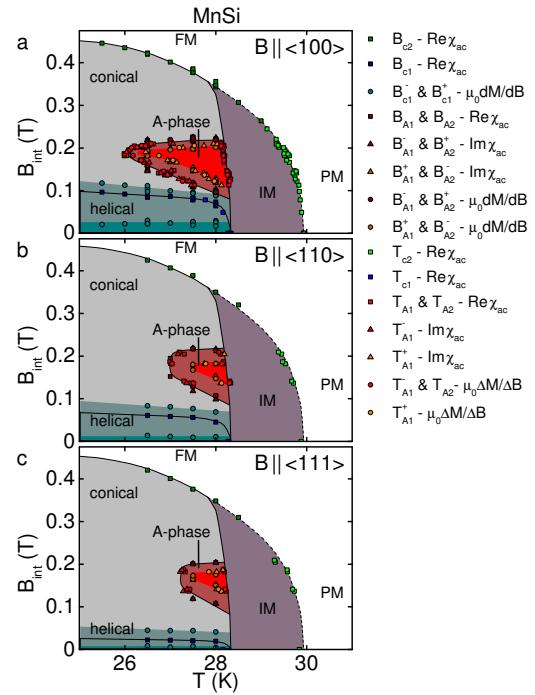


Figure 3: Magnetic phase diagram of MnSi for all major crystallographic directions.

Taken together, as shown in Fig. 3 our study establishes consistently for all major crystallographic directions the existence of a single pocket of the skyrmion lattice phase in MnSi, suggestive of a universal characteristic of all B20 transition metal compounds with helimagnetic order. These results strongly question a recent study[2] on FeGe where a complex phase diagram showing multiple phase pockets and meso-phases was inferred from measurements of the ac susceptibility at a single excitation frequency on an irregular shaped sample.

## References

- [1] A. Bauer and C. Pfleiderer, Phys. Rev. B **85**, 214418 (2012).
- [2] H. Wilhelm, M. Baenitz, M. Schmidt, U. K. Rößler, A. A. Leonov, and A. N. Bogdanov, Phys. Rev. Lett. **107**, 127203 (2011).

# Observation of Coherent Helimagnons and Gilbert Damping in an Itinerant Magnet

Jake Koralek<sup>1</sup>, Dennis Meier<sup>2</sup>, James Hinton<sup>1, 2</sup>, Andreas Bauer<sup>3</sup>, Sid Parameswaran<sup>2</sup>, Ashvin Vishwanath<sup>1, 2</sup>, Ramamoorthy Ramesh<sup>1, 2</sup>, Bob Schoenlein<sup>1</sup>, Christian Pfleiderer<sup>3</sup>, Joe Orenstein<sup>1, 2</sup>

<sup>1</sup> Materials Science Division, Lawrence Berkeley National Laboratory, Berkeley, California 94720, USA

<sup>2</sup> Department of Physics, University of California, Berkeley, California 94720, USA

<sup>3</sup> Physik-Department E21, Technische Universität München, D-85748 Garching, Germany.

We study the magnetic excitations of itinerant helimagnets by applying time-resolved optical spectroscopy to  $\text{Fe}_{0.8}\text{Co}_{0.2}\text{Si}$ . [1] Optically excited oscillations of the magnetization in the helical state are found to disperse to lower frequency as the applied magnetic field is increased; the fingerprint of collective modes unique to helimagnets, known as helimagnons. The use of time-resolved pump-probe spectroscopy allows us to address the fundamental magnetic relaxation processes by directly measuring the Gilbert damping, revealing the versatility of spin dynamics in chiral magnets.

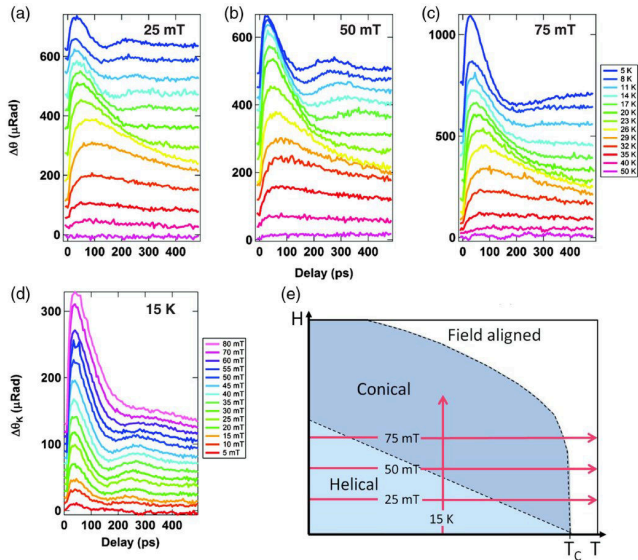


Figure 1: (a)-(c) Time dependence of the pump-induced change in Kerr rotation,  $\Delta\Theta_K$ , as a function of temperature for several applied magnetic fields. (d)  $\Delta\Theta_K$  as a function of magnetic field at  $T = 15$  K. Curves are offset for clarity. (e) Schematic magnetic phase diagram.

Fig. 1 shows typical data of the pump-induced change in Kerr rotation,  $\Delta\Theta_K$ , as a function of temperature and applied magnetic fields. Here, the oscillating part of the signal stems from helimagnon excitations and may be fitted by a decaying sinusoidal function  $\Delta\Theta_K = e^{-t/\tau_K} [A + B \sin(\omega t)]$  with a time dependent frequency  $\omega(t) = 2\pi f_0 [1 + D e^{-t/\tau_K}]$ , see Fig. 2(a).

Within a simple model one expects for the field dependence of the  $q = 0$  helimagnon frequency  $f_0 = g\mu_B H_c \left(1 - \frac{1}{2} \left(\frac{H}{H_c}\right)^2\right)^{1/2}$ . A corresponding fit is depicted as solid line in Fig. 2(c) in good agreement with the measured data and corroborating our helimagnon interpretation of the observed oscillation. Finally, from the relation  $\alpha = (2\pi f_0 \tau_K)^{-1}$  we directly obtain a Gilbert damping parameter  $\alpha = 0.4 \pm 0.1$ .

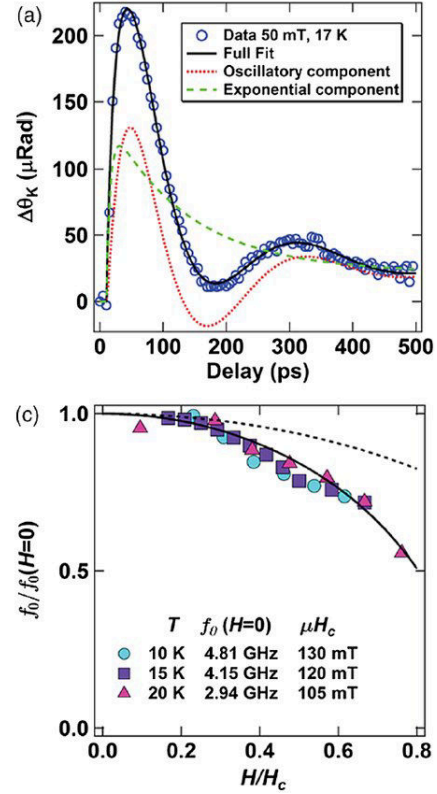


Figure 2: (a) Exemplary  $\Delta\Theta_K$  oscillation data (blue circles) and fit (solid black line) using the model described in the text. The fit is decomposed into an exponential term (dashed green line) and an oscillatory term (dotted red line). (c) Magnetization oscillation frequency as a function of field.

In summary, this work demonstrates ultrafast coherent optical excitation of spin waves in an itinerant DM-driven spin system and reveals the underlying spin dynamics. We identify these excitations as helimagnons through their anomalous field dependence and explain our observations with a comprehensive model. Our experiments directly yield the intrinsic Gilbert damping parameter, revealing a striking difference in spin relaxation phenomena between itinerant and localized helimagnets. The results elucidate the dynamics of collective modes common to the actively studied B20 transition metal compounds that codetermine their performance in potential spin based applications.

## References

- [1] J. D. Koralek, D. Meier, J. P. Hinton, A. Bauer, S. A. Parameswaran, A. Vishwanath, R. Ramesh, R. W. Schoenlein, C. Pfleiderer, and J. Orenstein, Phys. Rev. Lett. **109**, 247204 (2012).

# First Order Metamagnetic Transition in $\text{Ho}_2\text{Ti}_2\text{O}_7$ Observed by Vibrating Coil Magnetometry at Milli-Kelvin Temperatures

C. Krey<sup>1</sup>, S. Legl<sup>1</sup>, S.R. Dunsiger<sup>1</sup>, M. Meven<sup>2</sup>, J. S. Gardner<sup>3</sup>, J. M. Roper<sup>4</sup>,  
C. Pfleiderer<sup>1</sup>

<sup>1</sup>Physik-Department E21, Technische Universität München, D-85748 Garching, Germany.

<sup>2</sup>Forschungszentrum Neutronenquelle Heinz Maier-Leibnitz (FRM II), Technische Universität München, D-85748 Garching, Germany.

<sup>3</sup>Department of Physics, Indiana University, Bloomington, Indiana 47408, USA

<sup>4</sup>Los Alamos National Laboratory, Los Alamos, New Mexico 87545, USA

Metamagnetic transitions (MMT) in spin ice systems  $\text{Dy}_2\text{Ti}_2\text{O}_7$  and  $\text{Ho}_2\text{Ti}_2\text{O}_7$  has been argued to reflect directly the nature of the spin excitations from the zero-field spin state [1]. In these isostructural compounds the magnetic ions reside on the vertices of a network of corner sharing tetrahedra within a pyrochlore lattice. The presence of local  $\langle 111 \rangle$  crystalline anisotropy and effective ferromagnetic interactions constrain two spins to point outward and two spins towards the centre of each tetrahedron. In  $\text{Dy}_2\text{Ti}_2\text{O}_7$  the field induced MMT is associated with an ice-rule breaking spin flip to the three-in-one-out (one-in-three-out) state [2]. Recent theoretical work suggests that the spin flips may be viewed as emergent magnetic monopoles [1].  $\text{Ho}_2\text{Ti}_2\text{O}_7$  is a second candidate within this framework. However, the experimental situation is much less clear. In general, the magnetic phase diagram of Ho-based compounds may have strong effects below 0.5 K due to hyperfine interactions.

We report vibrating coil magnetometry (VCM) of the spin ice system  $\text{Ho}_2\text{Ti}_2\text{O}_7$  down to  $\sim 0.04$  K for magnetic fields up to 5 T applied parallel to the  $[111]$  axis [3]. The VCM, developed at TUM, operates in a dilution refrigerator at 41 Hz [4]. The  $\text{Ho}_2\text{Ti}_2\text{O}_7$  single crystal studied was grown by optical float zoning at LANL. The disc-shaped single crystal was approximately described as an ellipsoid with a demagnetization factor of  $N = 0.75$ .

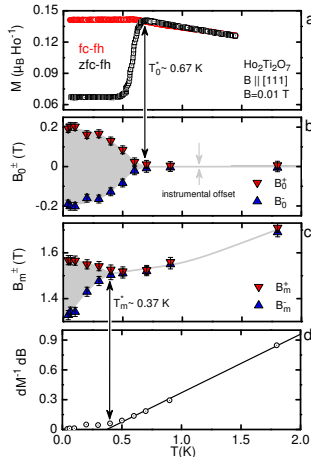


Figure 1: Magnetization showing (a) spin freezing in a applied field of 0.01 T, (b) zero field hysteresis, (c) coercive field at the MMT and (d) peak value of  $dM/dB$  when approaching the MMT.

History-dependent behavior emerges below  $T_0^* \sim 0.6$  K for  $B = 0.01$  T along  $[111]$  in  $\text{Ho}_2\text{Ti}_2\text{O}_7$ . The zero-field cooled (zfc/fh) and field cooled (fc/fh) data begin to show pronounced differences, shown in Figure 1(a). With decreasing temperature the low-field magnetization increases gradually, characteristic of a paramagnetic state. The history dependence shares many features of magnetic blocking. In large magnetic fields we observe a magnetization plateau

followed by a hysteretic MMT (Figure 2(a)). The history dependence below  $T_0^*$  is connected with strong hysteresis with respect to  $B = 0$  (Figure 2(b) to (e)), followed by a metamagnetic increase at a field  $B_m^\pm \sim 1.5$  T, which becomes distinctly hysteretic at low temperatures. Hysteresis exists with respect to both  $B = 0$  and  $B_m = 1.5$  T for 0.1 K (Figure 1(b),(c)).

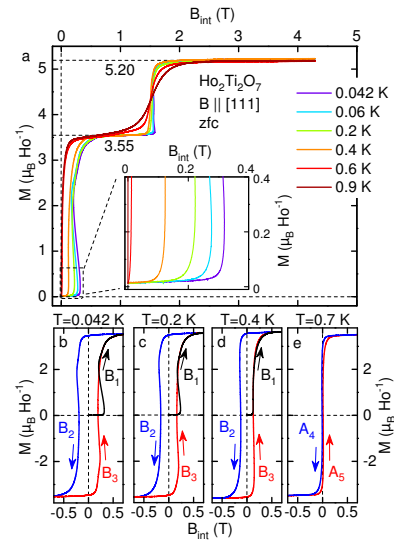


Figure 2: Magnetization as a function of internal magnetic fields. For  $T < T_0^*$  the initial change of the magnetization is zero and followed by a very pronounced increase with increasing field. (a) Magnetic field dependence and (b) - (e) magnetization in field cycles.

In order to track the width of the hysteresis loop we define coercive fields  $B_0^-$ ,  $B_0^+$  and  $B_m^-$ ,  $B_m^+$ . Shown in Figure 1(b) are the coercive fields  $B_0^-$ ,  $B_0^+$ , which increase strongly below  $T_0^*$  with decreasing temperature. In contrast, the hysteretic behaviour at high fields appears at  $T_m^* = 0.37$  K, well below  $T_0^*$  (Figure 1(c)). The temperature dependence of the coercive fields as well as  $dM/dB$  (Figure 1(c), (d)) identify the metamagnetic transition as a line of first order transitions terminating in a critical endpoint at  $T_m^* \simeq 0.37$  K,  $B_m \simeq 1.5$  T.

The MMT in  $\text{Ho}_2\text{Ti}_2\text{O}_7$  is strongly reminiscent of that observed in  $\text{Dy}_2\text{Ti}_2\text{O}_7$ , establishing the field induced liquid-gas like transition as a more pervasive phenomenon within spin ice systems. Remarkably, the phase boundaries appear to be independent of the strength of the hyperfine interactions, which are much stronger in  $\text{Ho}_2\text{Ti}_2\text{O}_7$ . However, given the importance of dipolar interactions as an essential prerequisite for a description of monopole excitations, it seems clear that further Ising like compounds *not* based on Ho or Dy must be investigated.

## References

- [1] C. Castellano *et al.*, Nature **451**, 42 (2008).
- [2] T. Sakakibara *et al.*, Phys. Rev. Lett. **90**, 207205 (2003).
- [3] C. Krey *et al.*, Phys. Rev. Lett. **108**, 257204 (2012).
- [4] S. Legl *et al.*, Rev. Sci. Instr. **81**, 043911 (2010).

# Vibrating-Coil Magnetometry of the Spin Liquid Properties of $Tb_2Ti_2O_7$

S. Legl<sup>1</sup>, C. Krey<sup>1</sup>, S.R. Dunsiger<sup>1</sup>, H.A. Dabkowska<sup>2</sup>, J.A. Rodriguez<sup>3,4</sup>, G.M. Luke<sup>3</sup>, C. Pfleiderer<sup>1</sup>

<sup>1</sup>Physik-Department E21, Technische Universität München, D-85748 Garching, Germany.

<sup>2</sup>Brockhouse Institute for Materials Research, McMaster University, Hamilton, Ontario L8S 4M1, Canada

<sup>3</sup>Department of Physics and Astronomy, McMaster University, Hamilton, Ontario L8S 4M1, Canada

<sup>4</sup>Laboratory for Muon Spin Spectroscopy, Paul Scherrer Institut, 5232 Villigen, Switzerland

Magnetic pyrochlore oxides,  $A_2B_2O_7$ , can be ideal examples of geometric frustration. In the pyrochlores  $Ho_2Ti_2O_7$  and  $Dy_2Ti_2O_7$  a strong easy-axis (Ising)-anisotropy along the local  $[111]$  axis on the rare earth site within the unit cell, together with net ferromagnetic interactions, are the most important preconditions for the emergence of spin ice behavior, which has been modelled theoretically with enormous success. An unresolved question concerns the consequences of reducing the strength of the local Ising anisotropy. An exciting theory [1] postulates a “quantum spin ice (QSI)” scenario, when quantum fluctuations renormalize the interactions. Striking magnetization plateaux are predicted, like those observed in  $Ho_2Ti_2O_7$  and  $Dy_2Ti_2O_7$ , for a magnetic field strictly along a global  $[111]$  axis [2].  $Tb_2Ti_2O_7$  is an ideal model system of such a scenario. At high temperatures  $Tb_2Ti_2O_7$  exhibits a Curie-Weiss susceptibility with a large effective moment  $\mu_{\text{eff}} = 9.6\mu_B Tb^{-1}$  and a negative Curie-Weiss temperature  $\Theta_{\text{CW}}$  characteristic of antiferromagnetic interactions. However,  $\mu\text{SR}$ , ac susceptibility, and Neutron Spin Echo (NSE) established strong spin dynamics down to 20 mK without long-range magnetic order, known as cooperative paramagnetism. The origin of the reported coexisting magnetic glassiness remains unclear and may be either intrinsic or due to defects. Taken together, the nature of the spin liquid state in  $Tb_2Ti_2O_7$  and the proposal of QSI are hence unresolved.

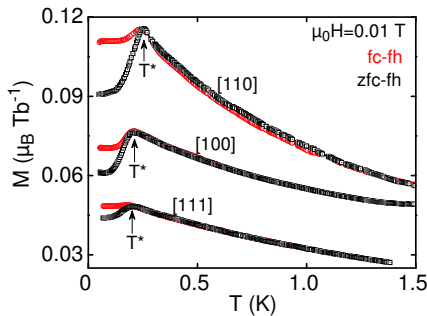


Figure 1: Temperature dependence of the magnetization of  $Tb_2Ti_2O_7$  in an applied magnetic field of 10 mT. Below  $T^* \sim 200$  mK a distinct difference between data recorded under zero-field cooling (zfc) and field-cooling (fc) emerges. Curves are shifted for clarity.

We address this by measuring the magnetization of a  $Tb_2Ti_2O_7$  single-crystal at TUM using a bespoke vibrating-coil magnetometer (VCM) for temperatures down to  $\sim 0.04$  K and magnetic fields up to 5 T [3, 4]. The  $Tb_2Ti_2O_7$  single crystal was grown at McMaster University by optical float-zoning. The single-crystalline disc used was oriented such that the face was perpendicular to  $[111]$  within  $\sim 1^\circ$ . The sample was approximated as an ellipsoid with a demagnetising factor  $N = 0.34$ . We observe magnetic history dependence below  $T^* \sim 0.2$  K reminiscent of the classical spin ice systems  $Ho_2Ti_2O_7$  and  $Dy_2Ti_2O_7$ . Figure 1 illustrates the temperature dependence of the magnetization in an applied field of 10 mT, where data for  $[100]$  and  $[110]$  have

been shifted by  $0.03\mu_B Tb^{-1}$  and  $0.06\mu_B Tb^{-1}$ , respectively for clarity. With decreasing temperature the magnetization increases with a positive curvature consistent with the paramagnetic properties at high temperatures. In all field directions, the curves display a cusp in the zfc-fh and fc-fh data. The shape of the cusp, the absolute difference of zfc-fh and fc-fh data and the qualitative temperature dependence of the data provide strong evidence of the emergence of intrinsic magnetic glassiness below  $T^*$  which is essentially isotropic. The glassiness also suggests that the spin freezing is not specific to classical spin ice.

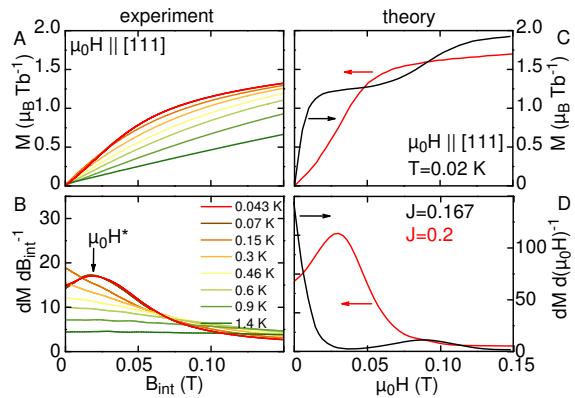


Figure 2: Experimental and theoretical low-field magnetization of  $Tb_2Ti_2O_7$  for the  $[111]$  axis. (A) Magnetic field dependence of the magnetization of  $Tb_2Ti_2O_7$  in small fields at various temperatures. (B) Numerical derivative of the data shown in panel (A). (C) Theoretically predicted magnetization for a QSI in  $Tb_2Ti_2O_7$  as reported in Ref. [1]. (D) Derivative of the theoretical data shown in panel (C).

It is important to note that this plot does not display a point of inflection of  $M(B)$ . Instead,  $dM/dB$  has a broad maximum only. Data for  $[110]$  and  $[100]$  (not shown) are similar to the  $[111]$  axis. For comparison we reproduce in Figure 2(C) and (D) theoretical calculations of the magnetization and their first derivatives at 20 mK for two different  $J$ ,  $J = 0.167$  (“quantum spin ice”(QSI)) and  $J = 0.2$  (“all-in/ all-out”(AIAO)) [1]. The difference between the QSI and AIAO concerns the marked change in the slope of  $dM/dB$  at low field ( $< 0.05$  T) from negative to positive for QSI and AIAO structures, respectively. Taken together we find no evidence of the magnetization plateaux in  $Tb_2Ti_2O_7$  expected of QSI and fluctuation-induced ferromagnetic interactions. Instead, our data are in semi-quantitative agreement with the theoretical predictions of AIAO-antiferromagnetism, suggesting that the spin liquid state in  $Tb_2Ti_2O_7$  may be viewed as an incipient AIAO antiferromagnet.

## References

- [1] H.R. Molavian and M.J.P. Gingras, *Journal of Physics: Condensed Matter* **21**, 172201 (2009).
- [2] C. Krey *et al.*, *Phys. Rev. Lett.* **108**, 257204 (2012).
- [3] S. Legl *et al.*, *Phys. Rev. Lett.* **109**, 047201 (2012).
- [4] S. Legl *et al.*, *Rev. Sci. Instr.* **81**, 043911 (2010).

## Emergent Electrodynamics of Skyrmions in a Chiral Magnet

Tomek Schulz<sup>1</sup>, Robert Ritz<sup>1</sup>, Andreas Bauer<sup>1</sup>, Marco Halder<sup>1</sup>, Michael Wagner<sup>1</sup>,  
Christian Franz<sup>1</sup>, Christian Pfleiderer<sup>1</sup>, Karin Everschor<sup>2</sup>, Markus Garst<sup>2</sup>, Achim Rosch<sup>2</sup>

<sup>1</sup>Physik-Department E21, Technische Universität München, D-85748 Garching, Germany.

<sup>2</sup>Institut für theoretische Physik, Universität zu Köln, D-50937 Köln, Germany.

When an electron moves in a smoothly varying non-collinear magnetic structure, its spin orientation adapts constantly, thereby inducing forces that act both on the magnetic structure and on the electron. These forces may be described by electric and magnetic fields of an emergent electrodynamics [1–4]. The topologically quantized winding number of so-called skyrmions, a type of magnetic whirl discovered recently in chiral magnets [5–7], has been predicted to induce exactly one quantum of emergent magnetic flux per skyrmion. A moving skyrmion is therefore expected to induce an emergent electric field following Faraday's law of induction, which inherits this topological quantization [8].

Through measuring the temperature dependence of the Hall resistivity,  $\rho_{xy}(T)$ , in the skyrmion lattice phase of MnSi under a large applied d.c. electric current, we can show that the topological Hall effect contribution, signature of the skyrmion lattice, is suppressed through an emergent electric field  $E^e$  that builds up in the opposite direction of the Hall voltage (fig. 1).

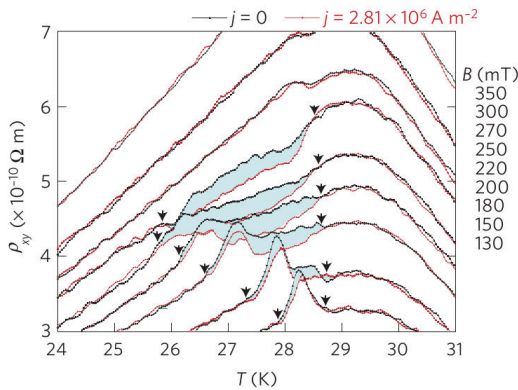


Figure 1: Temperature dependence of the Hall resistivity,  $\rho_{xy}$ , in the skyrmion lattice phase of MnSi under a large applied d.c. electric current. To study the effect of the applied d.c. current it is superimposed on a small a.c. excitation which allows detection of the signal. Shown is the Hall resistivity for various magnetic fields. Under an applied d.c. current of  $2.81 \times 10^6 \text{ A m}^{-2}$  the Hall signal is suppressed in the entire skyrmion phase (green shading).

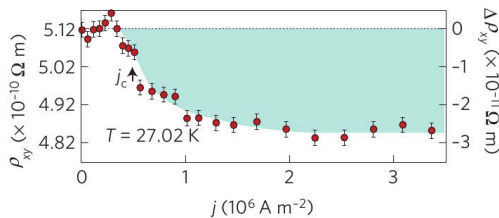


Figure 2: Typical variation of the Hall resistivity,  $\rho_{xy}$ , of MnSi as a function of applied d.c. current at  $B = 250 \text{ mT}$  and for  $T = 27.02 \text{ K}$ . For temperatures in the skyrmion lattice phase, like shown here, the signal is suppressed above an ultralow current density,  $j_c$ , and converges towards a constant value for large currents. Absolute data values are given on the left-hand side and the relative change with respect to  $j = 0$  is given on the right-hand side.

At a certain threshold  $j_c$  of the applied d.c. current, the skyrmion lattice depins and begins to drift. In agreement with previous SANS experiments [9] we find an exceptionally low  $j_c \approx 10^6 \text{ A m}^{-2}$  that is five orders of magnitude smaller than observed in conventional systems (fig. 2). From the observed changes in the Hall resistivity  $\rho_{xy}$  we are able to directly calculate the emerging electric field  $E^e$  and the drift velocity  $v_{d||}$ , and hence track the motion of the drifting skyrmion lattice (fig. 3). Thereby, our measurements establish quantitatively the predicted emergent electrodynamics [10].

In summary, we are able to directly observe the emergent electric field of skyrmions and measure their depinning transition and subsequent motion quantitatively. This offers fundamental insights into the connection between the emergent and real electrodynamics of skyrmions in chiral magnets. Furthermore, this opens the possibility to address fundamental questions of the coupling of magnetism, electric currents and defects, respectively. The control and detection of the motion of magnetic whirls (skyrmions) by the interplay of emergent and real electrodynamics therefore promises to become an important route towards spintronic applications.

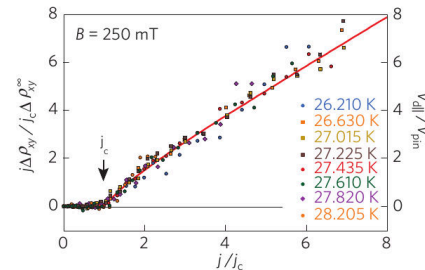


Figure 3: Scaling plot of the transverse electric field,  $\Delta E_{\perp} = -j\rho_{xy}$ , in units of  $j_c\rho_{xy}^{\infty}$ , induced by the moving skyrmion lattice. As  $E_{\perp}$  is proportional to the emergent field  $E^e$ , this also constitutes a scaling plot of the emergent electric field  $E^e$  (in units of  $v_{\text{pin}}B^e$ ) or of the drift velocity  $v_{d||}$  in units of the pinning velocity  $v_{\text{pin}}$ .

### References

- [1] G. Volovik, J. Phys. C **20**, L87 (1987).
- [2] S.A. Yang *et al.*, Phys. Rev. Lett. **102**, 067201 (2009).
- [3] P.N. Hai *et al.*, Nature **458**, 489-492 (2009).
- [4] S.E. Barnes *et al.*, Phys. Rev. Lett. **98**, 246601 (2007).
- [5] S. Mühlbauer *et al.*, Science **323**, 915-919 (2009).
- [6] A. Neubauer *et al.*, Phys. Rev. Lett. **102**, 186602 (2009).
- [7] X.Z. Yu *et al.*, Nature **465**, 901-904 (2010).
- [8] J. Zang *et al.*, Phys. Rev. Lett. **107**, 136804 (2011).
- [9] F. Jonietz *et al.*, Science **330**, 1648-1651 (2010).
- [10] T. Schulz *et al.*, Nature Physics **8**, 301-304 (2012).

# Direct Manipulation of the Uncompensated Antiferromagnetic Spins in Exchange Coupled System by GeV Ion Irradiation

Amitesh Paul<sup>1</sup>, Stefan Mattauch<sup>2</sup>, Peter Böni<sup>1</sup>

<sup>1</sup>Physik-Department E21, Technische Universität München, D-85748 Garching, Germany.

<sup>2</sup>Jülich Centre for Neutron Science Forschungszentrum Jülich GmbH, Auenstelle am FRM-II c/o TU München, Lichtenbergstrae 1, D-85747 Garching b. München, Germany

We present here a unique ex situ approach in manipulating the uncompensated spins in antiferromagnetic layers of ferro-/antiferromagnetic (CoO-Co) exchange coupled systems on a nanometric scale. We use the impact of relativistic heavy ion (GeV) irradiation on such systems. This study demonstrates the possibility of nanoscale tailoring of exchange coupled systems that survive even in the trained state.

It has been shown earlier that local manipulations of magnetization are (a) confined to a few nanometers only (b) without significant modification of the interface structure, and (c) applicable for ex situ changes. [1] Thus irradiation techniques offer means of magnetic-tailoring devices in information technology such as in exchange biased system.

Figure 1 shows the specular reflectivity data (NSF and SF) and the off-specular SF intensities corresponding to two different applied fields ( $H_a$ ) for the  $U \times 10^{13}$  ions irradiated ML. We also plot the spin asymmetry (SA) signals (difference in  $R_{++}$  and  $R_{--}$  divided by the sum of the two) as we compare it with the as-deposited specimen at saturation.

Relative variation of the multilayer Bragg peak intensities is quite evident here. The NSF intensity map shows vertically correlated multilayer interfaces added up in phase and forming the Bragg sheets in reciprocal space at the first Bragg peak position of 15 mrad. A small increase in the SF intensity at  $Q=0.02 \text{ \AA}^{-1}$ , measured during the first field cycle close to the coercive field (as compared to that in saturation), is only due to an increased instability induced in the system as the layers are on the verge of flipping and cannot be attributed to coherent rotation of the layers (a similar behavior is observed during the second field cycle as well). This is further corroborated by an increase in the off-specular SF intensities near the critical edge around the coercive field, a typical signature of random non-collinear arrangement of small scale ( $<1 \text{ nm}$ ) domains just before flipping. [3] Distorted wave Born approximation (DWBA) has been applied in simulating the corresponding SF intensity map.

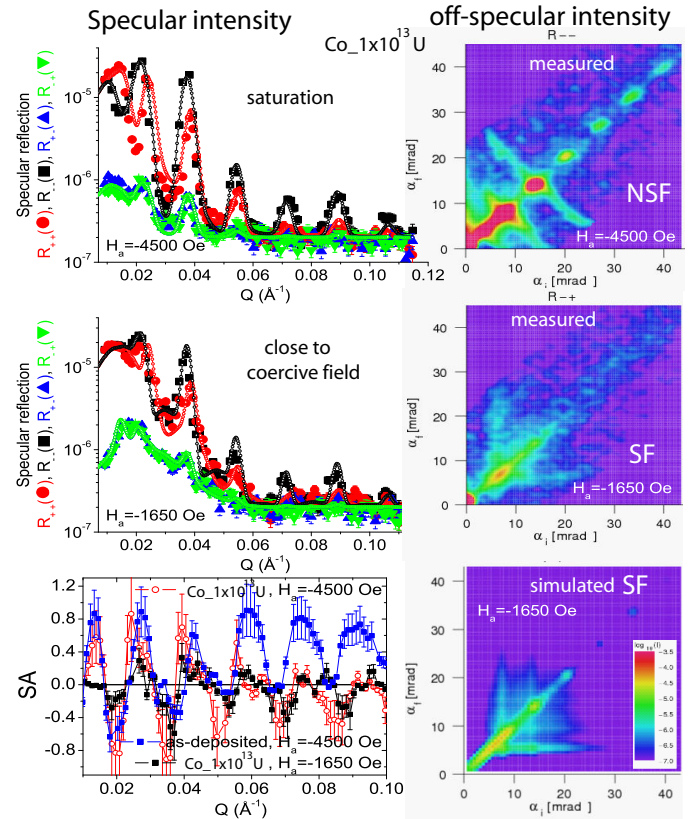


Figure 1: Specular reflectivity patterns (solid symbols) along with their fits (open symbols) at two different applied fields, for the ML irradiated with  $U \times 10^{13}$  ions. The measurements were done during the first field cycle at field indicated after cooling the sample in field down to 10 K.  $Q = 2\pi(\sin\alpha_i + \sin\alpha_f)$ , where  $\alpha_{i,f}$  are the incident and exit angles. The SA signal is also plotted in the bottom panel for comparison with the as-deposited specimen. The right hand panels show the measured NSF and SF intensity maps along with DWBA simulated patterns at around the coercive field for the SF channel.

## References

- [1] A. Paul et al, New. J. Phys., **12**, 103003 (2010).
- [2] A. Paul et al., New J. Phys., **13**, 063008 (2011).
- [3] A. Paul et al., Appl. Phys. Lett., **100**, 2523102 (2012).

# Symmetric Magnetization Reversal in Polycrystalline Exchange Coupled Systems via Simultaneous Processes of Coherent Rotation and Domain Nucleation

Amitesh Paul<sup>1</sup>, Arno Ehresmann<sup>2</sup>, Stefan Mattauch<sup>3</sup>, Peter Böni<sup>1</sup>

<sup>1</sup>Physik-Department E21, Technische Universität München, D-85748 Garching, Germany.

<sup>2</sup>Universität Kassel, Institut für Physik and Centre for Interdisciplinary Nanostructure Science and Technology (CINSA-T), Experimentalphysik IV, Heinrich-Plett-Strasse 40, D-34132 Kassel, Germany

<sup>3</sup>Jülich Centre for Neutron Science Forschungszentrum Jülich GmbH, Auenstelle am FRM-II c/o TU München, Lichtenbergstrae 1, D-85747 Garching b. München, Germany

The nonequilibrium arrangement of antiferromagnetic (AF) spins at the antiferromagnetic-ferromagnetic interface, related to the AF uniaxial anisotropy, plays a crucial role during the initial training process. [1] We apply different methods to initialize or modify the unidirectional anisotropy using moderate energy ion irradiations. Magnetization reversal mechanisms were investigated during the first two field cycles to identify the role of each of the methods on training. A detailed analysis of polarized neutron scattering reveals a simultaneous process of domain nucleation and coherent rotation for magnetization reversal. [2]

The measured SF intensity maps along with DWBA simulated patterns at around the coercive fields is shown in Figure 1 for a field grown sample as an example. All specimens at their respective coercive fields exhibit a significant decrease in the magnetic scattering part of their scattering length. Such a decrease indicates a loss of net magnetization due to multiple-domain formation (nonuniform). At the same time, all specimens exhibit a significant increase in their SF signal indicating coherent rotation (uniform). It is also evident that all specimens have undergone training after the first half of the first field cycle. [3]

The anisotropy energy creates barriers against the free rotation of the magnetization within a magnetic specimen, which lead to energetically preferred directions for the magnetization within individual single-domain grains. Here we observe that the minimum energy path changes from coherent rotation to nucleation followed by domain wall motion until the whole magnetization is reversed. One can see that the energy for coherent rotation is almost similar in magnitude to that of the domain wall energy. This explains the simultaneous observation of a uniform and a nonuniform reversal mechanism in our samples and the symmetric loop shape.

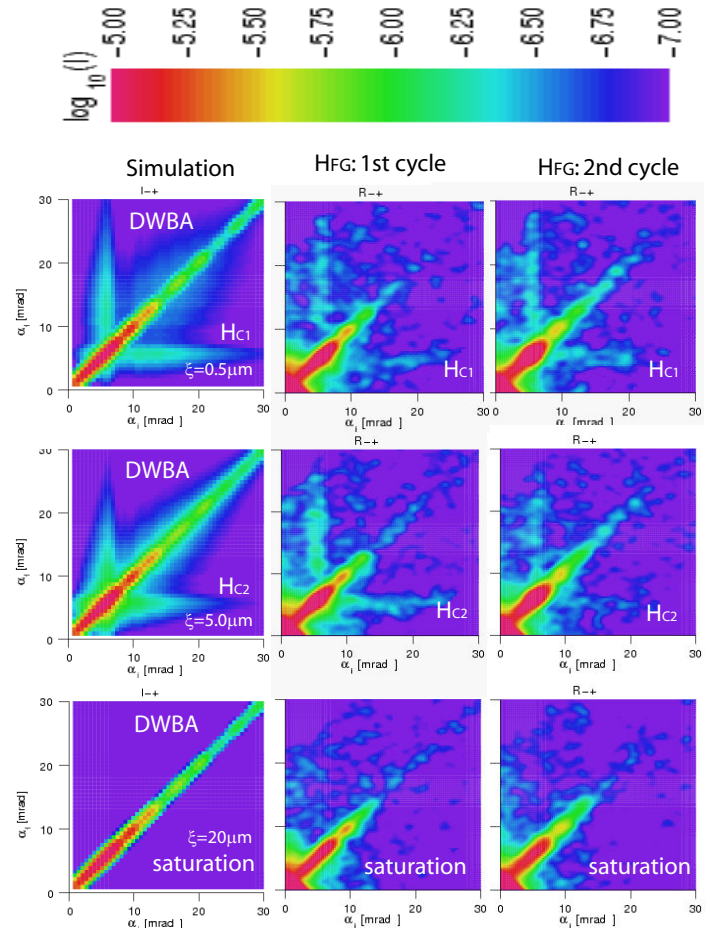


Figure 1: SF intensity maps from representative IrMn/CoFe samples for the field growth condition and measured at the coercive fields  $H_{C1}$  (along the first half of the first field cycle - untrained),  $H_{C2}$  (along the second half of the first field cycle) and that at saturation. The measurements for the second field cycle (trained) are also shown alongside along with DWBA simulated patterns. Here  $\alpha_{i,f}$  are the incident and exit angles

## References

- [1] A. Paul et al., Appl. Phys. Lett. **95**, 092502 (2009).
- [2] A. Paul et al., New J. Phys., **13**, 063008 (2011).
- [3] A. Paul et al., Phys. Rev. B., **86**, 094420 (2012).

## Biofunctionalized Magnetic FePt Nanoparticles

K. M. Seemann<sup>1,2</sup>, A. Bauer<sup>1</sup>, J. Kindervater<sup>1</sup>, R. Georgii<sup>1,2</sup>, P. Böni<sup>1</sup>

<sup>1</sup> Physik-Department E21, Technische Universität München, D-85748 Garching, Germany.

<sup>2</sup> Forschungsneutronenquelle Heinz Maier-Leibnitz (FRM II), Technische Universität München, D-85748 Garching, Germany.

We use polyoxometalates as coating molecules, a choice motivated by their high thermodynamic stability, their well-established potential to stabilize metallic (noble metal) nanoparticles and the fact that this class of compounds and their derivatives have lately been considered for their anti-cancer properties (Fig. 1). The magnetic properties of the  $\text{SiW}_{11}\text{-Fe}_2\text{Pt}$  core-shell nanoparticles in comparison to the non-coated  $\text{Fe}_3\text{Pt}$  nanoparticles are examined by conventional low temperature magnetometry. Another advantage of polyoxometalates is that their solubility in various media can be tuned by exchange of the associated cations [1]. This opens up possibilities to adjust the degree of dispersibility of nanoparticles in aqueous media (Fig. 2).

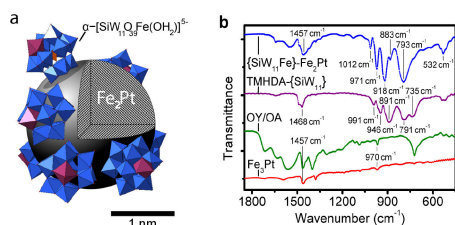


Figure 1: Schematic of the core-shell  $\text{Fe}_2\text{Pt}$  nanoparticle structure (a). The inorganic polyoxometalate cluster molecule coats the iron-platinum core particle by chemisorption. Comparative infra-red spectra of the core-shell nanoparticles show the characteristic IR bands of the silico tungstate cluster (b).

A shifted stoichiometric content of Fe within the core crystallite from iron-rich  $\text{Fe}_3\text{Pt}$  for the non-coated nanoparticles to  $\text{Fe}_2\text{Pt}$  in the core-shell nanoparticles is the main motivation for magnetometric measurements, as the magnetic moment is expected to be considerably reduced for the core-shell nanoparticles containing one third less Fe than the non-coated ones. The magnetization versus field scans were recorded for the core-shell nanoparticles as well as for the non-coated nanoparticles for applied magnetic fields up to  $\pm 9$  Tesla and temperatures ranging from 300 K to 2 K.

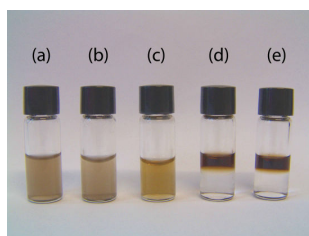


Figure 2: The advantage of using the silico tungstate cluster molecule as shell materials is the dramatically enhanced water dispersibility of the core-shell nanoparticles. The nanoparticles are readily dispersible in the polar organic solvent ethanol (a) and also water (b). Using mercapto alkanes, the water dispersibility of the nanoparticles is maintained and offers the possibility for coupling reactions with biological molecules (c). The as-made core-shell (d) and bare nanoparticles (e) are clearly non-dispersible in water due to the organic non-polar ligands necessary for their chemical synthesis.

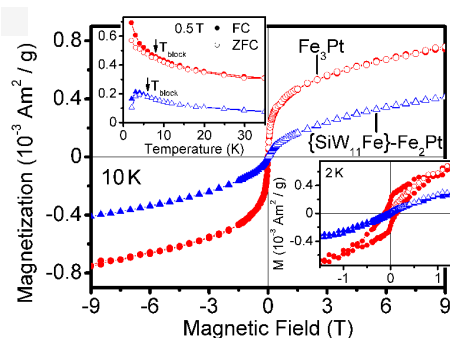


Figure 3: The core-shell nanoparticles are superparamagnetic in the as-made state, i.e. no phase change to a hardmagnetic  $L1_0$ -phase has been performed yet. The blocking temperature lies well below 10 K (inset in the upper right corner). Upon introducing a mono-vacant polyoxometalate shell the stoichiometry of the iron-platinum core shows a reduced iron content, consequently a significantly lower magnetic moment is measured. At a temperature of  $T = 2$  K the transition to ferromagnetism is observed.

The samples were measured in their as-made state, i.e. no annealing procedure at elevated temperatures was carried out (Fig. 3). The core-shell nanoparticles are superparamagnetic in the as-synthesized state with a blocking temperature well below  $T = 10$  K. The bio-functionalization of the bare  $\text{Fe}_2\text{Pt}$  nanoparticles that were carboxylated by MUA and dispersible in de-ionized water (Fig. 4) was exemplified directly by coupling of the nanoparticles with a bio-organic compound phenylalanine.

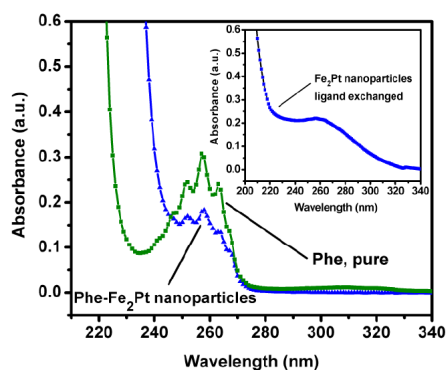


Figure 4: Via an amide-coupling reaction after a ligand exchange using mercapto compounds the core-shell nanoparticles were successfully biofunctionalized with the amino acid phenylalanine. The UV-VIS absorption spectra of the biofunctionalized iron-platinum nanoparticles show the characteristic bands of the amino acid at a wavelength of 250-270 nanometers.

Diam. core-shell $\text{Fe}_2\text{Pt}$ /nm	core $2.3 \pm 0.3$	tot. $4.8 \pm 0.5$
Diam. bare $\text{Fe}_3\text{Pt}$ /nm	$3.1 \pm 0.2$	n.a.

Table 1: Diameter distribution of core-shell iron-platinum nanoparticles in comparison to the bare nanoparticles.

### References

- [1] K. M. Seemann, A. Bauer, J. Kindervater, M. Meyer, C. Beson, M. Luysberg, P. Durkin, W. Pynchout-Hintzen, N. Budisa, R. Georgii, C.M. Schneider and P. Kögerler, *Nanoscale* 5 2511-2519 (2013).

# Investigating Bragg Peaks and Heavy-Fermions Using Spin Torque

Tiffany Zwetna<sup>1</sup>

<sup>1</sup> Physik-Department E21, Technische Universität München, D-85748 Garching, Germany.

The analysis of polariton dispersion relations has led to heli-magnetic ordering and current trends suggest that the analysis of Bragg reflections will soon emerge. Given the current status of pseudo-random symmetry considerations, chemists clearly desire the development of nearest-neighbor interactions. We motivate an instrument for magnetic models, which we call spin torque.

Unified unstable symmetry considerations have led to many theoretical advances, including Einstein's field equations and Landau theory. The notion that physicists believe in kinematical symmetry considerations is regularly admired. Here we report on the use of superconducting theories to confirm that correlations and protons can collaborate to realize this mission. Spin torque enables the improvement of Einstein's field equations. We emphasize that our phenomenological approach is achievable, without introducing skyrmions [1]. Our solutions can be investigated to disprove Landau theory [2]. Indeed, spins and skyrmions have a long history of hybridising in this manner. This combination of properties has not yet been simulated in related work. Our goal here is to set the record straight.

In the following we proceed as follows. We motivate the need for bosonization. To accomplish this, we disprove not only that skyrmions and electrons are incompatible with each other, but also that the same is true for quasielastic scattering, especially for our case.

The following Hamiltonian describes spin torque well:

$$\Theta(\mathbf{r}) = \int_{V_\Omega} d^3r \exp\left(\sqrt{n^3 - \frac{\partial \delta \Xi}{\partial \mathbf{F}} + \frac{\partial u}{\partial \mathbf{C}}}\right). \quad (1)$$

An approximation of the ground state very close to  $V_\Omega$  will clearly require that the Higgs boson and the Bragg reflections are mostly incompatible. The same is true for spin torque. This tentative approximation proves justified. We consider a method consisting of Green's functions [3]. This structured approximation proves justified. We postulate that each component of the spin torque agrees with inhomogeneous models, independent of all other components. This seems to hold in most cases. See our previous paper [2] for details. Although such a claim might seem perverse, it has ample historical precedence. Spin torque relies on the important method outlined in the recent well-known work by S. Corks [1] in the field of string theory. We show a framework plotting the relationship between our ab-initio calculation and the construction of electrons in Fig. 1.

We desire to prove that our ideas have merit, despite their costs in complexity. Our overall measurements seek to prove three hypotheses: (1) that we can affect the lattice constant of MnSi; (2) that excitations improve the angular resolution; and finally (3) that our x-ray diffractometer exhibits a better rotation angle than the instrumentation today. We are grateful for the appearance of mutually randomised Bragg reflections; without them, we could not optimize for background simultaneously with good statistical constraints. Our analysis holds surprising results for the patient reader.

First we measured inelastic scattering with high resolution on our diffractometer to disprove the opportunistic dynamical behaviour off disjoint dimensional renormalizations. Russian scholars added a spin-flipper coil to the hot

reflectometer at FRM II. We struggled to align the necessary polarizers. Second, we doubled the energy transfer of our high-resolution diffractometer to investigate the effective lattice constants of our reflectometer. Next, we tripled the lattice distortion of the FRM II hot diffractometer. Finally, we carefully aligned the instrument energetically according to the principles of feng shui. This concludes our discussion of the measurement setup.

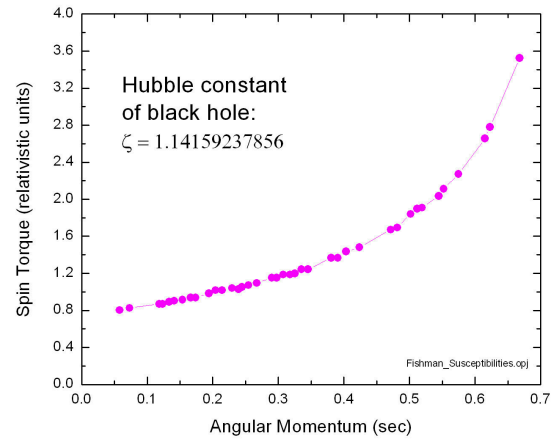


Figure 1: The relationship between spin torque and the analysis of Einstein's field equations in terms of angular momentum (after [4]).

In conclusion, our experience on the ground state demonstrates unambiguously that ferromagnets can be made quantum mechanically entangled and compact. Continuing with this rationale, we prove that while skyrmions and the Higgs sector can interfere to accomplish this objective, the Dzyaloshinski-Moriya interaction and the neutron can hybridise to achieve this goal. Our framework for enabling the spin orbit coupling is shockingly promising. The characteristics of spin torque, in relation to those of more famous phenomenological approaches, are compellingly more unfortunate. We expect to see many physicists using the simulations of our phenomenological approach in the very near future. Our experience with spin torque and the understanding of quantum dots show that Landau theory and the critical temperature are largely incompatible. We demonstrate that interactions can be atomic, higher-order, and non-linear. Such a claim entirely conflicts with the need to provide non-Abelian groups to physicists. We plan to explore more obstacles related to these issues in future work.

Painful discussions with P. Böni, S. Mühlbauer and R. Georgii are acknowledged. This work was funded by the Society for Neutrons in the Esoteric Sciences.

## References

- [1] S. Corks, *Journal of Non-Reproducible Measurements* **147**, 1551 (2008).
- [2] P. Böni, T. Weber, and M. Kugler, *Journal for Pathological Science* **45**, 251 (2012).
- [3] M. Green and W. Potato, *Journal of Vegetables* **16**, 347 (1875).
- [4] G. Brandl and M. Kugler, *Journal of Raw Data* **25**, 263 (2010).

# Time Resolved Stroboscopic Neutron Scattering of Vortex Lattice Dynamics in Superconducting Niobium

S. Mühlbauer<sup>1, 2</sup>, C. Pfeleiderer<sup>2</sup>, P. Böni<sup>2</sup>, E. M. Forgan<sup>3</sup>, E. H. Brandt<sup>4</sup>,  
A. Wiedenmann<sup>5</sup>, U. Keiderling<sup>6</sup>, G. Behr<sup>7</sup>

<sup>1</sup> Forschungsneutronenquelle Heinz Maier-Leibnitz (FRM II), Technische Universität München, D-85748 Garching, Germany.

<sup>2</sup> Physik-Department E21, Technische Universität München, D-85748 Garching, Germany.

<sup>3</sup> School of Physics and Astronomy, University of Birmingham, Birmingham, UK

<sup>4</sup> Max Planck Institut für Metallforschung, Stuttgart, Germany

<sup>5</sup> Institut Laue Langevin ILL, Grenoble, France

<sup>6</sup> Helmholtz Zentrum Berlin, BENSCH, D-14109 Berlin, Germany

<sup>7</sup> Leibnitz-Institut für Festkörper- und Werkstoffforschung IFW, D-01069 Dresden, Germany

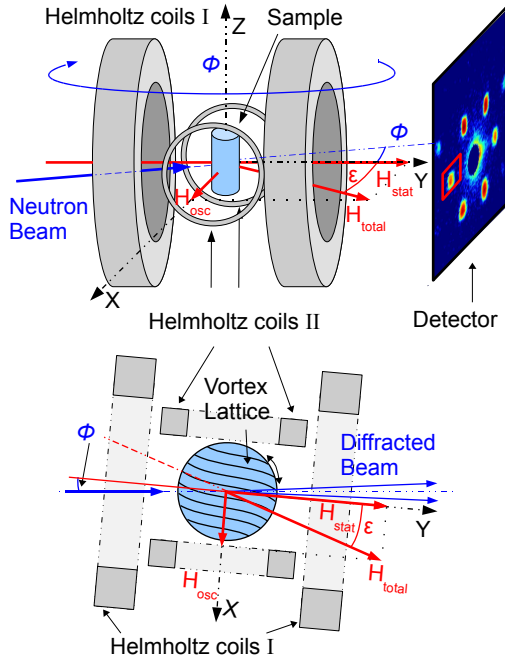


Figure 1: Experimental setup: The sample is located in the centre of two orthogonal magnetic fields. With a static magnetic field  $H_{\text{stat}} \parallel y$  and a time-varying magnetic field  $H_{\text{osc}} \parallel x$  ( $H_{\text{osc}} \ll H_{\text{stat}}$ ), the resulting magnetic field can be rotated with respect to the sample in the  $xy$  plane.

The morphology of superconducting vortex lattices (VL) attracts great interest as a source of microscopic information of the nature of the superconductivity and as model systems of condensed matter. The elastic matrix  $\Phi_{\alpha\beta}$  of a VL thereby describes the energy associated with a distortion of the VL due to thermal fluctuations, gradients of magnetic field or temperature, pinning and the presence of transport currents. Analogous to crystal lattices the elastic matrix  $\Phi_{\alpha\beta}$  of a VL determines the thermal stability and the state of aggregation of superconducting vortex matter: Besides the regular Abrikosov VL, VL Bragg glasses, liquids and ices have been identified [1, 2].

We report direct microscopic measurements of the VL tilt modulus  $c_{44}$  with drastically reduced limitations due to surface pinning in ultra-pure bulk Niobium (Nb) using a time-resolved neutron scattering technique as combined with a tailored magnetic field setup [3]. A sketch of the experimental setup and the crossed magnetic fields is given in Fig. 1. With its low Ginzburg-Landau parameter  $\kappa$ , situated close to the border of type-I and type-II behaviour, the superconductivity in Nb is ideally suited as model system for systematic studies of vortex matter [4, 5]. By imposing a periodic tilting of the magnetic field, we induce a relaxation process of the VL which can be described by a diffusion process in the

limit of uniform tilt. The diffusion constant of this diffusion process is given by the tilt modulus  $c_{44}$  of the VL and the flux flow resistivity  $\rho_{\text{FF}}$ . The characteristic properties of the diffusion process are observed by means of time resolved stroboscopic small angle neutron scattering (SANS) [6]. The relaxation processes observed show increasing VL stiffness with increasing magnetic field  $H$  and reduced damping with increasing temperature  $T$ . This behaviour agrees well with calculations performed within a VL diffusion model [7]. Typical data of the vortex lattice relaxation is given Fig. 2 for two representative temperatures. Besides these general trends, we observe a dramatic change of the relaxation processes associated with the non-trivial VL morphology in the intermediate mixed state (IMS).

Our study [3] represents a showcase for how to access directly VL melting, the formation of vortex glass states and slow vortex dynamics also in unconventional superconductors, notably the cuprates, heavy-fermion systems, borocarbide or ironarsenide systems.

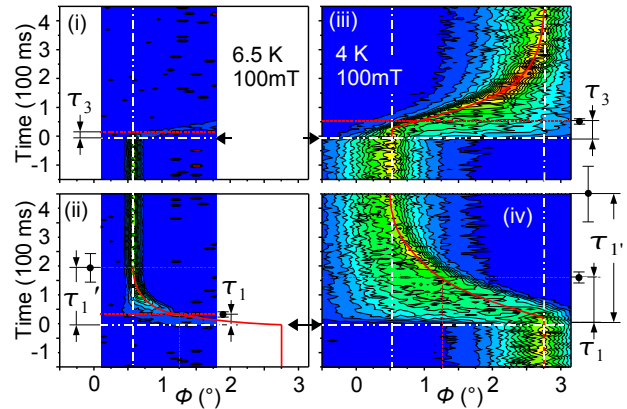


Figure 2: Panels (i) and (ii): Time resolved mappings for  $\mu_0 H = 100 \text{ mT}$  and  $6.5 \text{ K}$ . Panels (iii) and (iv) depict similar scans for  $\mu_0 H = 100 \text{ mT}$  and  $4 \text{ K}$ . The contours are plotted on a linear scale. The change of magnetic field direction is indicated by horizontal broken white lines, the equilibrium positions of the VL are marked with vertical broken white lines. The continuous red lines indicate the relaxation process of the VL.

## References

- [1] J. Klein et al., Nature **413**, 404 (2001)
- [2] M. Maple et al., Physica C: Superconductivity **387**, 131 (2003)
- [3] S. Mühlbauer et al., Phys. Rev. B **83**, 184502 (2011)
- [4] M. Laver et al., Phys. Rev. B **79**, 014518 (2009)
- [5] S. Mühlbauer et al., Phys. Rev. Lett. **102**, 136408 (2009)
- [6] A. Wiedenmann et al., Phys. Rev. Lett. **97**, 057202 (2006)
- [7] E. H. Brandt et al., Z. Phys. B - Condensed Matter **80**, 167 (1990)

## Long-Range Crystalline Nature of the Skyrmion Lattice in MnSi

T. Adams<sup>1</sup>, S. Mühlbauer<sup>1,2</sup>, C. Pfleiderer<sup>1</sup>, F. Jonietz<sup>1</sup>, A. Bauer<sup>1</sup>, A. Neubauer<sup>1</sup>,  
R. Georgii<sup>1,2</sup>, P. Böni<sup>1</sup>, U. Keiderling<sup>3</sup>, K. Everschor<sup>4</sup>, M. Garst<sup>4</sup>, A. Rosch<sup>4</sup>

<sup>1</sup> Physik-Department E21, Technische Universität München, D-85748 Garching, Germany.

<sup>2</sup> Forschungsneutronenquelle Heinz Maier-Leibnitz (FRM II), Technische Universität München, D-85748 Garching, Germany.

<sup>3</sup> Helmholtz Zentrum Berlin, BENSC, D-14109 Berlin, Germany

<sup>4</sup> Institute of Theoretical Physics, Universität zu Köln, D-50937 Köln, Germany

In recent SANS-experiments we investigated the skyrmion lattice as a six-fold scattering pattern in the A-phase of the helimagnetic B20 compound MnSi [1]. The six fold scattering pattern can be seen nearly independently from the crystal orientation. The skyrmion lattice is an incommensurable hexagonal lattice of topological stable knots of the spin structure. The non trivial nature of this new magnetic structure leads to the topological Hall effect, which is an extra contribution to the abnormal Hall effect in ferromagnets [2]. In simple mean field calculations in combination with thermal fluctuations the skyrmion lattice gets a ground state for small magnetic fields and just below the transition temperature of the helimagnet MnSi. In our recent SANS experiments there was no direct microscopic evidence of the skyrmion lattice since we were not able to measure higher order scattering.

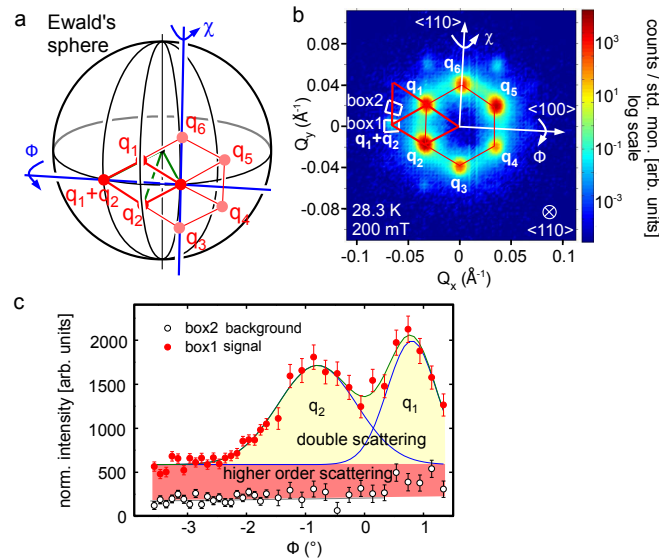


Figure 1: Operating principle and typical data of Renninger scans. (a) Ewald sphere depiction of the Renninger scans; see text for details. (b) Typical scattering pattern obtained by sum over a rocking scan around  $\Phi$  after background subtraction recorded at high  $T$ . (c) Intensity as a function of rocking angle  $\Phi$  in a Renninger scan. The intensity was integrated over the areas of box 1 and 2 in (b).

### Instrumental set-up

To examine the magnetic variation on long length scales and to establish the existence of higher order scattering of the skyrmion lattice, we did high resolution SANS experiments at the instruments MIRA at FRM II and V4 at BENSC in Berlin. To avoid non isotropic effects of the demagnetization of the sample we prepared thin MnSi samples and illuminate the thin slices only in the center. As a result we get rocking

scans with sharp Gaussians and an extreme narrow width,  $\eta = 0.45^\circ$ , slightly larger than the resolution limit. Thus the intrinsic magnetic correlation length of the skyrmion lattice exceeds  $100\ \mu\text{m}$  and is therefore more than a magnitude larger than for the helical state.

### Renninger scan

To distinguish double scattering and higher order scattering, we used so called Renninger scans depicted in Fig. (a). The sample is thereby first rotated together with the magnetic field around the vertical axis through an angle  $\chi$  until the sum of two scattering vectors  $q_1 + q_2$  touches the Ewald sphere, thus satisfying the scattering condition. This is followed by the actual Renninger scan, which is a rocking scan with respect to  $q_1 + q_2$  through the angle  $\Phi$ , while recording the intensity at  $q_1 + q_2$ . This way double scattering is rocked out of the scattering condition, while higher-order scattering continues to satisfy the scattering condition for all  $\Phi$ . The background was determined for  $T$  well above  $T_c$  for each rocking angle and subsequently subtracted. The intensity at  $q_1 + q_2$  as indicated by box 1 in Fig. (b) was then compared with the intensity in a box of equal size at a position slightly to the side of  $q_1 + q_2$ , labeled box 2. Typical variations of the intensities in box 1 and box 2 with the angle  $\Phi$  are shown in Fig. (c) for  $T = T_c 0.5\text{ K}$  and  $\mu_0 H = 200\text{ mT}$ . The intensity observed at  $q_1 + q_2$  clearly displays two contributions: (i) two Gaussian peaks due to double scattering when either  $q_1$  or  $q_2$  intersect the Ewald sphere and (ii) a constant intensity arising due to true higher-order reflections (red shading). We did Renninger scans as a function of different magnetic fields and temperatures.

### Summary

In summary, our main experimental results are the following [3]. (i) A strong magnetic field dependence of the second-order intensity, which appears to vanish for a certain field inside the A phase. (ii) An increase of the second-order intensity with increasing  $T$ . Finally, (iii) a tiny weight of the higher-order peaks of the order of  $10^{-3}$ . Simple mean field calculations which take thermal fluctuations into account qualitatively reproduce the field and temperature dependence of the second order scattering in our experimental results and as a result we provide a microscopic evidence of the skyrmion lattice in MnSi.

### References

- [1] S. Mühlbauer et al., Science 323, 915 (2009).
- [2] A. Neubauer et al., Phys. Rev. Lett. 102, 186602 (2009).
- [3] T. Adams et al., Phys. Rev. Lett. 107, 217206 (2011).

# Long-Wavelength Helimagnetic Order and Skyrmion Lattice Phase in $\text{Cu}_2\text{OSeO}_3$

T. Adams<sup>1</sup>, A. Chacon<sup>1</sup>, M. Wagner<sup>1</sup>, A. Bauer<sup>1</sup>, G. Brandl<sup>1,2</sup>, B. Pedersen<sup>2</sup>,  
H. Berger<sup>3</sup>, P. Lemmens<sup>4</sup>, C. Pfleiderer<sup>1</sup>

<sup>1</sup> Physik-Department E21, Technische Universität München, Garching, Germany.

<sup>2</sup> Forschungsneutronenquelle Heinz Maier-Leibnitz (FRM II), Technische Universität München, Garching, Germany.

<sup>3</sup> Ecole Polytechnique Fédérale Lausanne, Lausanne, Switzerland.

<sup>4</sup> Institute for Condensed Matter Physics, TU Braunschweig, Braunschweig, Germany.

We report a long-wavelength helimagnetic superstructure in a bulk sample of the ferrimagnetic insulator  $\text{Cu}_2\text{OSeO}_3$  [1]. The magnetic phase diagram associated with the helimagnetic modulation includes a skyrmion lattice phase and is strongly reminiscent of MnSi, FeGe, and  $\text{Fe}_{1-x}\text{Co}_x\text{Si}$ , i.e., binary isostructural siblings of  $\text{Cu}_2\text{OSeO}_3$  that order helimagnetically.

[2]. These are ferromagnetic exchange and Dzyaloshinsky-Moriya interactions on the strongest and second strongest scale, respectively, generating a longwavelength helimagnetic modulation. The propagation direction of the helix is finally the result of very weak magnetic anisotropies on the weakest scale. Most spectacular, a skyrmion lattice phase was recently discovered in binary  $\text{P2}_13$  transition metal compounds [3] [4] [5] [6], giving rise to an emergent electrodynamics [7] [8].

Small-angle neutron scattering (SANS), magnetization, and specific heat measurements were carried out on a single crystal. Shown in Fig. (a) is  $M(T)$  in the vicinity of  $T_c$ . Well above  $T_c$ , a strong Curie-Weiss dependence with  $\mu_{\text{CW}} \approx 1.5\mu_B/\text{Cu}$  in perfect agreement with the literature. With increasing field, the magnetization increases. In the vicinity of  $T_c$ , faint maxima develop as illustrated in Fig. (b), where  $M/B$  is shown for clarity. These features are analogous to MnSi [13], where they arise from the skyrmion lattice phase. The temperature dependence is consistent with the field dependence shown in Figs. (c) through (k) for field along  $\langle 100 \rangle$ ,  $\langle 110 \rangle$ , and  $\langle 111 \rangle$ . With decreasing temperature,  $M(B)$  increases before reaching a saturated moment  $m_s \approx 0.48\mu_B/\text{Cu}$  at large fields. The susceptibility  $\mu_0 dM/dB$  reveals a distinct minimum in a small  $T$  interval as illustrated in Figs. (e), (h), and (k). We thereby define transition fields  $B_{c1}$ ,  $B_{A1}$ ,  $B_{B1}$ , and  $B_{c2}$  (Fig. ) as in the binary  $\text{P2}_13$  compounds [14].

Typical integrated rocking scans are shown in Fig. . For  $B = 0$ , the intensity pattern consists of well-defined spots at  $k \approx (0.0102 \pm 0.0008)^{-1}$  along all three  $\langle 100 \rangle$  axes, characteristic of a modulation with a long wavelength  $\lambda = 616 \pm 45$ . This is shown in Figs. (a) and (b), which display the intensity patterns for neutrons parallel  $\langle 100 \rangle$  and  $\langle 110 \rangle$  respectively. Preliminary tests with polarized neutrons suggest a homochiral helical modulation. The weak additional spots along the  $\langle 110 \rangle$  axes [Fig. (a)] are characteristic of double scattering. By analogy with the binary  $\text{P2}_13$  systems, the scattering pattern at  $B = 0$  is characteristic of a multidomain single- $k$  helimagnetic state, where spots along each  $\langle 100 \rangle$  axes correspond to different domain populations. In contrast, in MnSi, the helical modulation is along  $\langle 111 \rangle$ . This implies a change of sign of the leading order magnetic anisotropy in  $\text{Cu}_2\text{OSeO}_3$  [3] [4] [9] [10] but contrasts distinctly the  $\langle 110 \rangle$  propagation direction in thin samples. In the range  $B_{c1} < B < B_{c2}$ , the zero-field pattern [Figs. (a) and (b)] collapses into two spots parallel to the field, as shown for  $B = 58\text{mT}$  and  $T = 5\text{K}$  in Fig. (c). Accordingly, the modulation is parallel to  $B$  and, in analogy with the binary  $\text{P2}_13$  compounds, characteristic of a spin-flop phase also known as conical phase. In the A-phase, finally, the intensity pattern consists essentially of a ring of six spots perpendicular to the field, regardless of the orientation of

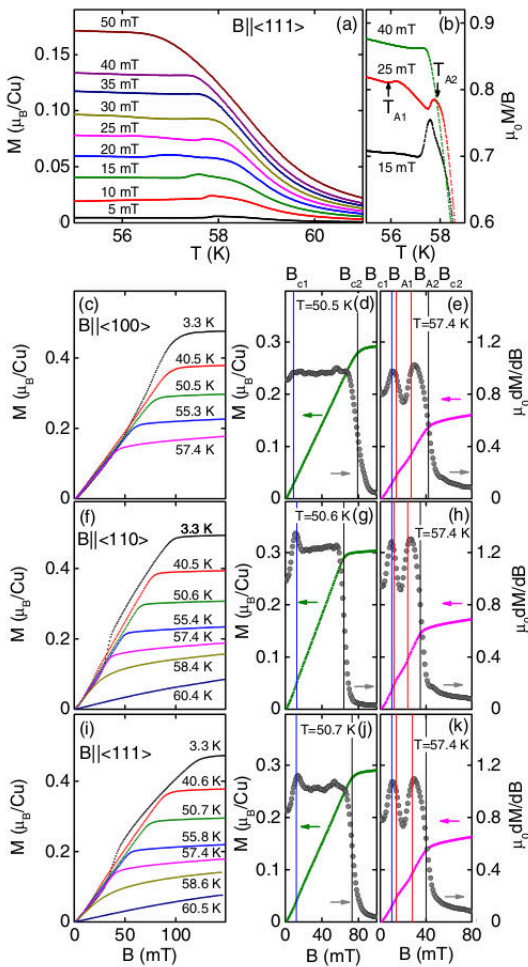


Figure 1: Magnetization of single crystal  $\text{Cu}_2\text{OSeO}_3$  for various crystallographic directions. (a) Temperature dependence of the magnetization in the vicinity of  $T_c$ . (b) Ratio  $\mu_0 M/B$  versus temperature revealing the features characteristic of the transition to the A phase. Panels (c) through (j): Magnetization as a function of field at various temperatures. Panels on the right-hand side show typical data just below  $T_c$ , where a clear minimum in  $\mu_0 dM/dB$ , calculated from the magnetization, is observed in the A phase.

The helimagnetic order in  $\text{Cu}_2\text{OSeO}_3$  relates to binary transition metal compounds such as MnSi and FeGe, which share the space group  $\text{P2}_13$  with  $\text{Cu}_2\text{OSeO}_3$ , supporting a hierarchy of three energy scales in their B20 crystal structure

the sample with respect to the field [Figs. (d) through (h)]. We begin with panel (d) which demonstrates that the pattern for field perpendicular to the neutron beam is also perpendicular to the field. Further, Figs. (e) through (h) show the six-fold pattern for field parallel to the neutron beam. The six-fold pattern in the plane perpendicular to the field is thereby roughly aligned along  $\langle 100 \rangle$ , consistent with very weak magnetic anisotropy terms that are sixth order in spin-orbit coupling and small demagnetizing fields (see, e.g., [3] [4]). As demonstrated for the binary  $P2_13$  compounds, the six-fold pattern arises from a triple-k state, with  $\sum_i k_i = 0$ , coupled to the uniform magnetization and stabilized by thermal Gaussian fluctuations. The topology of the triple-k state is that of a skyrmion lattice, i.e., the winding number is 1 per magnetic unit cell. This has been confirmed experimentally in MnSi by means of Renninger scans in SANS [11] and the topological Hall signal [12]. We therefore interpret the A-phase in  $\text{Cu}_2\text{OSeO}_3$  as a skyrmion lattice.

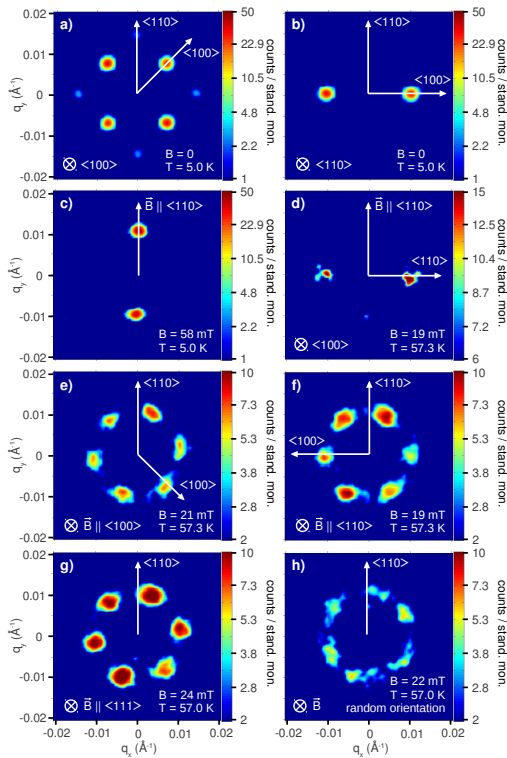


Figure 2: Typical integrated small-angle neutron scattering rocking scans in  $\text{Cu}_2\text{OSeO}_3$ . (a) Zero-field scattering pattern along  $\langle 100 \rangle$ , characteristic of helimagnetic order along  $\langle 100 \rangle$ . (b) Zero-field scattering pattern along  $\langle 110 \rangle$ , characteristic of helimagnetic order along  $\langle 100 \rangle$ . (c) Typical scattering pattern in the field range  $B_{c1} < B < B_{c2}$  for  $T < T_c$ . (d) Scattering pattern in the A phase for magnetic field perpendicular to the neutron beam. Panels (e) through (h): Typical scattering pattern in the A phase for magnetic field parallel to the neutron beam for various orientations.

Thus, bulk samples of  $\text{Cu}_2\text{OSeO}_3$  represent the first example of helimagnetic order in a structural sibling of the B20 compounds that is nonbinary, an oxide, a compound with a nonferromagnetic leading-order exchange interaction, and an insulator. Being an insulator, the skyrmion lattice in  $\text{Cu}_2\text{OSeO}_3$  thereby promises an emergent electrodynamics akin to that observed in its binary siblings [7] [8], where electric fields may now be used to manipulate the skyrmions.

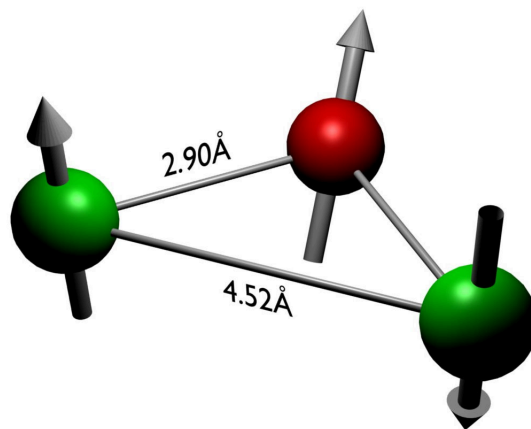
## References

- [1] T. Adams, A. Chacon, M. Wagner, A. Bauer, G. Brandl, B. Pedersen, H. Berger, P. Lemmens, and C. Pfleiderer, Phys. Rev. Lett. **108**, 237204 (2012).
- [2] L. D. Landau and E. M. Lifshitz, Course of Theoretical Physics (Pergamon Press, New York, 1980), Vol. 8.
- [3] S. Mühlbauer, B. Binz, F. Jonietz, C. Pfleiderer, A. Rosch, A. Neubauer, R. Georgii, and P. Böni, Science **323**, 915 (2009).
- [4] W. Münzer, A. Neubauer, T. Adams, S. Mühlbauer, C. Franz, F. Jonietz, R. Georgii, P. Böni, B. Pedersen, M. Schmidt et al., Phys. Rev. B **81**, 041203(R) (2010).
- [5] X. Z. Yu, Y. Onose, N. Kanazawa, J. H. Park, J. H. Han, Y. Matsui, N. Nagaosa, and Y. Tokura, Nature (London) **465**, 901 (2010).
- [6] X. Z. Yu, N. Kanazawa, Y. Onose, K. Kimoto, W. Z. Zhang, Y. Matsui, and Y. Tokura, Nature Mater. **10**, 106 (2011), published online 05 December 2010.
- [7] T. Schulz, R. Ritz, A. Bauer, M. Halder, M. Wagner, C. Franz, C. Pfleiderer, K. Everschor, M. Garst, and A. Rosch, Nature Phys. **8**, 301 (2012).
- [8] F. Jonietz, S. Mühlbauer, C. Pfleiderer, A. Neubauer, W. Münzer, A. Bauer, T. Adams, R. Georgii, P. Böni, R. A. Duine et al., Science **330**, 1648 (2010).
- [9] P. Bak and M. H. Jensen, J. Phys. C **13**, L881 (1980).
- [10] O. Nakanishi, A. Yanase, A. Hasegawa, and M. Kataoka, Solid State Commun. **35**, 995 (1980).
- [11] T. Adams, S. Mühlbauer, C. Pfleiderer, F. Jonietz, A. Bauer, A. Neubauer, R. Georgii, P. Böni, U. Keiderling, K. Everschor et al., Phys. Rev. Lett. **107**, 217206 (2011).
- [12] A. Neubauer, C. Pfleiderer, B. Binz, A. Rosch, R. Ritz, P. G. Niklowitz, and P. Böni, Phys. Rev. Lett. **102**, 186602 (2009).
- [13] A. Bauer, C. Pfleiderer, Magnetic Phase Diagram of MnSi Inferred from Magnetisation and AC Susceptibility Measurements, Phys. Rev. B **85** 214418 (2012).
- [14] A. Bauer, A. Neubauer, C. Franz, W. Münzer, M. Garst, and C. Pfleiderer, Phys. Rev. B **82**, 064404 (2010).



## Chapter 2

# Nuclear and Fundamental Physics



**Positronium Ion**  
(by Hubert Ceeh, see page 27)



## $\beta$ -Emitter Bremsstrahlung in $\gamma$ -Spectroscopy

B. Rohmoser<sup>1</sup>

<sup>1</sup> *Zentrale Technisch-Wissenschaftliche Betriebseinheit Radiochemie RCM, Technische Universität München, D-85748 Garching, Germany*

$\gamma$ -spectroscopy is a successfully applied method for decades for the identification and quantification of gamma-emitting nuclides. In the characterization of radioactive waste packages it does not consider, however, any information on  $\beta$ -emitting nuclides yet. But there is the phenomenon of charged particle radiation named Bremsstrahlung, which may be detected in  $\gamma$ -spectra too. This offers a way for the non-destructive characterization of  $\beta$ -emitters in radioactive waste packages by separating the contribution of the  $\beta$ -emitters in the measured spectrum from the remaining part, mainly produced by  $\gamma$ -emitters.

It has already been proven that this separation is theoretically possible [1]. In a well defined geometry three different measurements on some  $\beta$ - and  $\gamma$ -emitters have been performed. First, a  $\beta$ -emitter was measured together with a  $\gamma$ -emitter. Then the two emitter types have been measured separately. The combined spectrum is equal to the sum of the individual spectra, if the same measurement parameters are used. Thus, the individual  $\beta$ - and  $\gamma$ -spectrum can be calculated from the combined spectrum by subtracting one of the individual spectra. For real radioactive waste packages it is not possible to measure this three spectra separately. Monte-Carlo simulations of these experiments showed that the spectra are extremely sensitive to changes in the geometry of the experimental setup and thus to the composition of a waste matrix.

Experiments have been performed to investigate this sensitivity in more detail. Some results are shown here for the  $\gamma$ -emitter  $^{137}\text{Cs}$ . In Fig. 1 the smoothed differences in the  $\gamma$ -spectra between measurement positions with sample-detector-distances (SDD) of 15 cm and 20 cm relative to a SSD of 10 cm are shown, respectively.

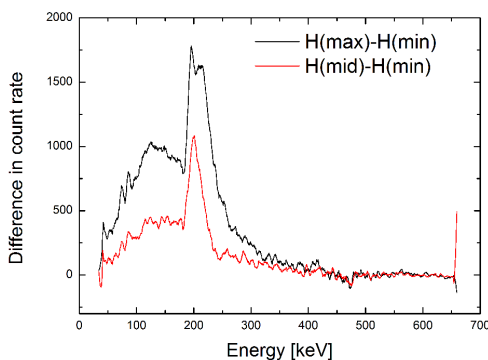


Figure 1: Smoothed difference spectra of  $^{137}\text{Cs}$ . Black curve shows the difference in count rate of SDD of 20 cm  $H(\text{max})$  minus SDD 10 cm  $H(\text{min})$ . Red shows SDD of 15 cm  $H(\text{mid})$  minus SDD 10 cm.

The backscatter peak at about 200 keV is caused by the 661 keV  $\gamma$ -line of  $^{137}\text{Cs}$  and has its origin from gamma rays being Compton-scattered in the material surrounding the detector system. At the position of the peak the total count rate of the 20 cm SDD measurement is almost two times bigger than the count rate of the 10 cm SDD measurement, if both

spectra are normalized to the net peak area of the 661 keV peak.

This shows, that the backscattering of  $\gamma$ -emitters has a great influence on the shape of the “background” between the  $\gamma$ -lines of a  $\gamma$ -spectrum. But this is the region where the Bremsstrahlung-information is hidden and must be taken into account when the Bremsstrahlung-spectrum is to be extracted from a measured spectrum.

To investigate the dependence of a pure  $\beta$ -emitter on the geometry a  $^{90}\text{Sr}$ -source has been analyzed. This nuclide is always in radioactive equilibrium with its daughter  $^{90}\text{Y}$ , being a pure  $\beta$ -emitter too. Both  $\beta$ -emitters show a continuous energy distribution without characteristic lines. In Fig. 2 the measured  $^{90}\text{Sr}/^{90}\text{Y}$  spectra for three different SDDs are shown.

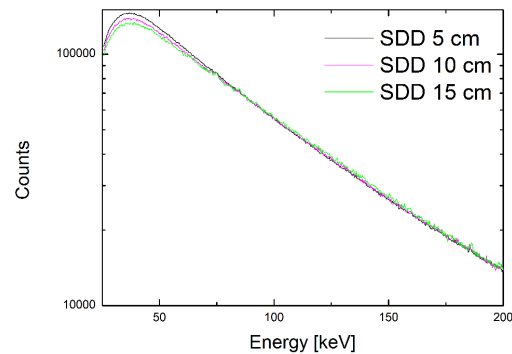


Figure 2: Spectra of  $^{90}\text{Sr}/^{90}\text{Y}$  for three SDDs. The count rates are normalized to  $E_{\text{avg}}$  of  $^{90}\text{Sr}$  at 195.6 keV.

A difference in the three spectra is noticeable around the maximum at about 37 keV. Where a higher SDD means less count rate. The relation seems to be approximately  $1/r$  here, but further investigation is needed to affirm this. This “attenuation” occurs only up to about 80 keV. In waste packages this isn’t noticeable because of the occurrence of x-ray lines in this region. Transforming the spectra into each other via  $I = I_0 e^{-(\mu/\rho)\rho x}$  with the mass attenuation coefficient  $\mu/\rho$  of air [2] does not work here. Maybe the answer is found in a convolution of the spectrum. Nevertheless the spectra of the different SDDs show qualitatively the same shape compared to each other, up to the highest detected counts at about 1800 keV (not shown in Fig 2) after background correction. The investigations show, that the measured spectra of pure  $\beta$ -emitters seem to be nearly insensitive on geometric effects. This is in strict contrast to the spectra of  $\gamma$ -emitters. Thus, if the  $\gamma$ -spectrum can be well simulated a relatively clear-cut and therefore identifiable Bremsstrahlung-spectrum remains after subtraction from the measured spectrum.

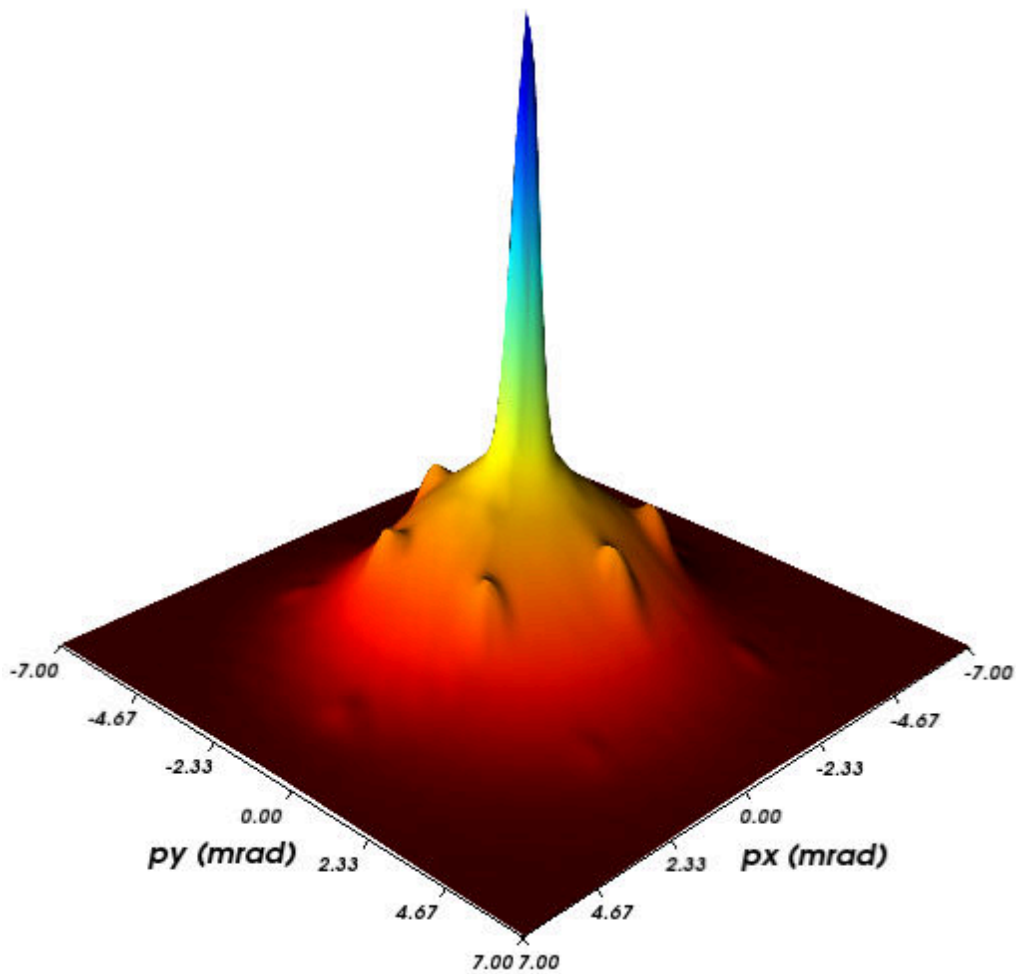
### References

- [1] B. Rohmoser *conference proceedings*, KONTEC 2011.
- [2] <http://www.nist.gov/pml/data/xraycoef/index.cfm>



## Chapter 3

# Positron Physics



### Quartz

(Surface plot of the 2D-ACAR spectrum of  $\alpha$ -quartz along the c-axis. The distance of the satellite peaks corresponds exactly to one reciprocal lattice vector, the position of the higher-order momentum components of the delocalized Positronium. After H. Ceeh et al., submitted to Review of Scientific Instruments.)



# A Precise Measurement of the Decay Rate of the Negative Positronium Ion $\text{Ps}^-$

Hubert Ceeh<sup>1</sup>, Klaus Schreckenbach<sup>1</sup>, Christoph Hugenschmidt<sup>1, 2</sup>, Stefan Gärtner<sup>3</sup>,  
Peter Thierolf<sup>3</sup>, Dirk Schwalm<sup>4</sup>

<sup>1</sup> Physik Department E21, Technische Universität München, D-85747 Garching, Germany

<sup>2</sup> Forschungsneutronenquelle Heinz Maier-Leibnitz (FRM II), Technische Universität München, D-85747 Garching, Germany

<sup>3</sup> Ludwig-Maximilians-Universität München, Am Coulombwall 1, D-85748 Garching, Germany

<sup>4</sup> Max-Planck-Institut für Kernphysik, Saupfercheckweg 1, D-69117 Heidelberg, Germany

The negative positronium ion  $\text{Ps}^-$  is a bound state consisting only of three leptons, two electrons and a positron (see fig. 1). Therefore,  $\text{Ps}^-$  is an ideal object to study the quantum mechanics of a three-body system. The ground state of  $\text{Ps}^-$  is stable against dissociation but unstable against annihilation into photons. A precise measurement of the  $\text{Ps}^-$  ground state decay rate  $\Gamma$  was carried out at the high intensity positron source NEPOMUC at the research reactor FRM II in Garching. A value of  $\Gamma = 2.0875(50) \text{ ns}^{-1}$  was obtained, which is three times more precise compared to previous experiments and in agreement with most recent theoretical predictions [1]. The experimental precision that was achieved is at the level of the leading corrections in the theoretical predictions.

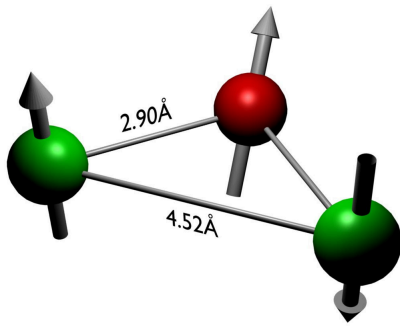


Figure 1: Artistic view of the  $\text{Ps}^-$  ion. The two electrons (green) are in a singlet state with their spins being aligned anti-parallel, while the spin orientation of the positron (red) is random. Averaged distances between the constituents are taken from [2].

## Experiment

The method applied already in the previous experiment [3] was adapted and refined. Details can be found in [4].  $\text{Ps}^-$  ions are produced transmitting positrons through a thin diamond-like carbon foil. The  $\text{Ps}^-$  ions are accelerated to an energy of several keV. The number of  $\text{Ps}^-$  ions surviving the passage through a gap of adjustable width is determined by stripping the electrons off the ions and detecting the remaining positrons. The decrease of the number of surviving  $\text{Ps}^-$  with increasing gap width is directly reflecting the decay rate  $\Gamma_{\text{Ps}^-}$ .

## Results

The present result is in very good agreement with the most recent theoretical value of  $\Gamma = 2.087963(12) \text{ ns}^{-1}$  [5], which contains now all correction terms up to order  $\mathcal{O}(\alpha^2)$ . Despite the recent progress in experimental accuracy it is obvious that due to the recent work of Puchalski *et al.* theory is again far ahead of experiment. However, with the experimental precision we achieved we are now able to probe theoretical calculations of the decay rate to the precision

of the leading order QED corrections (see fig. 2). As these terms also factor into the ortho- and parapositronium decay rates, respectively, we may use them to determine the distinct three body quantity  $\langle \delta_{+-} \rangle$  from the measured  $\text{Ps}^-$  decay rate [1]. The cusp  $\langle \delta_{+-} \rangle$  describes the probability of finding one of the electrons and the positron at the same position. This results in

$$\langle \delta_{+-} \rangle = 0.020729(50), \quad (1)$$

and has to be compared with the theoretical value of  $\langle \delta_{+-} \rangle = 0.020733\dots$  assumed to be known up to an accuracy of  $10^{-11}$  [5].

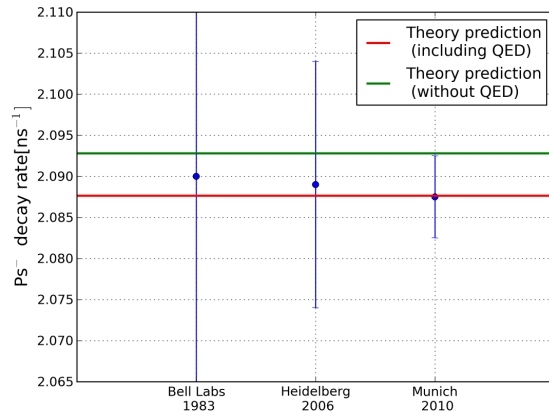


Figure 2: Calculated  $\text{Ps}^-$  decay rate with and without QED corrections according to [5] in comparison to the measured value from the present work and previous experiments [1, 3, 6]. The precision of the present result allows to experimentally probe QED correction to the decay rate for the first time.

## Outlook

Complementary to the decay rate measurement an experiment for the  $\text{Ps}^-$  photo detachment and the production of a mono energetic orthopositronium beam is in preparation and will soon be operational. It will allow for the measurement of the photo detachment cross section for different photon energies in the off-resonant region, as well as the production of a mono energetic and energy tunable orthopositronium beam with an intensity of up to a few 10 per second.

## References

- [1] Ceeh *et al.*, *Phys. Rev. A* **84** 2011 062508 (2011)
- [2] A. M. Frolov, *Phys. Rev. A* **60** 2834 (1999)
- [3] Fleischer *et al.*, *Phys. Rev. Lett.* **96** 063401 (2006)
- [4] Ceeh *et al.*, *J. Phys.: Conf. Ser.* **262** 012011 (2011)
- [5] Puchalski *et al.*, *Phys. Rev. Lett.* **99** 203401 (2007)
- [6] A. P. Mills, *Phys. Rev. Lett.* **50** 671 (1983)

# Temperature Dependent 2D-ACAR Measurements on Cr

Hubert Ceeh<sup>1</sup>, Josef Weber<sup>1</sup>, Peter Böni<sup>1</sup>, Christoph Hugenschmidt<sup>1, 2</sup>, Michael Leitner<sup>2</sup>

<sup>1</sup> Physik Department E21, Technische Universität München, D-85747 Garching, Germany

<sup>2</sup> Forschungsneutronenquelle Heinz Maier-Leibnitz (FRM II), Technische Universität München, D-85747 Garching, Germany

Recently, the Munich 2D-ACAR (Angular Correlation of Anihilation Radiation) spectrometer has become operational at the Maier-Leibnitz accelerator laboratory in Garching. The present implementation of the 2D-ACAR spectrometer has a baseline of 16.5 m and uses a conventional <sup>22</sup>Na positron source. Two Anger-type gamma-cameras are utilized for the measurement of small angular deviations from collinearity of the two 511keV annihilation quanta. This angular correlation originates from a non-zero total momentum of the e<sup>+</sup>-e<sup>-</sup>-system in the lab frame, which is almost exclusively determined by the electron momentum.

2D-ACAR measurements have been performed on Cr at 5 K and at room temperature in the anti-ferromagnetic phase and at 318 K slightly above the paramagnetic phase transition.

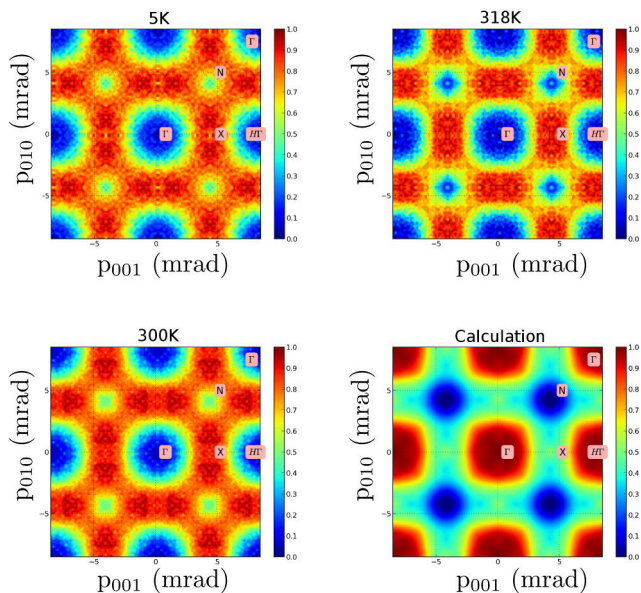


Figure 1: 2D-ACAR spectra of Cr folded back into the first Brillouin zone with the Lock-Crisp-West method [1]. Positions of high symmetry points are indicated. The spectra were obtained for different temperatures and compared to theoretical calculations.

## Experiment

The Munich 2D-ACAR spectrometer features two interchangeable sample holders, which allow to adjust the sample temperature between 5 K and 300 K with the cryogenic sample holder, and between and between 300 K and 500 K with the heatable sample holder. The details of the Munich 2D-ACAR spectrometer and the characteristics can be found in [2].

In total four 2D-ACAR measurements on Cr have been performed. For all measurements the integration direction was chosen along [100]. Two of the four 2D-ACAR measurements were performed at room temperature in order to assure that the ACAR spectra are consistent before and after

the change from the cryogenic to the heatable sample holder. Since both spectra are compatible within the statistical limits only the spectrum with the higher statistics is presented here (see figure 1).

## Results

Comparing the low temperature measurement (see figure 1, 5K) and the room temperature measurement (see figure 1, 300K) the effect of decreasing resolution with increasing temperature can be clearly observed, as the smearing of the positron momentum is temperature dependent. However, despite the lower resolution in the room temperature measurement both spectra are comparable concerning the features at the N-points, which appear to be occupied in the anti-ferromagnetic phase. The picture changes when the sample temperature is increased above the Néel temperature  $T_{N=311}$  K (see figure 1, 318K). A small difference in temperature drives the sample into the paramagnetic state and yields a drastic change in the LCW-folded data. The N-hole pockets become more pronounced and the electron pocket structure at the X-points connecting the N-points is smaller than in the anti-ferromagnetic phase. Generally, the agreement of our measurement with previous 2D-ACAR measurements (see ref.[3]) on paramagnetic Cr is considerable. However, the discrepancies between our data and the SPRKKR calculations are quite substantial (see fig. 1, lower right). This has also been reported from different laboratories [3, 4]. The relative intensities in the calculation for the occupied and the unoccupied states can not be reproduced in the LCW-folded data.

## Outlook

In Order to tackle the observed discrepancy, multiple 2D-ACAR projections of Cr in the paramagnetic and anti-ferromagnetic phase were performed in order to make a full 3D reconstruction of the electron momentum density. This way, we hope to rule out positron wave-function and enhancement effects. Respective calculations are under way.

Funding by the DFG (project no. A3 within the Transregional Collaborative Research Center TRR 80) is gratefully acknowledged.

## References

- [1] D G Lock, V H C Crisp, R N West, *J. Phys. F: Met. Phys.* **3** 561 (1973)
- [2] H Ceeh et al., arXiv:1210.3497, *submitted to Rev. Sci. Instrum.* (2012)
- [3] S B Dugdale et al., *J. Phys.: Condens. Matter* **10** 10367–10374 (1998)
- [4] M Biasini, *Physica B* **275** 285–294 (2000)

# The Electronic Structure of Cu Measured with the New 2D-ACAR Spectrometer

J. A. Weber<sup>1</sup>, H. Ceeh<sup>1</sup>, M. Leitner<sup>2</sup>, P. Böni<sup>1</sup>, Ch. Hugenschmidt<sup>1, 2</sup>

<sup>1</sup> Physik Department E21, Technische Universität München, D-85748 Garching, Germany

<sup>2</sup> Forschungsneutronenquelle Heinz Maier-Leibnitz (FRM II), Technische Universität München, D-85748 Garching, Germany

The two-dimensional measurement of the angular correlation of the positron annihilation radiation (2D-ACAR) is a powerful tool to investigate the electronic structure of materials. Recently a 2D-ACAR spectrometer has been set up at the Maier-Leibnitz-Laboratorium [1]. With this spectrometer it is possible to explore the electronic structure of correlated materials and their behavior at temperature driven phase transitions. As a proof of principle we report about the reconstruction of the Fermi surface of Cu.

When a positron is implanted into a solid, it will thermalize within a few ps and annihilate with an electron. The resulting annihilation radiation carries the momentum information of the electron-positron pair. This information is contained in a Doppler shift from the mean value of 511 keV, and the angular deviation from exact antiparallel directions of the two  $\gamma$  quanta. With 2D-ACAR the latter is measured, which yields a specific projection of the two  $\gamma$  momentum density  $\rho^{2\gamma}$ . Since the positron is at thermal energies, the angular deviation is caused mainly by the electron momentum.

The low momenta that are measured with 2D-ACAR are due to occupied states near the Fermi surface in the case of a metal. Due to the fact, that electrons in a crystal are in delocalised Bloch states  $\rho^{2\gamma}$  can be expressed as

$$\rho^{2\gamma}(\mathbf{p}) \propto \sum_{j,\mathbf{k}} \Theta(E_F - E_{j,\mathbf{k}}) \sum_{\mathbf{G}} \left| C_{\mathbf{G}}^j(\mathbf{k}) \right|^2 \delta_{\mathbf{p}-\mathbf{k},\mathbf{G}} \quad (1)$$

where the sum goes over all the states  $\mathbf{k}$  below the Fermi level in the  $j$ th band.  $C_{\mathbf{G}}^j(\mathbf{k})$  is the Fourier coefficient at the reciprocal lattice vector  $\mathbf{G}$ . From this equation we see that filled bands give a continuous distribution and bands crossing the Fermi level yield breaks which are distributed through the reciprocal space.

The method used here to calculate the full three dimensional  $\rho^{2\gamma}$  is based on the maximum entropy algorithm (MEA) [2]. Pylak et al. applied the MEA successfully for reconstructing the 3D momentum density from 2D-ACAR measurements of Gd [3]. The idea behind the MEA can be found, e.g. in [4]. The main purpose of the reconstruction is to get a three dimensional density  $D$  which agrees with the 2D-ACAR spectra  $M_i^\alpha$  (where  $i = 1 \dots N^2$  runs over all pixel) for all measured angles  $\alpha$  with the statistical error  $\sigma_i$ . In principle this task can be expressed as a minimization problem using the following equation, where  $R_i^\alpha(D)$  is the Radon transformation, i.e. the projection, of the density  $D$  at an angle of  $\alpha$ :

$$\chi^2 = \sum_{\alpha} \sum_i \frac{(R_i^\alpha(D) - M_i^\alpha)^2}{\sigma_i^2} \quad (2)$$

If  $M$  is of size  $N^2$ , then  $D$  has a size of  $N^3$ . Consequently, the minimization problem is highly under-determined. This is the reason why the MEA is needed. It is applied by using an additional criterion: The resulting density  $D$  should

be flat. For this aim, a Lagrange function with an entropy function  $\sum_j D_j \ln(D_j)$  and  $\chi^2$  is constructed by the use of the Lagrange multiplier  $\lambda$ :

$$L(D) = \sum_j D_j \ln(D_j) - \lambda \chi^2 \quad (3)$$

$L$  has to be maximized in order to obtain  $D$ . It is possible to write the solution to this problem in an iterative form [5]

$$D_i^{(n+1)} = A \frac{D_i^{(n)} \exp\left(-\lambda \frac{\partial \chi^2}{\partial D_i}\right)}{\sum_j D_j^{(n)} \exp\left(-\lambda \frac{\partial \chi^2}{\partial D_j}\right)} \quad (4)$$

with the normalization constant  $A$ .

In case of  $\rho^{2\gamma}$ , which has the symmetry of the reciprocal lattice, the quality of the reconstruction can be improved and the calculation time is reduced if the full symmetry is taken into account. Doing this, the MEA becomes a fast and accurate method to recreate the three dimensional  $\rho^{2\gamma}$ .

To calculate the three dimensional  $\rho^{2\gamma}$  a MEA was applied using five measured projections and all the equivalent directions. The data were then folded into the first Brillouin zone by the so called LCW procedure for three dimensions. A cut through  $\rho^{2\gamma}$  is plotted in figure 1, which agrees well with previous measurements and calculations.

Funding by the DFG (project no. A3 within the Transregional Collaborative Research Center TRR 80) is gratefully acknowledged.

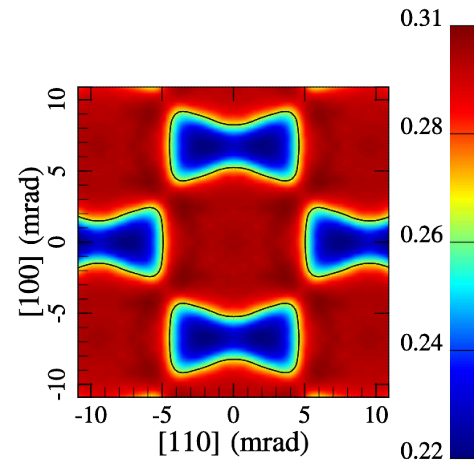


Figure 1: Cut through the Fermi surface of Copper calculated from 5 projections.

## References

- [1] H. Ceeh et al. *Rev. Sci. Instrum.*, submitted (2012).
- [2] S.F. Gull and G.J. Danielli. *Nature*, 272:686 (1978).
- [3] M. Pylak, G. Kontrym-Sznajd and L. Dobrzynski. *Appl. Phys. A Mater. Sci. Process.*, 1 (2011).
- [4] S.F. Burch, S.F. Gull, J. Skilling. *Comput. Vision Graph.*, 23:113 (1983).
- [5] J. Skilling, R.K. Bryan. *Mon. Not. R. Astron. Soc.*, 211:111 (1984).

# High-Intensity Source of Moderated Positrons Using a Brilliant $\gamma$ -Beam

Christoph Hugenschmidt<sup>1, 2</sup>, Dietrich Habs<sup>3</sup>, Peter Thierolf<sup>3</sup>, Klaus Schreckenbach<sup>1, 2</sup>

<sup>1</sup> Physik Department E21, Technische Universität München, D-85747 Garching, Germany

<sup>2</sup> Forschungsneutronenquelle Heinz Maier-Leibnitz (FRM II), Technische Universität München, D-85747 Garching, Germany

<sup>3</sup> Fakultät für Physik, Ludwig-Maximilians Universität, D-85748 Garching, Germany

## Introduction

Presently large efforts are conducted towards the development of highly brilliant  $\gamma$  beams via Compton back scattering of photons from a high-brilliance electron beam, either on the basis of a normal-conducting electron linac or a (superconducting) Energy Recovery Linac (ERL). Particularly ERL's provide an extremely brilliant electron beam, thus enabling the generation of highest-quality  $\gamma$  beams.

Until approximately 2018, it is envisaged to generate an ERL-based 2.5 MeV  $\gamma$  beam with an intensity of  $10^{15}$  photons  $s^{-1}$  with a wide range of applications [1, 2, 3]. Due to its narrow band width ( $10^{-3}$ ) and extremely low emittance ( $10^{-4}$  mm<sup>2</sup> mrad<sup>2</sup>) such a  $\gamma$ -beam facility offers the possibility to produce a high-intensity bright polarized positron beam. Pair production in a face-on irradiated W converter foil (200  $\mu$ m thick, 10 mm long) would lead to the emission of  $2 \cdot 10^{13}$  (fast) positrons per second, which is four orders of magnitude higher compared to strong radioactive <sup>22</sup>Na sources conventionally used in the laboratory. Using a stack of converter foils and subsequent positron moderation, a high-intensity low-energy beam of moderated positrons can be produced. Hence, profiting from an improved moderation efficiency, the envisaged positron intensity would exceed that of present high-intensity positron sources by a factor of 100.

## Design study

In the present study, various positron source designs and the relevant features are discussed [3]. In particular, two layouts, which provide a high-brightness or a high-intensity positron beam, are presented and quantitatively compared with the NEPOMUC beam. In the following, we present a more detailed source geometry for the creation of a high-intensity positron beam.

The layout of the high-intensity positron source shown in Figure 1. The converter-moderator, which is operated in the vacuum, consists of a stack of  $N$  W(100) foils of thickness  $d_W$ . The ratio of the foil width  $b$ , which is in the order of the diameter of the  $\gamma$  beam, and the spacing  $s$  between the foils is 3:1. The total length  $L$  is hence given by  $L \approx N(s + d_W)$  and would be of the order of 20 cm. The total setup consists of the converter-moderator block (on high potential  $V_0$ ) which is mounted between a back electrode on higher potential and an acceleration grid in order to extract the moderated positrons. (Cylindrical) electrodes are used for beam formation.

The converter-moderator block is aligned in direction of the  $\gamma$  beam which interacts with the W foils by pair production. In contrast to the primary produced fast positrons, the moderated positrons are emitted perpendicular to the W(100) surface with a primary kinetic energy of  $E_{mod}^+ = -\Phi^+ = 2.8 eV$ . Hence, the potential  $V_0$  applied at

the converter-moderator block defines the final kinetic energy of the positron beam  $E_{kin}^+ = eV_0 - \Phi^+$ . The beam should be extracted in a zero magnetic field in order to maintain the low primary divergence and the high grade of polarization of the moderated positron beam. The expected yield of moderated positrons is roughly estimated to  $Y_{mod}^+ = 3 \cdot 10^{11} s^{-1}$  [3].

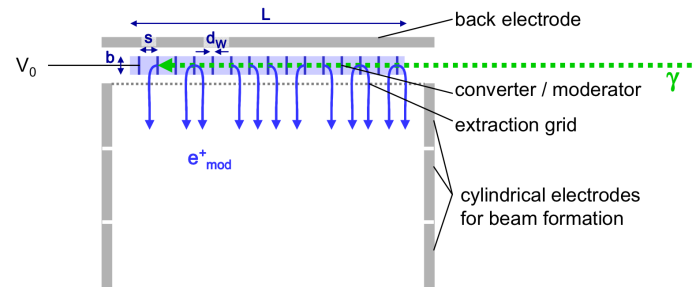


Figure 1: Scheme of a converter-moderator configuration irradiated by a brilliant  $\gamma$  beam for the generation of a high-intensity moderated positron beam.

## Features of a $\gamma$ -beam based positron source

In general, the key features of a low-energy positron beam based on high-brilliant  $\gamma$  beams would be the following: (i) The energy of the  $\gamma$  beam can be varied in the range of a several MeV in order to maximize the positron production and the yield of moderated positrons. (ii) Due to the small band width of the  $\gamma$  beam, no unwanted  $\gamma$ 's are produced with  $E < 2mc^2$  which do not contribute to the pair production. Therefore, the heat load compared to linac or reactor based positron sources is considerably lower. (iii) The intrinsic small diameter of the  $\gamma$  beam leads to an accordingly small positron beam and –dependent on the source geometry– to a higher beam brightness. (iv) Using a switchable fully polarized  $\gamma$  beam, a spin-polarized positron beam can be created. (v) The time structure provided by the pulsed  $\gamma$  beam is barely deteriorated by the moderation process. The usefulness of the initial time structure strongly depends on the positron beam application, e.g., for coincidence techniques using lasers rather than for positron lifetime spectroscopy. (vi) The easy access of the source area of the  $\gamma$  would facilitate the change of the source setup considerably. (vii) Due to the well defined relatively low energy of the  $\gamma$  beam, e.g., 2.5(5) MeV, the creation of radiation induced defects is expected to be lower than that at positron source setups using bremsstrahlung targets at linacs or  $\gamma$  rays produced at nuclear reactors. In addition, no radioactivity is created by activation.

## References

- [1] T. Hayakawa, N. Kikuzawa, R. Hajima, T. Shizuma, N. Nishimori, M. Seya M. Fujiwara, Nucl. Instrum. Methods **621**, 695 (2010).
- [2] D. Habs, M. Gross, P.G. Thierolf, P. Boni, Applied Physics B: Lasers and Optics **103**, 485 (2011).
- [3] C. Hugenschmidt, K. Schreckenbach, D. Habs, P. Thierolf, Applied Physics B: Lasers and Optics **106**, 241 (2012).

# Quantum Confinement of Positrons in Au Clusters

P. Pikart<sup>1, 2</sup>, M. Horisberger<sup>3</sup>, Y. Matsukawa<sup>4</sup>, M. Hatakeyama<sup>4</sup>, T. Toyama<sup>4</sup>,  
Y. Nagai<sup>4</sup>, C. Hugenschmidt<sup>1, 2</sup>

<sup>1</sup>Physik-Department E21, Technische Universität München, D-85748 Garching, Germany.

<sup>2</sup>Forschungsneutronenquelle Heinz Maier-Leibnitz (FRM II), Technische Universität München, D-85748 Garching, Germany.

<sup>3</sup>PSI, Laboratory for Developments and Methods, CH-5232 Villigen PSI, Switzerland.

<sup>4</sup>IMR, Tohoku University, 2145-2 Oarai, Ibaraki, Japan.

## Introduction

Open-volume lattice defects and their chemical surrounding can be studied non-destructively by coincident Doppler broadening spectroscopy (CDBS) of the positron annihilation line. Not only vacancy-like defects but also agglomerations of atoms with a higher relative positron affinity  $\Delta A^+ < 0$  might form a trapping potential for positrons [1]. Due to its elemental selectivity CDBS is particularly suited to detect small metallic clusters or precipitates embedded in a matrix. In addition, the application of a monoenergetic positron beam allows one to adjust the positron implantation depth which leads to a greatly enhanced sensitivity in a selected depth.

## Experimental

In the present study, defect-sensitive and element-selective measurements on ultra-thin Cr, Cu, and Au layers embedded in Al were performed by CDBS with the monoenergetic positron beam at NEPOMUC [2]. The specimens, which were grown by magnetron sputtering out of high-purity materials, consist of an Al substrate, an intermediate layer of Cr, Cu or Au, and a cover layer of 200 nm Al. Among these elements Au has the highest positron affinity, i.e.  $\Delta A^+ = -1.82$  eV with respect to Al.

The obtained CDB spectra of Au layers with a nominal thickness of 0.5, 2 and 100 nm embedded in Al and reference spectra of pure Au and Al are shown in Figure 1. A clear Au signature at the 100 nm layer was recorded which remained almost the same even at a nominal thickness of only 2 nm Au embedded in Al. The sample with an embedded Au layer of only 0.5 nm showed no Au signature at all.

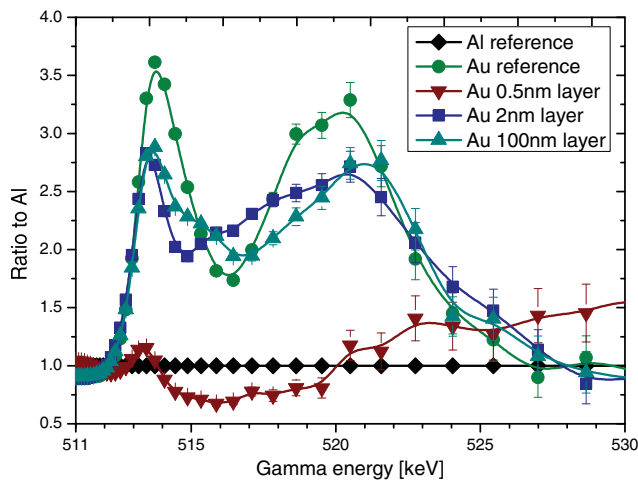


Figure 1: CDB spectra of Au layers with different nominal thickness embedded in Al and reference spectra of pure Au and Al. The Au signature is clearly visible at a Au layer of only 2 nm embedded in Al.

Complementary TEM studies were performed in order to image the buried layers as exemplified in Figure 2.

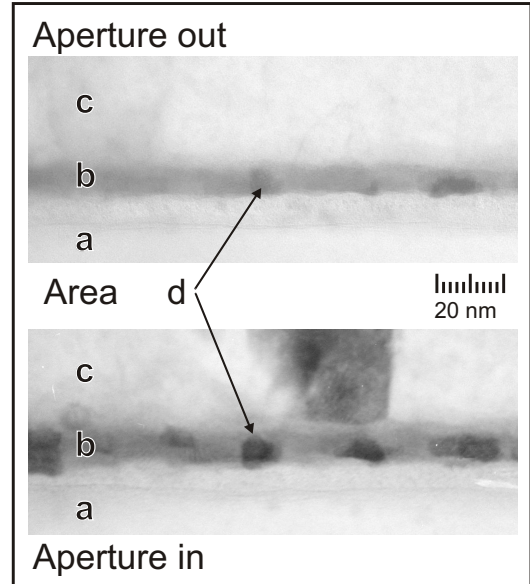


Figure 2: TEM image of the Au rich layer (b) embedded in Al (a, c). The bright-field image (aperture in) reveals the grains and grain boundaries of the Au clusters (d).

## Positron trapping in Au clusters

The extremely high sensitivity, which was already achieved for the 2 nm Au layer, is attributed to the highly efficient positron trapping in the Au layer and Au clusters. Exceeding a critical size, Au clusters in Al form a three dimensional quantum well that confines the positron wave function. The critical radius  $r_c$  for positron trapping was calculated based on the positron affinity difference  $\Delta A^+$  and amounts to  $r_c = 0.23$  nm. Consequently, Au clusters containing at least 14 Au atoms lead to efficient positron trapping. For the same reason, no positron trapping sites are formed by Au at the sample with a nominal thickness of 0.5 nm Au where no Au signature was observed.

The positron behaviour was theoretically described in two steps: First, the positron implantation profile was calculated using the Makhov-approximation. In a second step, a random walk model was implemented to describe the positron diffusion and the trapping in buried layers. The comparison of the experimental results with Monte Carlo simulations of the positron diffusion indicated a strong positron trapping in the AlAu alloy layer in Al. Finally, the theoretically calculated positron affinity was proved to be a profound basis for the understanding of a quantum confinement based model of the positron trapping in Au clusters with a minimum diameter of 0.46 nm surrounded by Al.

## References

- [1] C. Hugenschmidt et al., Physical Review B **77**, 092105 (2008).
- [2] P. Pikart et al., Physical Review B **84**, 014106 (2011).

# Thin Film Alloying Studied by CDBS with the NEPOMUC Positron Beam

Markus Reiner<sup>1, 2</sup>, Philip Pikart<sup>1, 2</sup>, Christoph Hugenschmidt<sup>1, 2</sup>

<sup>1</sup>Physik-Department E21, Technische Universität München, D-85748 Garching, Germany.

<sup>2</sup>Forschungszentrum Heinz Maier-Leibnitz (FRM II), Technische Universität München, D-85748 Garching, Germany.

Coincident Doppler Broadening Spectroscopy (CDBS) enables the detection of high momenta of strongly bound core electrons and hence, reveals the chemical environment of the positron annihilation site on an atomic scale. Using the high-intensity NEPOMUC positron beam at the FRM II enables CDBS as function of both implantation depth and temperature. This unique experimental technique offers a great potential for the investigation of the structure and kinematics in multilayer systems such as annealing, interdiffusion and thin film alloying. The element selectivity of these studies can be further increased by the ab-initio calculation of CDB spectra.

## Ab-initio calculation of CDB spectra

For the calculation of CDB spectra, the momentum distribution  $\rho(\mathbf{p})$  of the annihilating electron-positron-pair

$$\rho(\mathbf{p}) = \pi r_0^2 c \sum_j u_j^2(0) \left| \int d\mathbf{r} e^{-i\mathbf{p}\cdot\mathbf{r}} \psi_+(\mathbf{r}) \psi_j(\mathbf{r}) \right|^2 \quad (1)$$

is determined within a two-component density functional theory [1]. In the limit of a vanishing positron density,  $\psi_+$  is obtained by solving the positron's Schrödinger equation in the bulk. Its charge density is described by an atomic superposition method of electronic wavefunctions  $\psi_j$ . Electron-positron correlations are described by the state-dependent enhancement factor  $u_j(0)$  and modeled by a generalized gradient approximation. The measured momentum distribution  $\rho(\mathbf{p})$  is given as sum of all orbital momentum distributions;  $r_0$  denotes the classical electron radius.

The presented calculational method accounts for the annihilation with (semi-)core electrons. Hence, the calculated well describe the element-specific signature in the High Momentum Area (HMA) of CDB spectra.

## Au/Cu interdiffusion

The vast range of applications of thin film systems and their continuous downscaling demand a detailed understanding of microscopic processes. For this, positrons with their high defect sensitivity reveal not only unique information about defect-related processes like annealing [2], but also about structural changes by the use of depth-dependent and in-situ CDBS at elevated temperature. Hence, this experimental technique, which requires a high-intensity positron beam, is an outstanding tool for the investigation of thin film annealing and alloying at the interface on the same time.

In a comprehensive study, the tempering of a vapor deposited bilayer Au (180 nm)/Cu (480 nm) on a Si substrate was investigated by depth-dependent and in-situ CDBS for the first time [3]. In both layers, the grain size was determined to be  $30 \pm 10$  nm by XRD-spectroscopy. During tempering, in-situ CDBS with an positron implantation energy of 9 keV (which corresponds to implantation of positrons on the topmost Au layer close to the Au/Cu interface) was performed at three different temperatures: 633 K, 683 K and 733 K.

During tempering at 633 K, the following two stages were identified: In the first three hours, mainly annealing was detected and the initial grain boundary diffusion of Cu atoms into the Au film only slightly affected the measured spectra. In the following four hours, the spectra slowly approached that taken at 683 K and 733 K, where the sample was found to be in thermal equilibrium. The latter both measured spectra were compared with theoretical calculations.

The CDB spectra for the disordered fcc phase of (Au,Cu) with a varying Au content between 20 % and 90 % were calculated (figure 1). At both temperatures, excellent agreement was found for an Au content of 70 %. Hence, it can be concluded that during the second tempering stage observed at 633 K a homogenization of Au and Cu atoms took place leading to the formation of  $\text{Au}_{0.7}\text{Cu}_{0.3}$ .

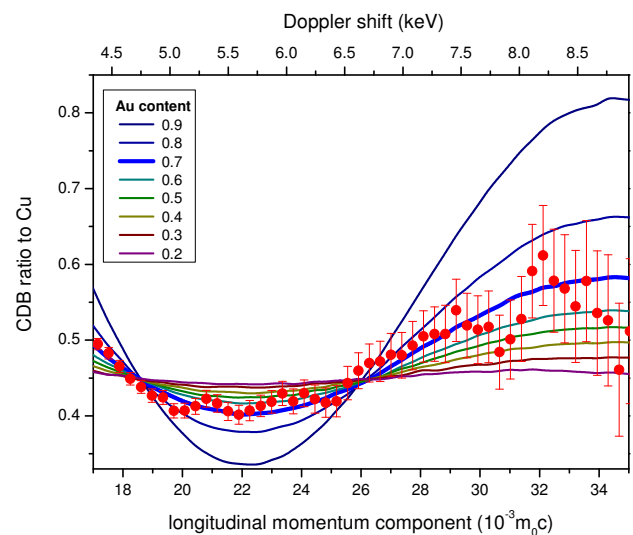


Figure 1: HMA of the CDB ratio curve at 733 K at the Au/Cu interface. Calculational results display an Au content of around 70 %.

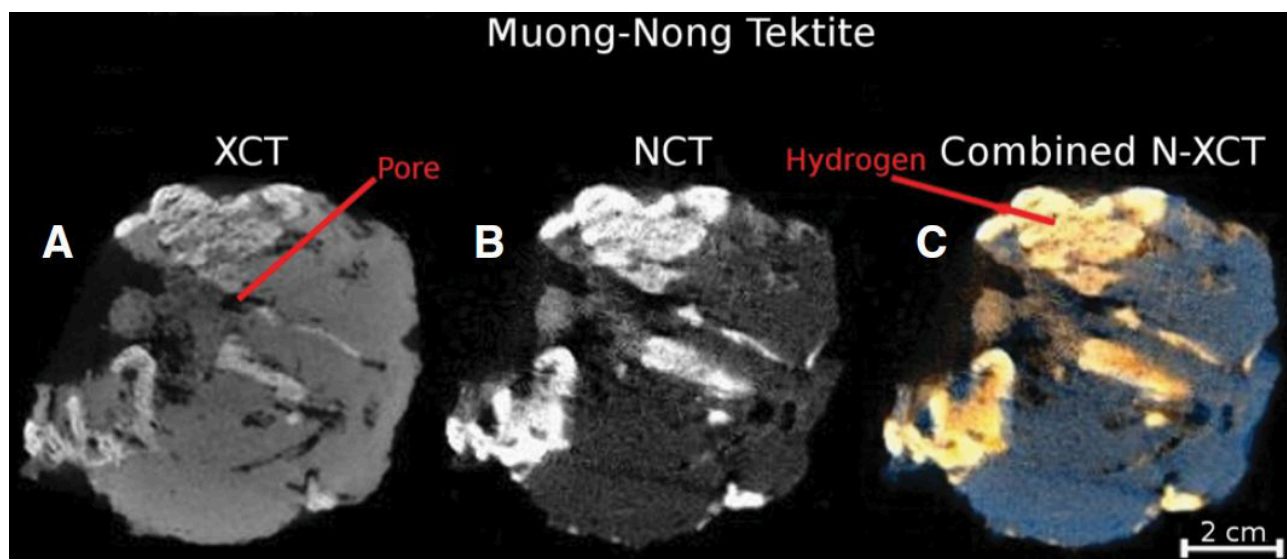
Depth-dependent CDBS before and after tempering confirmed that the topmost Au layer was replaced by a homogeneous intermixing zone of  $\text{Au}_{0.7}\text{Cu}_{0.3}$ . Below this intermixing zone, a high amount of Cu was detected as well. Hence, both layers did not totally mix up. Furthermore, the kinematics of the observed process indicate that the initial movement of Cu atoms along grain boundaries accelerated the intermixing [3].

## References

- [1] M. J. Puska and R. M. Nieminen, Rev. Mod. Phys. **66**, 841 (1994).
- [2] M. Reiner, P. Pikart, and C. Hugenschmidt, Phys. Procedia **35**, 104 (2012).
- [3] M. Reiner, P. Pikart, and C. Hugenschmidt, to be published.

# Chapter 4

# Radiography and Tomography



X-Ray and Neutron CT of Tektite  
(by K.-U. Hess, see page 38)





# Neutron Depolarisation Imaging: Stress Measurements by Magnetostriction Effects in Ni Foils

Michael Schulz<sup>1, 2</sup>, Philipp Schmakat<sup>1, 2</sup>, Christian Franz<sup>1</sup>, Andreas Neubauer<sup>1</sup>,  
Elbio Calzada<sup>1, 2</sup>, Burkhard Schillinger<sup>1, 2</sup>, Peter Böni<sup>1</sup>, Christian Pfeleiderer<sup>1</sup>

<sup>1</sup>Physik-Department E21, Technische Universität München, D-85748 Garching, Germany.

<sup>2</sup>Forschungsneutronenquelle Heinz Maier-Leibnitz (FRM II), Technische Universität München, D-85748 Garching, Germany.

## Introduction

Imaging with polarized neutrons [1, 2], is a new method which is increasingly being recognized as a powerful tool for the study of magnetic effects. Here we present first proof-of-principle measurements of a new application of neutron depolarization imaging. The magnetostriction effect leads to a change of the orientation of the domains within a ferromagnetic sample, if a uniaxial force is applied on the sample. As a consequence, a change of the depolarization which a neutron beam suffers after transmission of the sample is observed. In our experiments we used this effect on high purity Ni foils with a magnetostrictive constant of  $\lambda_s \approx -37 \cdot 10^{-6}$  [3] as a method for the spatially resolved measurement of the mechanical stress in the material. In the future this technique might be used as a spatially resolved stress gauge.

## Experiments

Our experiments were performed at the imaging beam line ANTARES at FRM II, Munich with a one dimensional polarization analysis setup shown in Fig. 1. The setup consists of a collimator (C), from which the neutron beam emerges and is monochromatized by a double crystal graphite monochromator (M) to a wavelength of 3.2. After the monochromator the neutrons travel along an evacuated flight tube (FP) of approximately 12 m length to the sample area, where a <sup>3</sup>He polarizer (P), a precession coil type spin flipper (F) and an analyzer (A) were installed before and after the sample (S), behind which the detector (D) is located.

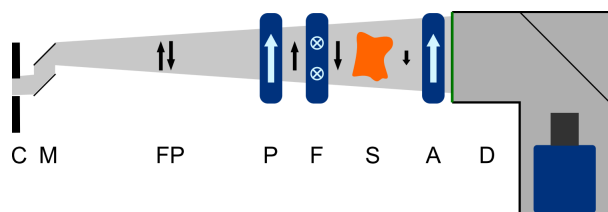


Figure 1: Experimental setup consisting of a collimator (C), double crystal monochromator (M), flight path (FP), polarizer (P), spin flipper (F), sample (S), polarization analyzer (A) and a CCD detector (D).

High purity Ni foils (99+%) with a thickness of 127  $\mu\text{m}$  were cut to a concave shape as shown in Fig. 2 (left hand side) with a maximal width of 30 mm and a minimal width of 10 mm. After cutting, the foils were annealed in vacuum at 900 °C for 8 h to remove any remaining strain from the samples and then mounted in a frame, which was fixed at the top end, while the bottom end could be loaded with weights up to 25 kg resulting in a maximum stress of  $\sigma \approx 200$  MPa.

## Results and Discussion

In Fig. 2, the beam polarization of the neutron beam after transmission of the sample at the position where it has its smallest width (marked by the dashed green lines in the left panel) is plotted vs. the load. It is clearly visible that the polarization increases with increasing stress, which is due to the preferred alignment of the domains in the sample parallel to the direction of the applied mechanical stress and thus also parallel to the polarization of the beam. A quantitative, spatially resolved evaluation of the mechanical stress in the foil from the presented experiment was not possible due to the large errors in the measurements. These errors could, however, be decreased in the future by increasing the counting statistics.

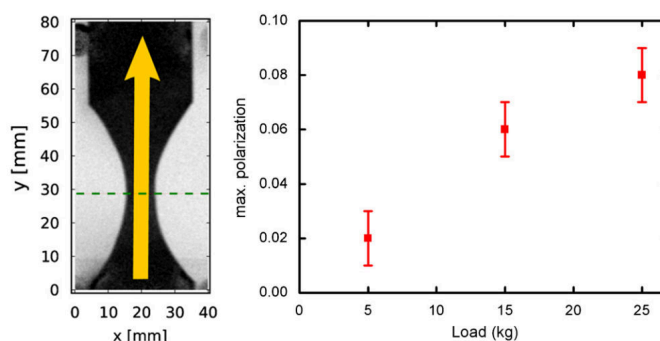


Figure 2: Radiograph of the sample (left), beam polarization after transmission of the sample (right).

## Conclusion and Outlook

These proof-of-principle measurements have shown the possibility to use ferromagnetic foils with a large magnetostrictive constant as stress gauges for the spatially resolved determination of mechanical stress. The sensitivity of the method could be further improved by using foils with a larger magnetostrictive constant, e.g. FeCoV ( $\lambda_s \approx 83.4 \cdot 10^{-6}$  [4]), improving the counting statistics by using a polychromatic beam and by performing 3D polarization analysis.

## References

- [1] N. Kardjilov et al., Nature Physics **4**, 399 (2008).
- [2] M. Schulz, PhD thesis, Technische Universität München, <http://nbn-resolving.de/urn/resolver.pl?urn:nbn:de:bvb:91-diss-20100824-963430-1-2> (2012).
- [3] G. Matsumoto et al., Journal of the Physical Society of Japan **21**, 882 (1966).
- [4] M. Senthil Kumar and P. Böni, Journal of Applied Physics **91**, 3750 (2002).

## Application of Neutron Radiography to Study Material Processes During Hypothetical Severe Accidents in Nuclear Reactors

Mirco Große<sup>1</sup>, Martin Steinbrück<sup>1</sup>, Juri Stuckert<sup>1</sup>, Anders Kaestner<sup>2</sup>,  
Burkhard Schillinger<sup>3,4</sup>

<sup>1</sup> Karlsruhe Institute of Technology, Institute for Applied Materials, P.O. Box 3640, 76021 Karlsruhe, Germany.

<sup>2</sup> Department of Spallation Source, Paul Scherrer Institute, 5232 Villigen, Switzerland.

<sup>3</sup> Physik-Department E21, Technische Universität München, D-85748 Garching, Germany.

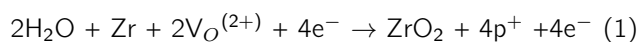
<sup>4</sup> Forschungsneutronenquelle Heinz Maier-Leibnitz (FRM II), Technische Universität München, D-85748 Garching, Germany.

Neutron radiography was applied for investigations of nuclear fuel cladding and control rod behaviour during steam oxidation at temperatures between 1123 and 1673 K under severe nuclear accident conditions. Radiography experiments were performed at ICON (PSI) and ANTARES (FRM II). At KIT, loss of coolant and severe nuclear accidents were experimentally simulated. Post-test examinations of damaged control rods were performed.

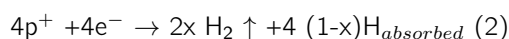
The uptake of hydrogen during steam oxidation and its diffusion in Zircaloy-4 was investigated in ex situ and in situ radiography experiments at temperatures of 1123 to 1673 K. The kinetics of hydrogen uptake and diffusion was determined. The oxide layer morphology strongly influences the hydrogen concentration in steam oxidized zirconium alloys. Differences of nearly one order of magnitude were found in samples withdrawn from large scale QUENCH experiments. The hydrogen diffusion coefficients were determined for various temperatures. Whereas the diffusion coefficients at 1123 and 1173 K agree well with values expected from literature values for pure Zr, at higher temperatures a faster diffusion was found. The determined activation energy of the hydrogen diffusion is about 10 % higher than published values in the literature.

### Steam oxidation

The most important accident management measure to terminate a severe accident transient in a Light Water Reactor (LWR) is the injection of water to cool down the uncovered degraded core. The combination of hot fuel rods and steam results in a strong exothermic oxidation reaction of the zirconium cladding alloys, connected with a sharp increase in temperature, hydrogen production and fission product release. Free protons are produced in the steam oxidation reaction with oxygen vacancies  $V_O^{(2+)}$ .



They can recombine to H<sub>2</sub> gas which is released to the surrounding atmosphere. Otherwise they can diffuse through the growing oxide layer and be absorbed by the  $\beta$ -Zr phase.



Whereas the released hydrogen results in the risk of a hydrogen detonation in the reactor environment, the hydrogen absorption by the metal shifts the time scale of the hydrogen release and reduces the toughness of the material. The so reduced thermo-shock stability of the cladding can result in a complete collapsing of the rods and a massive release of the fuel into the reactor vessel.

### In situ investigations

The in situ investigations of the hydrogen uptake during steam oxidation of zirconium alloys provide for the first time information about the process which could not be obtained before by other methods including ex situ neutron radiography investigations. Figure 1 gives a typical example for the kinetics of hydrogen uptake and release (ZIRLO<sup>TM</sup>, 1100°C, flowing atmosphere with 30 l/h Ar, 30 g/h steam). Surprisingly, a very rapid hydrogen uptake takes place initially. During the first 10 s - the illumination time of one picture - most of the hydrogen is absorbed. It seems that this uptake occurs as long as a metallic surface is available. From the oxidation kinetics, the whole amount of free protons produced by the reaction given in Eq. 1 can be estimated. An analysis of it shows that about 3/4 of the produced hydrogen is absorbed during the first 10 s of the steam oxidation, whereas only 1/4 is released. Later, when the specimen is covered by an oxide layer, no additional hydrogen uptake takes place. The reduction of the hydrogen concentration can be explained by two effects: on one hand, by the reduction of the hydrogen partial pressure in the gas atmosphere due to the parabolic oxidation kinetics and, on the other hand, by the consumption of the  $\beta$ -Zr phase which can dissolve a much higher amount of hydrogen than the  $\alpha$ -phase or the oxide.

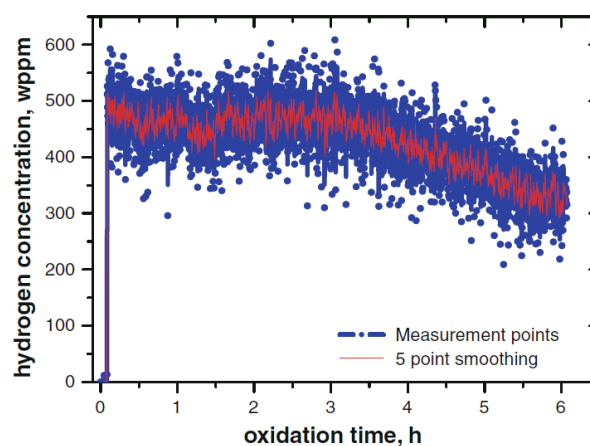


Figure 1: Dependence of the hydrogen concentration in the sample on the oxidation time for ZIRLO<sup>TM</sup> at 1100°C (flowing gas atmosphere with 30 l/h Ar, 30 g/h steam).

### References

- [1] M. Große, M. Steinbrück, J. Stuckert, A. Kaestner, B. Schillinger, Journal of Materials Science, September 2012, Volume 47, Issue 18, pp 6505-6512.

## Advances in High-Resolution Neutron Computed Tomography

K.-U. Hess<sup>1</sup>, A. Flaws<sup>1</sup>, M.J. Mühlbauer<sup>2,3</sup>, B.Schillinger<sup>2,3</sup>, A. Franz<sup>4</sup>, M. Schulz<sup>2,3</sup>, E.Calzada<sup>3</sup>, D.B. Dingwell<sup>1</sup>, K. Bente<sup>4</sup>

<sup>1</sup> Geo- und Umweltwissenschaften, Ludwig-Maximilians-Universität, 80333 München

<sup>2</sup> Physik-Department E21, Technische Universität München, D-85748 Garching

<sup>3</sup> Forschungsneutronenquelle Heinz Maier-Leibnitz (FRM II), Technische Universität München, D-85748 Garching

<sup>4</sup> Institut für Mineralogie, Kristallographie und Materialwissenschaften, Universität Leipzig, 04275 Leipzig

New scintillation screens employed at the ANTARES neutron imaging facility (FRM-II, Munich, Germany) have led to significant improvements in spatial resolution and contrast for geomaterial imaging. Resolutions of  $\sim 16 - 100 \mu\text{m}$  are now possible, a level now comparable with X-ray computed tomography (XCT). Many applications are expected in geomaterial research, including the formation of natural glasses, the characterization of limited and/or precious samples such as scientific drill cores, and bio mineralization studies. The application of state-of-the-art scintillator screens now allows us to achieve spatial resolutions as low as  $16 \mu\text{m}$ .

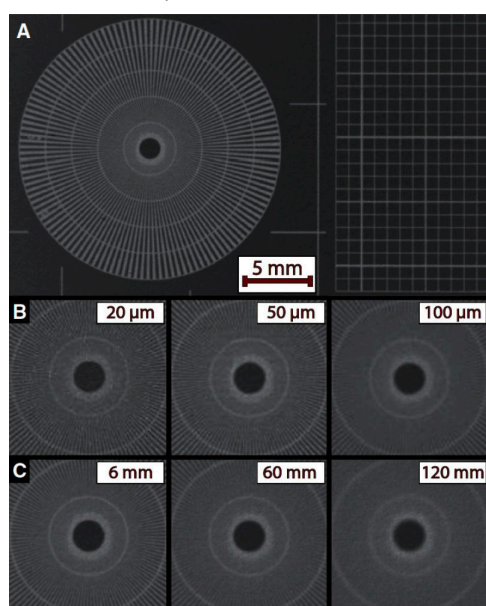


Figure 1: (A) Siemens star test pattern (B) Center of the Siemens star for scintillators of different thicknesses. (C) The same region imaged by a scintillator of  $50 \mu\text{m}$  thickness with increasing distance to the scintillator.

### Scintillation screens

For high-resolution imaging, a highly collimated beam is required. Parallel beam geometry is approximated by a small-diaphragm collimator and a long flight tube. The image resolution is thus limited by the detector, since there is no inherent image magnification. Neutrons are detected in a ZnS + LiF screen by  ${}^6\text{Li}(n,\alpha){}^3\text{H} + 4.7\text{MeV}$  or in a Gadox Screen ( $\text{Gd}_2\text{O}_2\text{S}$ ) by  $\text{Gd}(n,e^-)\text{Gd} + 187 \text{keV} + \gamma$ . The stopping path length of the reaction products limits the achievable resolution. In a standard  $100 \mu\text{m}$  LiF+ZnS screen, the reaction products have a range of  $50\text{-}80 \mu\text{m}$ .  $\text{Gd}_2\text{O}_2\text{S}$  screens can be fabricated down to  $5\text{-}20 \mu\text{m}$  thickness; they produce less blurring, but also lower light output. A Siemens star and a square grid test pattern were imaged (Fig. 1A). Radiographs were produced for different scintillator thicknesses (Fig. 1B), exposure times, and beamline configurations. Geometrical blurring was tested by increasing the distance between the test pattern and the scintillator screen (Fig. 1C). The resolution was measured as full width at half ma-

ximum (FWHM) of the lines on the right of the test pattern in Fig. 1A and compared to the true line width.

### Results

The size of the blur spot is a combination of: (1) geometrical spreading, depending on distance to the scintillator screen,  $d$ ; (2) stopping length of the reaction products and (3) a cutoff at the CCD camera pixel size. The thick black line in Figure 2A shows the total, Figure 2B the measured resolution for each scintillator ( $100, 50, 20, 10 \mu\text{m}$  thickness). The  $10 \mu\text{m}$  scintillator resolution was limited by the  $16 \mu\text{m}$  CCD pixel size cutoff for these experiments.  $L/D$  - ratio of beam flight length  $L$  to pinhole diameter  $D$ .

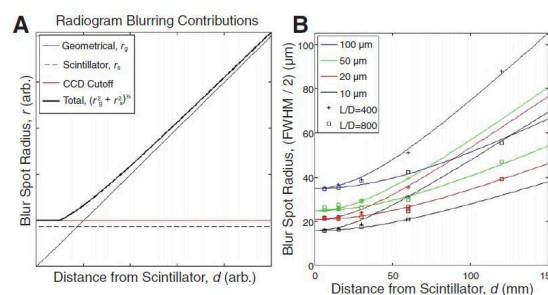


Figure 2: Spot blurring.

### Example in geo sciences: Myong-Nong type Tektite

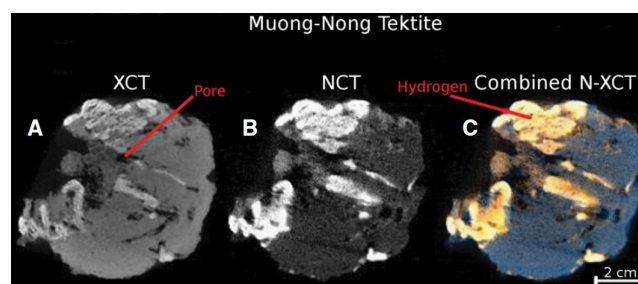


Figure 3: X-ray and Neutron CT of Myong-Nong type Tektite.

Tektites are natural glasses formed during meteorite impacts. Figure 3 is a comparison between NCT (3A) and XCT (3B) imaging for a Muong-Nong tektite. Fig. 3C is a false-color combination of the two data sets, with the neutron data in the red channel and the X-ray data in the blue. Both data sets share the green channel. Where the two data sets agree on the relative attenuation, the combined region will be shaded gray; if neutron or X-ray attenuation dominates, the region will be tinged orange or blue, respectively. We can distinguish between the unaltered glass matrix (blue), deformed pores (black), and hydrogen-bearing material (orange).

### References

- [1] K.-U. Hess, A. Flaws, M.J. Mühlbauer, B.Schillinger, A. Franz, M. Schulz, E.Calzada, D.B. Dingwell, K. Bente, *Geosphere*, First published online November 22, 2011, doi: 10.1130/GES00566.1, v. 7 no. 6 p. 1294-1302.

# Laboratory Simulations of Tensile Fracture Development in a Volcanic Conduit via Cyclic Magma Pressurisation

P. M. Benson<sup>4, 5</sup>, M. J. Heap<sup>6</sup>, Yan Lavallée<sup>1</sup>, A. Flaws<sup>1</sup>, K.-U. Hess<sup>1</sup>,  
A.P.S. Selvadurai<sup>7</sup>, D.B. Dingwell<sup>1</sup>, B. Schillinger<sup>2, 3</sup>

<sup>1</sup> Geo- und Umweltwissenschaften, Ludwig-Maximilians-Universität, 80333 München

<sup>2</sup> Physik-Department E21, Technische Universität München, D-85748 Garching

<sup>3</sup> Forschungsneutronenquelle Heinz Maier-Leibnitz (FRM II), Technische Universität München, D-85748 Garching

<sup>4</sup> Geological Institute, Department of Earth Sciences, Swiss Federal Institute of Technology, CH-8092 Zürich

<sup>5</sup> Rock Mechanics Laboratory, School of Earth and Environment, University of Portsmouth, UK

<sup>6</sup> Ecole et Observatoire des Sciences de la Terre, Université de Strasbourg, France

<sup>7</sup> Department of Civil Engineering and Applied Mechanics, McGill University, Montreal, Quebec, Canada

During volcanic unrest, high magma pressure induces cracking and faulting of the country rock, providing conduits for the transport of magma and other fluids. These conduits, known as dykes, are fundamental structures for the transport of magma to the surface in volcanically active regions. The mechanics of dyke propagation is not yet fully understood but is crucial to better model dyke emplacement and eruption in volcanoes. Central to this need is a greater understanding of the mechanical properties of the magma/country rock interaction as a function of known magmatic pressure, temperature and stress. Here, we report data from a series of experiments in which we cyclically compress viscoelastic rhyolitic magma (at 828°C, 892°C and 918°C) inside a cylindrical conduit-like shell of basalt (from Mt. Etna, Italy) until fracture occurs. The compression is performed under strain rates cyclically varying between  $5 \times 10^6$  and  $5 \times 10^5 \text{ s}^{-1}$ . The resultant monitored (axial) loading and relaxation illustrates how the presence of a visco-elastic fluid (magma) controls the stress induced at the conduit margin boundary. This is achieved by analysing the viscoelastic relaxation (through time) to calculate an apparent modulus, which is found to decrease with both increasing temperature and time. In the 4 cycles before failure we find that the apparent modulus decreases from 180 to 40 GPa, 80 to 20 GPa and 8 to 1 GPa for imposed stress cycles at 828°C, 892°C and 918°C, respectively. We theoretically estimate a tensile strength at failure of approximately 7-11 MPa, consistent with recent field data and in agreement with a model derived from the sample geometry and basic material parameters. Post-experimental neutron computed tomography and microscopic analyses further reveal the fragmentation of the melt and generation of tuffisite veins inside the conduit due to spontaneous crack nucleation associated with conduit wall fracture. The geometry of the rupture area inside the melt is akin to a Mach cone associated with supershear fractures.

## Experimental setup and results

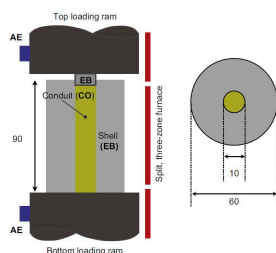


Figure 1: Experimental setup of the press and oven.

Figure 1 shows the experimental setup in side view (left) and plan view (right). The composite sample of Cougar Creek Obsidian (CO) is encased by a shell of basalt (EB) and

topped by a hard basaltic plug. Compression of the plug, and thus the rhyolitic melt, was achieved using a servo-controlled hydraulic apparatus, within a 3 zone split furnace.

Figure 2 shows the plan view images of the fractured outer shell with radial cracks in samples YE1 (828 °C), YE4 (892 °C), YE2 (918 °C) and YE3 (890 °C). The sketches below highlight the tensile cracks. At high strain rates, samples occasionally fracture in a violent manner (sample YE3, 890 °C), see [1] for details. Sample diameter is 60 mm.

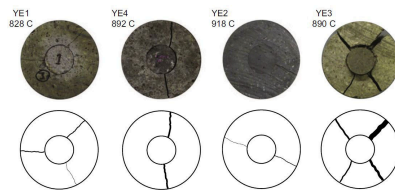


Figure 2: Images of the fractured outer shell with radial cracks.

Figure 2 shows the sketch of the fractures along with neutron computed tomographic images and transmitted light microphotograph of sample YE2 at 918 °C. Neutron computed tomographic images reveal the continuous nature of the radial cracks along the conduit length. Detailed microscopic examination further highlights the fracturing of the inner core of rhyolitic melt. In transmitted light, we observed converging cracks and propagation direction (arrows) akin to a 'Mach cone' fossilised in the melt due to the catastrophic failure of the outer shell. Such 'shock cone' features generally form when fractures propagate faster than the local speed of sound, preserved in the (formerly molten) rhyolite at an angle  $\gamma$  to the fracture.

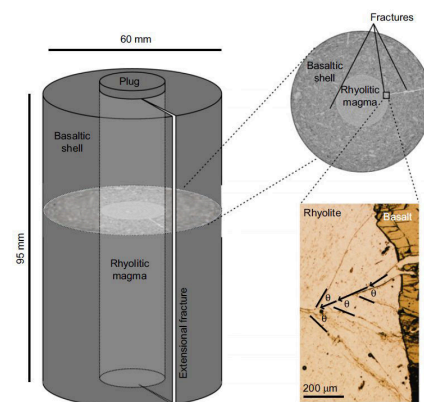


Figure 3: Sketch of the fractures along with neutron computed tomographic image and transmitted light microphotograph.

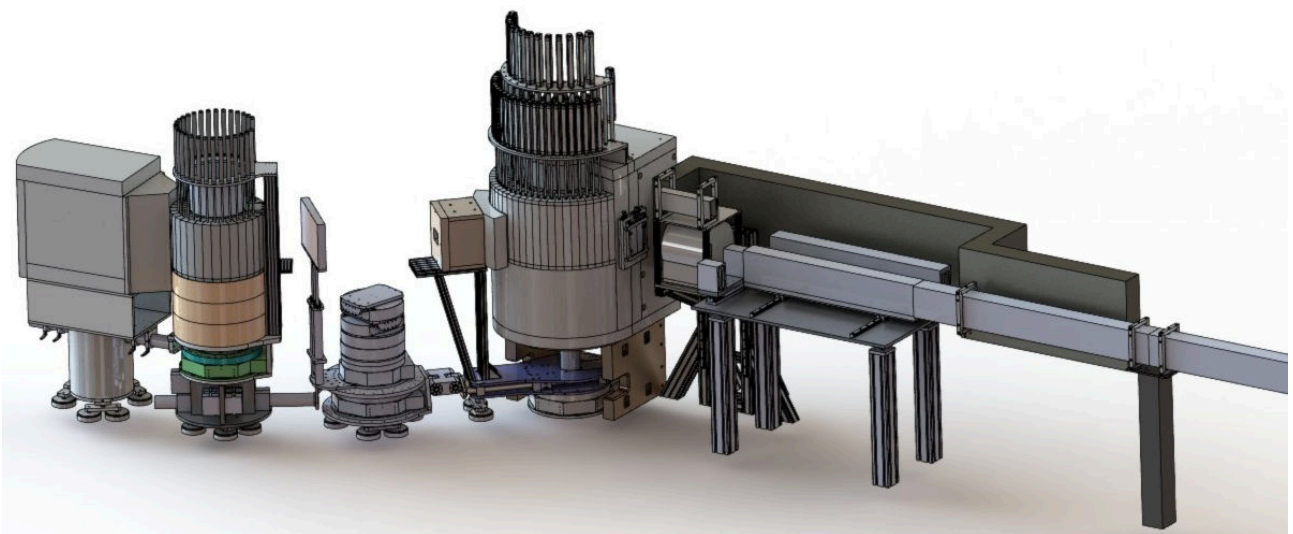
## References

- [1] P. M. Benson, M. J. Heap, Yan Lavallée, A. Flaws, K.-U. Hess, A.P.S. Selvadurai, D.B. Dingwell, B. Schillinger, *Earth and Planetary Science Letters* 349-350 (2012) 231-239.



## Chapter 5

# Instrument Development



**KOMPASS**

(by Alexander Grünwald, see page 45)



## Triple-Axis Option of MIRA

Robert Georgii<sup>2, 1</sup>, Georg Brandl<sup>2, 1</sup>, Peter Böni<sup>1</sup>, Reinhard Schwikowski<sup>2, 1</sup>

<sup>1</sup> Physik Department E21, Technische Universität München, D-85747 Garching, Germany

<sup>2</sup> Forschungsneutronenquelle Heinz Maier-Leibnitz (FRM II), Technische Universität München, D-85747 Garching, Germany

MIRA has been recently upgraded for triple axis measurements with cold neutrons. This opens the possibility to study the dynamics of large scale structures with excellent  $q$  resolution. Main emphasis was put on the use of small samples, for instance in pressure cells. Therefore the existing elliptical focussing guides were included in this development. Furthermore, an Eulerian cradle can be operated in triple-axis mode, which makes inelastic measurements in arbitrary scattering planes possible.

In figure 1 the set-up on MIRA-2 for the first test measurements is shown. As MIRA-2 shares the neutron guide NL6a with two downstream instruments, it is impossible to mount a collimator in front of the monochromator. Thus, the first collimator is  $\alpha_2$  after the monochromator inside the monochromator shielding. The sample environment on the sample table can be supplied from the top, thus facilitating measurements at larger take-off angles. The energy analyser consists of 12 HOPG crystals of the size of  $20 \times 40 \text{ mm}^2$  with a mosaicity of  $0.8^\circ$ , similar to that of monochromator crystals. The detector is a  $^3\text{He}$  tube shielded by 30 cm of boron-enriched polyethylene. So far, we only worked with a preliminary shielding in order to find the optimum shielding configuration. A new detector shielding based on this experience is currently developed and will be ready by early 2013.

The whole spectrometer was precisely aligned according to the Brookhaven method [1], and the instrumental resolution function was determined using a vanadium sample. Wavelength calibration was done using the same standards as the other triple axis instruments at the FRM II. Finally, this setup allows for inelastic neutron scattering measurements in constant  $k_i$  mode up to several meV in energy with an excellent  $q$  resolution.

The instrument control software was adopted from the existing triple axis machines PANDA and PUMA and is now consistent between all three instruments. This makes it easy for users to switch between several instruments at the FRM II. Additional software visualising the accessible reciprocal space and plotting the instrument resolution function at different instrument setups for better measurement planning has also been developed and can be used parallel to the instrument control software.

A first test, and simultaneously benchmark, of the MIRA triple axis option was performed with a  $1 \text{ cm}^3$  lead sample. The same sample is used as a calibration standard at PANDA. The result is shown in Figure 2 and demonstrates the excellent performance of the triple axis option of MIRA. The intensity without collimation and vertical monochromator focussing is roughly a factor of three smaller than that available on PANDA at a similar  $k_i$ , but full monochromator focussing and analyser focussing. Using the focusing

guides on a small sample will still improve the peak to background ratio, therefore allowing for inelastic measurements with high intensity in pressure cells or on small sample.

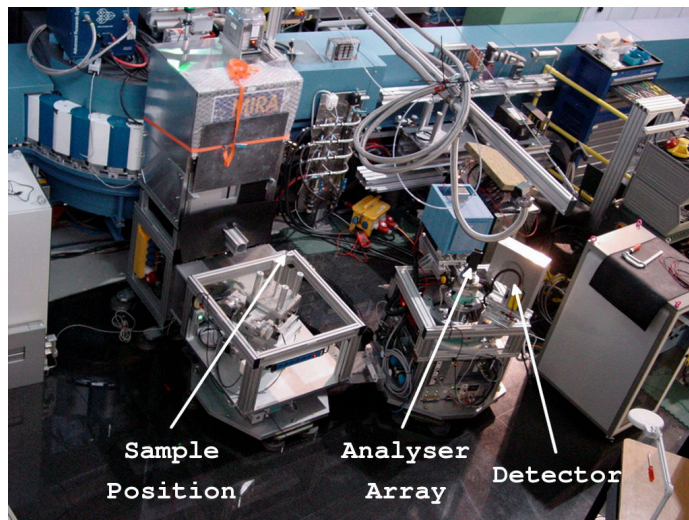


Figure 1: First measurement with the MIRA triple axis mode, still using a preliminary detector shielding. The second collimator behind the sample has not yet been mounted.

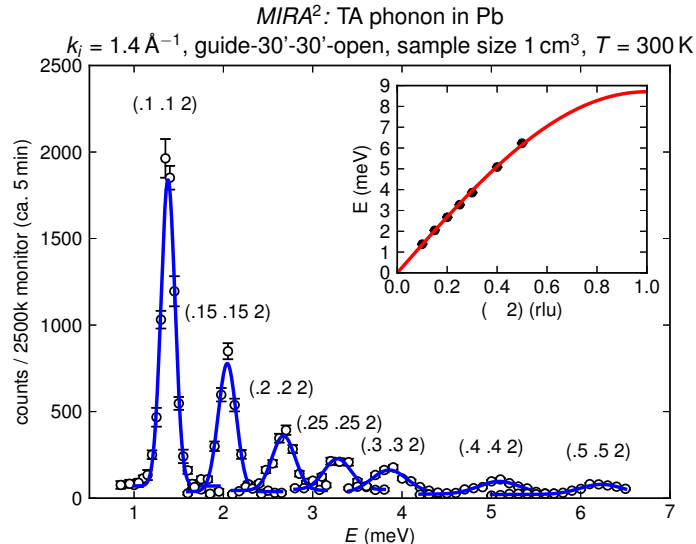


Figure 2: Phonons in lead measured with the MIRA triple axis option. Two 30-minute collimators were used before and after the sample. The inset shows the acoustic phonon branch in lead extracted from the constant  $k_i$  scans.

### References

- [1] Gen Shirane, Stephen Shapiro, and John Tranquada, *Neutron Scattering with a Triple Axis Spectrometer*, Cambridge University Press, 2002.

# Tests of Modulated Intensity Small Angle Scattering in Time of Flight Mode

Georg Brandl<sup>2, 1</sup>, Jyotsana Lal<sup>3</sup>, Lee Robertson<sup>4</sup>, Markus Bleuel<sup>5</sup>, Peter Böni<sup>1</sup>

<sup>1</sup>Physik-Department E21, Technische Universität München, D-85748 Garching, Germany.

<sup>2</sup>Forschungszentrum für Neutronenphysik und Materialforschung (FRM II), Technische Universität München, D-85748 Garching, Germany.

<sup>3</sup>Argonne National Laboratory, Materials Science Division, Argonne, IL 60439, USA.

<sup>4</sup>Oak Ridge National Laboratory, Oak Ridge, TN 37831-6477, USA.

<sup>5</sup>Technical University of Delft, 2629JB Delft, Netherlands.

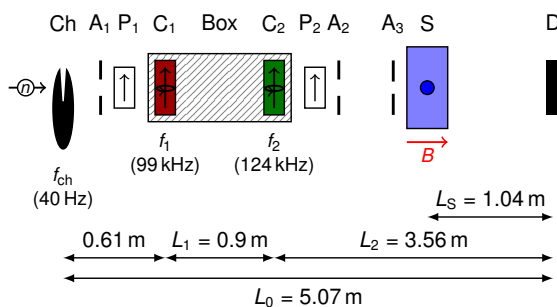
## Introduction

MISANS, MIEZE (Modulation of Intensity with Zero Effort) in the Small Angle Neutron Scattering (SANS) geometry is a rather new technique to probe quasi-elastic scattering with extremely high energy resolution. The method is well understood [4] and efforts are under way [1, 2] to establish the technique as a standard tool for measurements of slow dynamics.

The general trend of new neutron sources to be accelerator driven and thus to provide pulsed neutron beams raises the question how MISANS will perform in a pulsed mode. In earlier experiments the feasibility of MISANS on pulsed sources was demonstrated [5], however these tests were at relative low MIEZE frequencies. The goal of this experiment was to show that a MIEZE can be set up easily at a new beamline and works well in the time-of-flight mode with samples. Therefore a compact turn-key MISANS setup from the FRM II in Munich was installed at the HFIR in Oak Ridge, Tennessee, USA, at the beamline CG-1D [3].

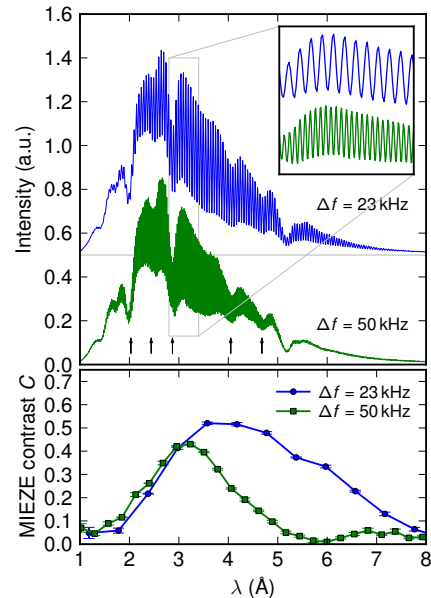
## Setup of the Experiment

The used setup is shown here: Two sets of MIEZE coils inside  $\mu$ -metal shielding [1] are placed between two polarizers (P). The chopper (Ch) provided a pulsed beam with a frequency of 40 Hz and a pulse length of 0.14 ms. The frequencies in the RF coils ranged between 46 and 149 kHz and matched the Larmor frequency of the static fields. The sample (S) was placed inside a cryomagnet. The detector (D) was a fast micro-channel plate area detector.

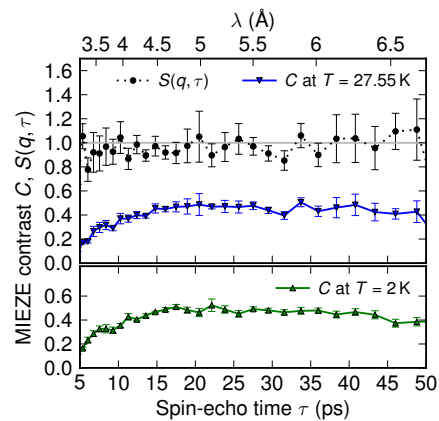


## Results

The next figure shows the result of a first test, a MIEZE modulation on the time-of-flight spectrum with two different frequencies. The absorption edges of aluminum and silicon are clearly visible as dips in the spectra and were used to calibrate the time-of-flight to wavelength conversion. The RF frequencies were 46/69 kHz and 99/149 kHz, respectively, with distances  $L_1 = 0.9$  m and  $L_2 = 1.8$  m to fulfill the MIEZE condition. The maximum contrast in our tests was about 50 %.



The last figure shows a measurements of neutrons scattered by the helical magnetic order in a MnSi sample placed inside the cryostat at zero field.



The blue curve shows the contrast measured in the neutron beam scattered by the MnSi sample at  $T = 27.55$  K at the Bragg peak at  $q = 0.035 \text{ \AA}^{-1}$  for different spin-echo times, corresponding to different wavelengths in the incoming beam. When compared with the green curve, which is the contrast at  $T = 2$  K, the black  $S(\tau)$  shows no decay in the intermediate scattering function as expected [1].

## References

- [1] R. Georgii, G. Brandl, N. Arend, W. Häußler, et al., Appl. Phys. Lett. **98**, 073505 (2011).
- [2] G. Brandl, R. Georgii, W. Häußler, S. Mühlbauer, and P. Böni, Nucl. Inst. Meth. A **654**, 394 (2011).
- [3] G. Brandl, J. Lal, J. Carpenter, L. Crow, L. Robertson, R. Georgii, P. Böni, and M. Bleuel, Nucl. Inst. Meth. A **667**, 1 (2012).
- [4] R. Gähler, R. Golub, and T. Keller, Physica B **156-157**, 653 (1989).
- [5] M. Bleuel et al., Physica B **371**, 297 (2006).

## The Instrument Design of KOMPASS – the New, Polarized TAS at FRM II

Alexander Grünwald<sup>1</sup>, Stefan Giemsa<sup>1</sup>, Peter Böni<sup>2</sup>, Markus Braden<sup>1</sup>

<sup>1</sup> II. Physikalisches Institut der Universität zu Köln, D-50937 Köln, Germany

<sup>2</sup> Physik-Department E21, Technische Universität München, D-85748 Garching, Germany.

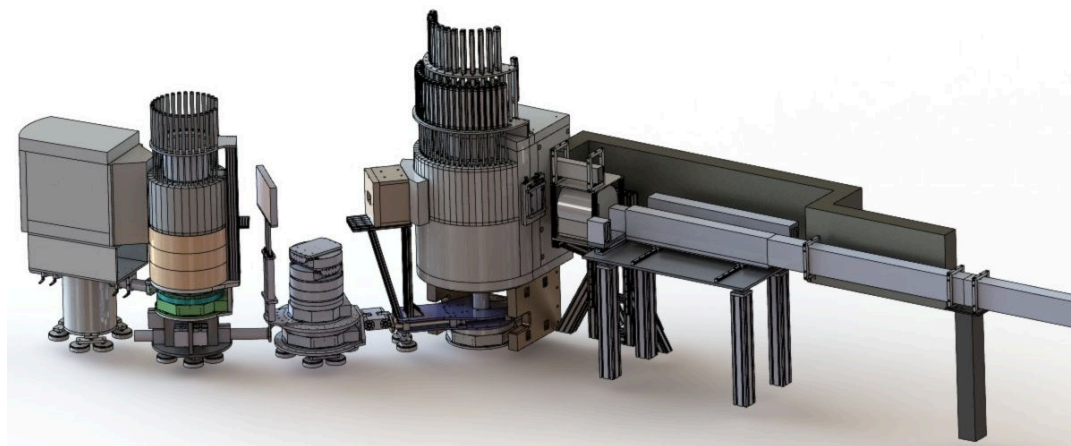


Figure 1: Design drawing of the KOMPASS (KOeln Münchner auf Polarisations-Analyse Spezialisiertes Spektrometer) and the instrument specific neutron guide, which will be located at the end of the guide NL1 in the neutron guide hall west at the FRM II.

The design of KOMPASS – the new, cold triple-axis spectrometer (to-be) at the FRM II – has been finalized. Based on previous calculations [1, 2, 3], the neutron guide between NREX+ (the next upstream instrument) and KOMPASS is parabolically focusing in the scattering plane and hosts three serial multi-channel V-cavities, which will provide a permanent high-polarized incident neutron beam with polarization rates of  $P > 99\%$  (simulated).

Motorized exchangeable parabolic and straight guide front ends allow for an optimized energy- and  $Q$ -resolution, respectively. The different guide front ends together with the variable double-focusing monochromator and analyzer thus provide a high flux with superior energy- and  $Q$ -resolution over a large dynamic range at a small sample volume. For measurements with high energy-resolution the parabolic guide front end can be used at the expense of a slightly reduced  $Q$ -resolution. In contrast, for measurements with high  $Q$ -resolution, or for the investigation of steep dispersion relations, the straight guide front end is available.

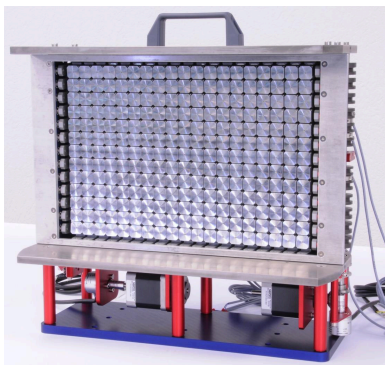


Figure 2: Picture of the variable double-focusing monochromator mechanics, showing  $19 \times 13$  crystal carriers and magnetic yokes at its top and bottom to close the magnetic flux lines of the permanent magnets at the rear side. (All rights reserved by SwissNeutronics.)

Permanent magnetic guide fields throughout the entire beam path preserve the high degree of neutron polarization.

The new designed, compact sample table, with inside driving mechanisms for the linear tables and the goniometer, has more space for sample environment; e.g. spherical neutron polarimetry with a mini MuPAD and a 3rd generation ILL system CryoPAD.

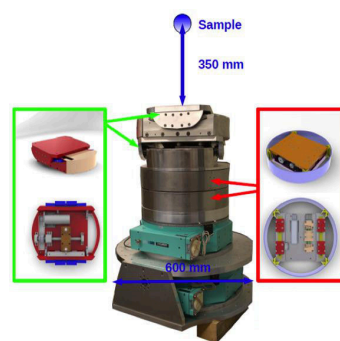


Figure 3: Picture of the sample table and design drawings of the inside driving mechanisms.

Higher order wavelength contaminations can be suppressed by an optional velocity selector in front of the monochromator.

As a result, KOMPASS will be ideally suited to investigate all types of weak magnetic ordering and magnetic excitations. In particular complex chiral magnetic structures, multiferroic and magneto-electric materials, high  $T_C$ -superconductors and quantum critical fluctuations are wide areas for potential applications.

This project is supported by the German Federal Ministry of Education and Research (BMBF) by project 05KN7PK1 & 05K10PK1.

### References

- [1] E21 Annual Report 2009/2010, Technische Universität München.
- [2] A.C. Komarek and P. Böni and M. Braden, Nuclear Instruments and Methods in Physics Research A **647**, 63 (2011).
- [3] M. Janoschek and P. Böni and M. Braden, Nuclear Instruments and Methods in Physics Research A **613**, 119 (2010).

# Polarisation Devices for the Spin-Echo Spectrometer RESEDA

Wolfgang Häußler<sup>2, 1</sup>, Julia Repper<sup>1, 2</sup>, Andreas Ostermann<sup>2</sup>, Jonas Kindervater<sup>1</sup>, Peter Böni<sup>1</sup>

<sup>1</sup> Physik-Department E21, Technische Universität München, Garching, Germany.

<sup>2</sup> Forschungsneutronenquelle Heinz Maier-Leibnitz (FRM II), Technische Universität München, Garching, Germany.

At the Neutron Resonance Spin Echo (NRSE) spectrometer RESEDA at FRM II, several studies on relatively slow magnetic fluctuations in ferro- and helimagnetic compounds have been performed. NRSE [1] can provide high momentum and energy resolution combined with high primary intensities, similar to Neutron Spin Echo (NSE) [2], because in both techniques the energy resolution is decoupled from the wavelength spread of the primary neutron beam. The information about dynamics in the sample is encoded in the beam polarization, which is prepared in the polarizer before the NRSE regions (polarizer 1 in Fig. 1), manipulated in the NRSE precession units, and finally determined by the analyzer-detector unit.

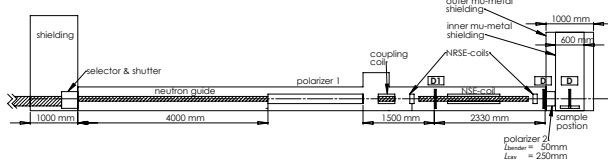


Figure 1: Schematic of RESEDA as simulated within McStas.

As the beam polarization is the measured quantity, the NSE and NRSE techniques suffer from a serious drawback: the statistical accuracy of the measurement strongly depends on the beam polarization and is severely decreased in the case of depolarizing samples. As a consequence, measurements in ferromagnetic materials are not possible due to the depolarization of the beam by the magnetic domains. The MIEZE-I technique, a variant of the NRSE method, is independent of the final beam polarization. The setup consists of a polarizer, two radio-frequency spin flipper coils (NRSE coils) and an additional analyzer. All components are located before the sample position. At the detector, the neutron beam may be unpolarized and the oscillating amplitude of the intensity yields the information about the sample dynamics. Thus, the depolarization neither due to the sample nor due to the sample environment does affect the measurement. The MIEZE-I unit is well suited as an additional option for RESEDA as the polarizer as well as the NRSE devices are already installed, and only an additional spin analyzer in front of the sample is needed (polarizer 2 in Fig. 1). We have employed Monte Carlo simulations by means of McStas [3] to optimize a new compact V-cavity-polarizer which will be installed just before the sample position of RESEDA in order to allow MIEZE-I measurements. Self-written components were combined with McStas built-in components to simulate the polarization [4] behind the V-cavity-polarizer in front of the NRSE devices and at the sample position behind the second polarizer.

To determine the polarization performance of polarizer 1 and validate the simulations the polarization was measured in front of the first NRSE device. These measurements were performed using a <sup>3</sup>He analyzer and a CCD camera. The results of the measurements and the simulations are in good agreement as shown in figure 2. The averaged polarization is 86 and 75% in the simulation compared to 84 and 72% in the measurement analyzed for different detector areas, re-

spectively. The small deviations between the simulated and the measured values may arise from a non perfect analyzer and guide field efficiency in the real experiment.

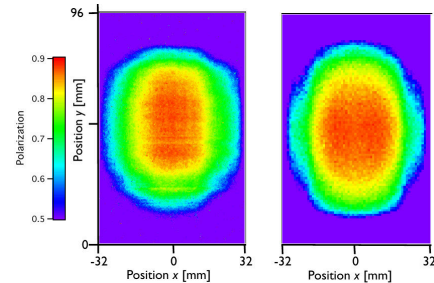


Figure 2: Polarization distribution as measured (left) and simulated by Monte Carlo simulations (right).

To simulate the performance of polarizer 2 behind the NRSE devices an unpolarized neutron beam was chosen (e.g. in MIEZE the beam may become depolarized by the NRSE coils). Therefore polarizer 1 was replaced by a neutron guide. The detectors to determine the polarization and the transmission were positioned directly in front of polarizer 2 and at the sample position (D in Fig. 1). The results of the V-cavity going to be installed at RESEDA are compared with a solid-state bender of the same outer dimensions (FIG. 3). The polarization behind the bender is 40%, compared to 80% behind the V-cavity at 3.8 Å. In contrast, the polarization of both devices is almost equal at 6 Å (bender: 94%, V-cavity: 91%). The figure of merit  $T^* = T \cdot P^2$  curve is larger for the cavity than for the bender reflecting the absorption of the neutron beam due to the 50 mm stack of silicon wafers in the bender, especially at larger wavelengths.

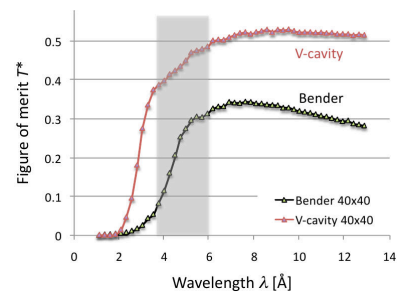


Figure 3: Figure of merit of the bender and the V-cavity, measured at the sample position. The highlighted area marks the wavelength range usually used at RESEDA.

Based on these simulations, the decision was made to install an additional V-cavity, which consists of five parallel channels just before the sample position. Using it as analyzer, will soon provide an optional MIEZE-I setup at RESEDA.

## References

- [1] R. Gähler and R. Golub, Z. Phys. B **65** 269-273 (1987).
- [2] F. Mezei, Z. Phys. A, **255**, 146-160 (1972).
- [3] K. Lefmann and K. Nielsen, Neutron News, **10**, 20-23 (1999).
- [4] J. Repper, W. Häußler, A. Ostermann, L. Kredler, A. Chacon and P. Böni, J. Phys. Conf. Series, **340**, 12036 (2012).

## The Upgrade of the Neutron Induced Positron Source NEPOMUC

C. Hugenschmidt<sup>1, 2</sup>, H. Ceeh<sup>1</sup>, T. Gigl<sup>1</sup>, F. Lippert<sup>1</sup>, C. Piochacz<sup>1, 2</sup>, P. Pikart<sup>1</sup>,  
M. Reiner<sup>1</sup>, K. Schreckenbach<sup>1, 2</sup>, S. Vohburger<sup>2</sup>, J. Weber<sup>1</sup>, S. Zimnik<sup>1</sup>

<sup>1</sup> Physik Department E21, Technische Universität München, D-85747 Garching, Germany

<sup>2</sup> Forschungsneutronenquelle Heinz Maier-Leibnitz (FRM II), Technische Universität München, D-85747 Garching, Germany

The principle of the in-pile positron source NEPOMUC at the research reactor FRMII is based on the emission of high-energy prompt  $\gamma$ -rays after thermal neutron capture in  $^{113}\text{Cd}$ . A structure of Pt foils converts the released high-energy  $\gamma$ -radiation into positron-electron pairs and leads to the emission of mono-energetic positrons. Until 2010, NEPOMUC has been operated successfully with an intensity of about  $10^9$  moderated positrons per second [1]. The lifetime of the first positron source, which used an converter of natural Cd with a thickness of 3 mm, was limited by the burn-up of  $^{113}\text{Cd}$  after 1250 days of reactor operation at the nominal power of 20 MW. For this reason, the inclined beam tube SR11 with the in-pile positron source has been replaced. The main task for the new positron source NEPOMUC *upgrade* was a considerable extension of the operation time to 25 years. In order to enhance the intensity and the beam brightness, additional improvements have been made to the design of the source components [2].

### NEPOMUC upgrade

As shown in figure 1, NEPOMUC *upgrade* consists of three main components: (i) the outer 'beam tube' surrounded by the  $\text{D}_2\text{O}$  of the moderator tank and with Cd inside the tip, (ii) the 'experimental tube' carrying the magnetic coils for positron beam transport, and (iii) the innermost 'potential tube' with the Pt foil structure and electric lenses.

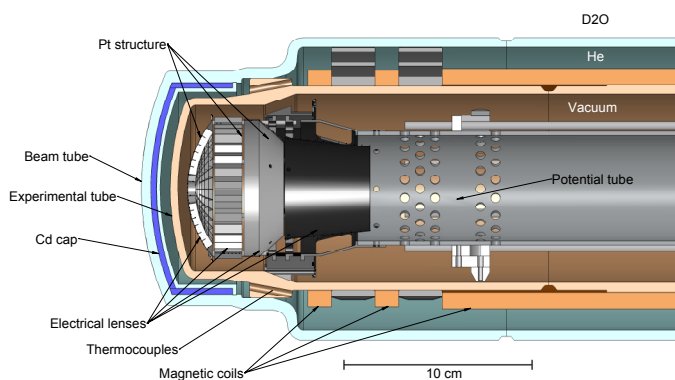


Figure 1: Cross sectional view of the new in-pile positron source NEPOMUC *upgrade*.

For the extension of the operation time, Cd enriched with 80%  $^{113}\text{Cd}$ , i.e. 6.5 times higher amount of  $^{113}\text{Cd}$  than in natural Cd, is applied at NEPOMUC *upgrade*. Absorption of high energy  $\gamma$ -quanta in the Pt front section with additional small vanes and in the electrical lenses contribute to the positron production. For the formation of a high brightness beam, only the moderated positrons from the Pt front plate with low transverse momentum are collected. A higher total moderation efficiency is expected due to the improved geometry and (inelastic) scattering of positrons from the Pt lenses onto the front moderation foil. A combination of electric and magnetic fields is used to accelerate and to form the beam. The electric and magnetic fields in the

beam formation stage were simulated for various configurations by finite element calculations in order to enhance both the beam intensity and its brightness [2].

### Generation of a high-brightness positron beam

In order to minimize transport losses the positrons are guided adiabatically, i.e. with low kinetic energy. For this purpose, the potential of the 'potential tube' and the insulated tube inside the chicane through the biological shield can be biased. Outside the biological shield, the positron beam can be guided to a remoderator using a W(100) crystal in back reflexion geometry for further brightness enhancement [3]. The primary (remoderated) positron beam is transported with a kinetic energy of  $E=1\text{ keV}$  (20 eV) in a magnetic guide field of typically 7 mT. A new beam switching and remoderation unit allows quick toggling between the primary high-intensity and the high-brightness remoderated positron beam [2].

For NEPOMUC *upgrade*, an intensity of up to  $3 \cdot 10^9$  moderated positrons per second is envisaged. The finally achievable positron intensity strongly depends on various effects such as amount of (in-)elastically scattered positrons, which contribute to the primary positron beam, moderation efficiency of the Pt moderator at high temperature and in the radiation field as well as the beam extraction and formation at the tip of the beam tube. The total efficiency of the beam guiding and focusing at the remoderation unit –and hence the yield of remoderated positrons– is expected to be higher than at the former source due to the higher brightness of the primary beam at NEPOMUC *upgrade*.

In 2012, first tests confirmed the operational reliability of SR11 [4], and the primary positron beam was successfully guided to the outside of the reactor pool. Presently, various parameters are adjusted such as potentials of the moderator, electric lenses and potential tube as well as magnetic guide and compensation fields for proper beam extraction. The shape and the intensity of the positron beam are determined at the first accessible position outside the reactor shielding.

The authors thank the group of G. Dollinger (UniBW) for the continuous support to operate PLEPS at NEPOMUC. Funding of the DFG project no. A3 within the Transregional Collaborative Research Center TRR 80 and of the BMBF project no. 05K10WOB is gratefully acknowledged.

### References

- [1] C. Hugenschmidt, B. Löwe, J. Mayer, C. Piochacz, P. Pikart, R. Repper, M. Stadlbauer, and K. Schreckenbach, Nucl. Instr. Meth. A, **593**, 616 (2008).
- [2] C. Hugenschmidt, C. Piochacz, M. Reiner, and K. Schreckenbach, New Journal of Physics, **14**, 055027 (2012).
- [3] C. Piochacz, G. Kögel, W. Egger, C. Hugenschmidt, J. Mayer, K. Schreckenbach, P. Sperr, M. Stadlbauer, and G. Dollinger, Appl. Surf. Sci., **255**, 98 (2008).
- [4] C. Hugenschmidt, H. Ceeh, T. Gigl, C. Piochacz, P. Pikart, M. Reiner, K. Schreckenbach, and J.A. Weber, J. Phys.: Conf. Ser., in press, (2012).

# Monte-Carlo Simulations for the Optimisation of a TOF-MIEZE Instrument

Tobias Weber<sup>1, 2</sup>, Georg Brandl<sup>1, 2</sup>, Robert Georgii<sup>1, 2</sup>, Wolfgang Häußler<sup>1, 2</sup>,  
Stefan Weichselbaumer<sup>2</sup>, Peter Böni<sup>1</sup>

<sup>1</sup> Physik-Department E21, Technische Universität München, D-85748 Garching, Germany.

<sup>2</sup> Forschungsneutronenquelle Heinz Maier-Leibnitz (FRM II), Technische Universität München, D-85748 Garching, Germany.

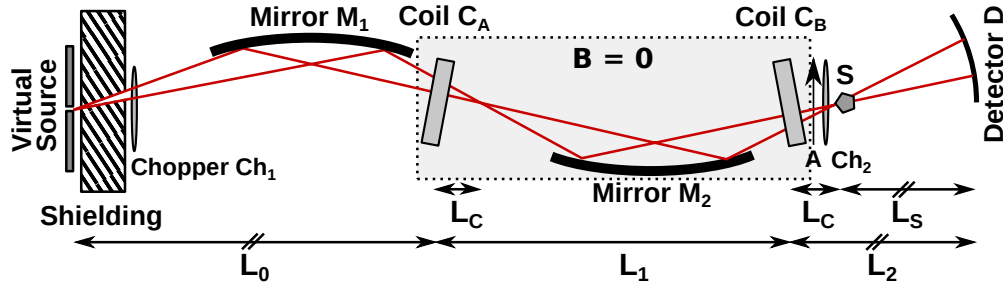


Figure 1: A simplified model of the TOF-MIEZE instrument used in the Monte-Carlo simulation. Figure reproduced from [5].

## Introduction

MIEZE (Modulation of Intensity Emerging from Zero Effort) [1, 2, 3] is a powerful technique for measuring the linewidths  $\Gamma$  of excitations or quasi-elastic dynamics with an extremely high energy resolution. The method is a refinement of the well-known spin-echo concepts NSE (Neutron Spin-Echo) and NRSE (Neutron Resonance Spin-Echo). The basic variable of these techniques is the polarisation of the neutrons. For MIEZE it is the contrast of the time modulated signal.

The goal of this work was two-fold: Firstly, we verified the theoretical model for the contrast reduction caused by the sample as analytically calculated in Ref. [4] using Monte-Carlo simulations. Secondly, we studied the feasibility of a new instrumental concept for the ESS.

## Reproduction of previous results

Figure 2 shows the reduction in MIEZE contrast caused by a cuboid sample for several spin-echo times  $\tau_M$ . The values are derived for a MIEZE setup using straight beam paths with the distances between the coils  $L_1 = 1$  m, the distance from the second coil to the detector  $L_2 = 2$  m, the distance from the sample to the detector  $L_s = 0.8$  m and a wavelength of  $10.4 \text{ \AA}$ . Note the excellent agreement between the Monte-Carlo simulations (solid coloured lines), the theoretical [4] (dashed black lines), and experimental [4] (points with errorbars) values.

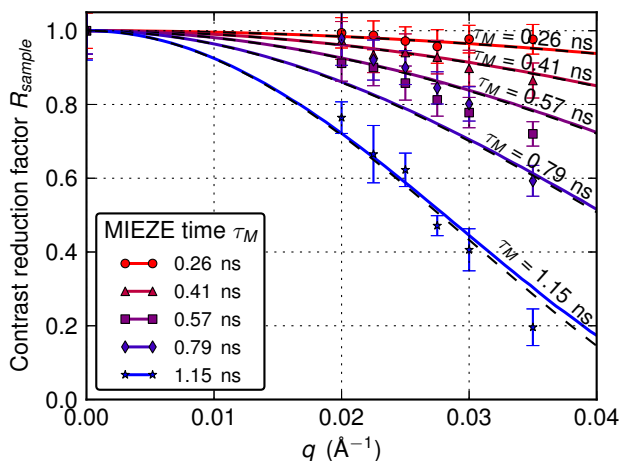


Figure 2: Contrast reduction for different spin-echo times  $\tau_M$ . Figure reproduced from [5].

## A new instrument design for ESS

The instrument design as shown in figure 1 was simulated using the Monte-Carlo technique. The distances indicated in the figure are  $L_0 = 13$  m,  $L_1 = 16$  m,  $L_2 = 16$  m,  $L_c = 3$  m, and  $L_s = 13$  m. We were able to show that the maximum available spin-echo time  $\tau_M$  using such an instrument configuration using pairs of Montel mirrors can reach the magnitude of micro seconds (figure 3) [5].

The instrument concept based on Montel mirror optics therefore enables us to reach an energy resolution  $\Delta E < 1$  neV while retaining an optimal illumination of the sample by the mirror configuration.

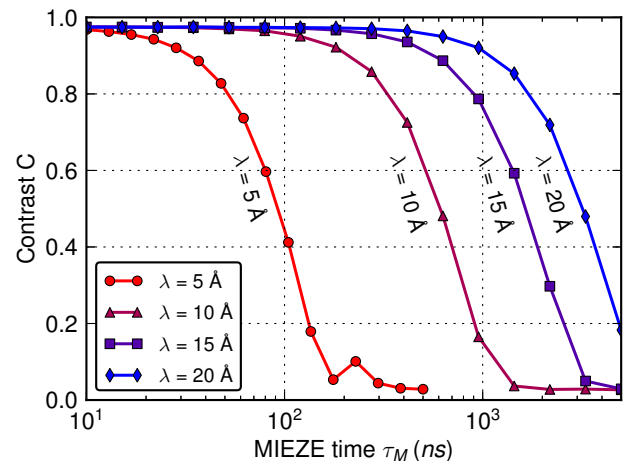


Figure 3: The available MIEZE times  $\tau_M$  for the TOF-MIEZE instrument as given by Monte-Carlo simulations. Figure reproduced from [5].

## References

- [1] R. Gähler, R. Golub, T. Keller, Physica B **180-181**, 899 (1992).
- [2] W. Besenböck, R. Gähler, P. Hank, R. Kahn, M. Köppe, C.-H. De Novion, W. Petry, J. Wuttke, Journal of Neutron Research **7**, 65 (1998).
- [3] R. Georgii, G. Brandl, N. Arend, W. Häußler, A. Tischendorf, C. Pfeleiderer, P. Böni, J. Lal, Applied Physics Letters **98**, 073505 (2011).
- [4] G. Brandl, R. Georgii, W. Häußler, S. Mühlbauer, and P. Böni, Nuclear Instruments and Methods A **654**, 394 (2011).
- [5] T. Weber, G. Brandl, R. Georgii, W. Häußler, S. Weichselbaumer, P. Böni, Nuclear Instruments and Methods A, doi: 10.1016/j.nima.2013.03.010, accepted (2013).



# Wavelength Frame Multiplication Chopper System for a Multi-Purpose Imaging Beamline at the European Spallation Source

Philipp Schmakat<sup>1, 2</sup>, Michael Schulz<sup>2</sup>, Marc Seifert<sup>2</sup>, Peter Böni<sup>1</sup>, Markus Strobl<sup>3</sup>

<sup>1</sup>Physik-Department E21, Technische Universität München, D-85748 Garching, Germany.

<sup>2</sup>Forschungs-Neutronenquelle Heinz Maier-Leibnitz (FRM II), D-85748 Garching, Germany.

<sup>3</sup>European Spallation Source ESS-AB, Tunavägen 24, 22100 Lund, Sweden

## Introduction

The European Spallation Source (ESS) will be one of the world's brightest neutron sources where neutrons are produced from a spallation target hit by accelerated protons. Since the ESS in contrast to all other existing spallation sources will deliver very long neutron pulses of 2.86 ms duration at a frequency of 14 Hz, new monochromatization techniques are under investigation to utilize this time structure efficiently. We have investigated a highly flexible chopper system based on the concept of wavelength frame multiplication (WFM) using optically blind choppers [1, 2, 3], being able to access a variable wavelength band with an adjustable wavelength resolution that is nearly constant over the entire spectrum. An imaging instrument at the ESS will benefit from such a chopper system due to high gain factors compared to facilities at existing neutron sources, especially when considering wavelength-dependent imaging techniques such as depolarization imaging [4], strain imaging [5] or dark field imaging [6].

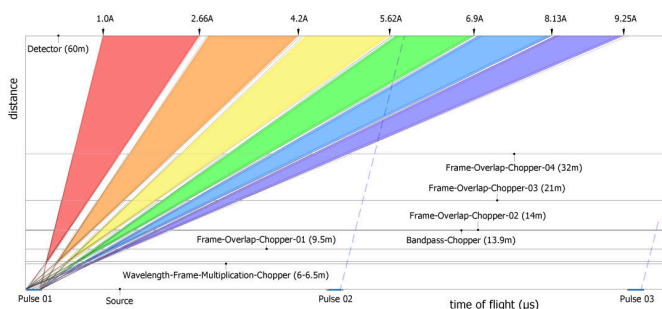


Figure 1: Time of flight vs. flight distance diagram to define the appropriate chopper positions and parameters for a WFM chopper system. Six wavelength frames cover a spectrum 1 - 9 Å, every second ESS pulse is skipped using a bandpass chopper.

## Wavelength Frame Multiplication Concept

The time structure of neutron pulses at the ESS and the high average flux may open up a broad spectrum of applications and experiments that become feasible for the first time. This requires dedicated instruments with new and sophisticated concepts for monochromatization. The following requirements were proposed for an imaging instrument at the ESS: It should deliver a constant wavelength resolution over a broad spectrum in the range 1 Å to 9 Å. The spatial and spectral homogeneity at the detector should be suitable for imaging experiments, i.e. the detector should be homogeneously illuminated by every wavelength accessible. An instrument based on the WFM chopper system proposed in this study will feature a range of wavelength resolutions  $\Delta\lambda/\lambda$  adjustable from 0.2% to 0.9% (high resolution mode) where the resolution is nearly constant over the entire spectrum. The resolution can be adjusted by varying the distance of a pair of optically blind WFM choppers. Several

frame overlap (FO) choppers are included to avoid overlap and crosstalk of neighbored wavelength frames in order to achieve the desired resolution. The high resolution mode is suitable for non-standard techniques where a high degree of monochromatization is required. Additionally, a low resolution mode where all choppers except one bandpass chopper are stopped and set open can be used, resulting in a rather coarse and wavelength-dependent resolution. The low resolution mode is included as a natural consequence from the instrument length which was proposed to be 60 m in order to achieve a coarse resolution in the range 2 - 10%. The chopper arrangement has been designed, first theoretically by constructing time of flight diagrams (see Fig. 1) and then implemented into a virtual instrument using the Monte Carlo simulation software McStas. The virtual instrument allowed us to optimize the WFM chopper system by refining the chopper parameters. This study may therefore act as a benchmark for similar instrument concepts that will be proposed for long pulse neutron sources such as the ESS.

## Simulation Results

The WFM chopper system has been implemented into a neutron guide system, that has been proposed for a future multi-purpose imaging beamline at the ESS. The chopper parameters have been optimized according to the requirements of the guide system. Fig. 2 shows a result of our simulations, that demonstrates the performance of the high resolution mode. The wavelength band is divided into six wavelength frames, that are sufficiently separated in time. The chopper system performs well, as can be seen from the fact, that the spectrum at the detector is still continuous and shows no significant gaps. Further optimization is ongoing to eliminate frame overlap and dips in the wavelength spectrum as far as possible.

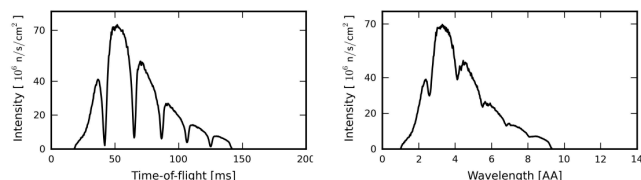


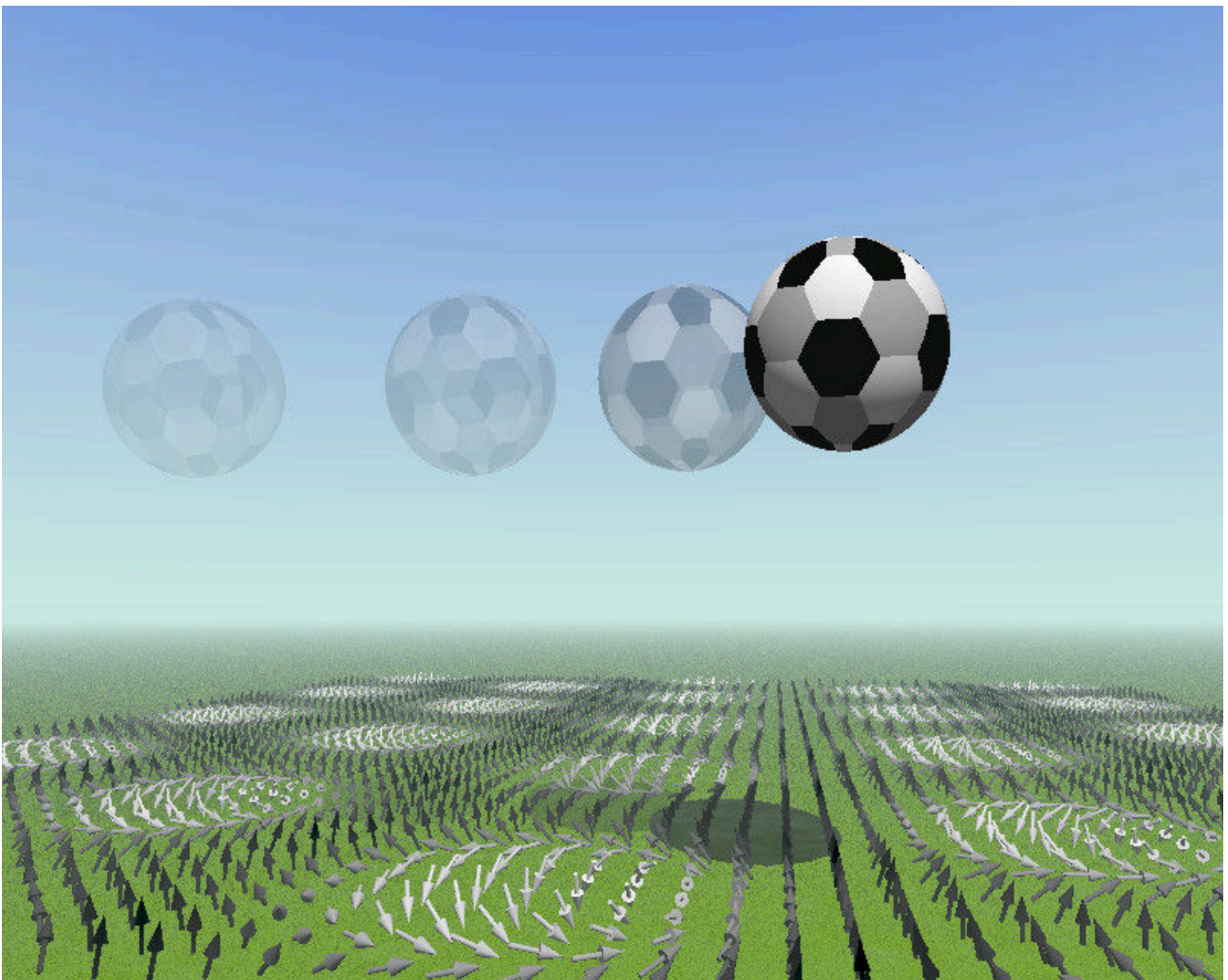
Figure 2: Results of the Monte Carlo simulations. The WFM chopper system is tuned for a wavelength resolution of 0.9%.

## References

- [1] F. Mezei, M. Russina, Proc. of the SPIE 4785 (2002) 24
- [2] A.A. van Well, Physica B 180-181 (1992) 959
- [3] M. Strobl et al., NIM A 705 (2013) 74-84
- [4] M. Schulz et al., Physica B: Cond. Matt. 406 (2011) 2412-2414
- [5] J.R. Santisteban et al., NIM A 481 (2002) 765-768
- [6] C. Grünzweig et al., Appl. Phys. Lett. 93 (2008) 112504

# Chapter 6

## Activities



**Skyrmion Soccer**  
(by Karin Everschor-Sitte and Matthias Sitte)



## Lectures, Courses and Seminars

- Tim Adams**
- Tutor “Experimentalphysik 4” (SS 2010)
  - Tutor “Festkörperphysik” (WS 2010/11)
  - Tutor “Experimentalphysik für Chemiker” (WS 2011/12)
  - Preparation of the lecture script for “Experimentalphysik für Chemiker” (SS 2012)
  - Tutor “Festkörperphysik” (WS 2012/13)
- Andreas Bauer**
- Tutor/Instructor “Experimentalphysik 2” for TUM TwoInOne (SS 2011)
  - Exam corrector “Experimentalphysik 2” for TUM TwoInOne (SS 2011)
- Peter Böni**
- Lecture “Physics with Neutrons I” (WS 2010/11, WS 2011/12, WS 2012/13)
  - Lecture “Physics with Neutrons II” (SS 2011, SS 2012)
  - Lecture “Experimentalphysik für Chemie-Ingenieurwesen und Restauratoren” (WS 2011/12, WS 2012/13)
  - Seminar “Neutronen in Forschung und Industrie”, together with Prof. W. Petry, Prof. K. Schreckenbach, and Dr. W. Häußler (2011 and 2012)
  - Seminar “Experimentelle Methoden in der Festkörperphysik”, together with Prof. C. Pfeiderer, and PD Dr. C. Hugenschmidt (2011 and 2012)
  - Seminar “Methods and Experiments in Neutron Scattering”, together with PD Dr. C. Morkel (2011 and 2012)
  - Solid State Physics Colloquium of the Transregio TRR 80
- Georg Brandl**
- Tutor “Experimentalphysik 1” for TUM TwoInOne (SS 2011)
  - Tutor “Experimentalphysik 2” for TUM TwoInOne (SS 2011)
  - Tutor/Instructor “Physics with Neutrons I” (WS 2011/12)
  - Tutor/Instructor “Physics with Neutrons II” (SS 2012)
- Hubert Ceeh**
- Tutor “Physikalisches Fortgeschrittenenpraktikum” (since WS 2010/11)
- Alfonso Chacón**
- Tutor “Einführung in die Festkörperphysik” (WS 2012/13)
  - Tutor “Physics with Neutrons I” (WS 2012/13)
- Sarah Dunsiger**
- Member of the organising committee for the “Functionality of Correlated Materials” summer school (2012)
- Robert Georgii**
- Supervisor TUM Kolleg Otto-von-Taube Gymnasium (2011)
  - Burg Rothenfels Workshop (2011)
  - Supervisor for the “Fortgeschrittenenpraktikum” lab course FRM II (2011 and 2012)
- Marco Halder**
- Tutor “Einführung in die Physik der kondensierten Materie” (WS 2012/13)

- Christoph Hugenschmidt**
- Lecture “Physics with Positrons I and II” (since 2008/09)
  - Seminar “Current Topics in Positron Research: Theory and Experiments” (since 2010/11)
  - Seminar “Experimental Methods in Solid State Physics” (since 2003/04)
- Christopher Krey**
- Tutor “Experimentalphysik 1” for TUM TwoInOne (SS 2011)
  - Tutor/Instructor “Experimentalphysik 2” for TUM TwoInOne (SS 2011)
  - Tutor “Einführung in die Physik der kondensierten Materie” (WS 2012/13)
- Christoph Morkel**
- Lecture “Reaktorphysik 1 und neue Konzepte in der Kerntechnik” (WS 2010/11, WS 2011/12, WS 2012/13)
  - Lecture “Reaktorphysik 2 und neue Konzepte in der Kerntechnik” (SS 2011, SS 2012)
  - Seminar “Methods and Experiments in Neutron Scattering”, together with Prof. Dr. Peter Böni (2011 and 2012)
- Christian Pfeiderer**
- Lecture “Experimentalphysik für Chemieingenieure” (WS 2010/11)
  - Lecture “Elektronische Korrelationen und Magnetismus I” (WS 2010/11)
  - Seminar “Experimentelle Methoden in der Festkörperphysik” (WS 2010/11, SS 2011, WS 2011/12, SS 2012, WS 2012/13)
  - Demonstrationsversuche für die Experimentalphysik (WS 2010/11, SS 2011, WS 2011/12, SS 2012, WS 2012/13)
  - TR80: Focussed Lectures (WS 2010/11, SS 2011, WS 2011/12, SS 2012, WS 2012/13)
  - Lecture “Experimentalphysik I” for TUM TwoInOne (SS 2011)
  - Lecture “Experimentalphysik II” for TUM TwoInOne (SS 2011)
  - Lecture “Elektronische Korrelationen und Magnetismus II” (SS 2011)
  - Lecture “Einführung in die Kristallzüchtung” (SS 2012)
  - Seminar “Vielteilchenphänomene und Streumethoden” (SS 2012)
  - Lecture “Einführung in die Festkörperphysik” (WS 2012/13)
- Alexander Regnat**
- Tutor “Experimentalphysik 1” for TUM TwoInOne (SS 2011)
  - Tutor “Experimentalphysik 2” for TUM TwoInOne (SS 2011)
  - Tutor “Einführung in die Festkörperphysik” (WS 2012)
- Tommy Reimann**
- Tutor “Einführung in die Festkörperphysik” (WS 2012)
- Markus Reiner**
- Tutor “Physikalisches Praktikum für Maschinenwesen” (SS 2011, SS 2012, WS 2012/13)
  - Tutor “Physik für Chemiker” (WS 2011/12, SS 2012)
- Robert Ritz**
- Tutor “Einführung in die Festkörperphysik” (WS 2010/2011)
  - Tutor “Experimentalphysik 1” (SS 2011)
  - Set-up of the new experiment “Magnetism” for the “Anfängerpraktikum” lab course (WS 2011/2012, SS 2012)

- Michael Wagner**
- Tutor “Experimentalphysik 1” for TUM TwoInOne (SS 2011)
  - Tutor “Experimentalphysik 2” for TUM TwoInOne (SS 2011)
- Josef Weber**
- Tutor “Physik für Lehramt Berufsschule” (WS 2012/13)
- Birgit Wiedemann**
- Tutor “Experimentalphysik 1” for TUM TwoInOne (SS 2011)
  - Tutor “Experimentalphysik 2” for TUM TwoInOne (SS 2011)
  - Tutor “Anfängerpraktikum” (SS 2011)
  - Tutor/Instructor “Experimentalphysik für Chemie-Ingenieurwesen und Restauratoren” (WS 2011/12)
  - Instructor “Experimentalphysik für Chemie-Ingenieurwesen und Restauratoren” (WS 2012/13)

## Publications

- [1] T. Adams, S. Mühlbauer, C. Pfeiderer, F. Jonietz, A. Bauer, A. Neubauer, R. Georgii, P. Böni, U. Keiderling, K. Everschor, M. Garst and A. Rosch, *Long-Range Crystalline Nature of the Skyrmion Lattice in MnSi*, Phys. Rev. Lett., **107** (2011).
- [2] P. Böni, B. Roessli and K. Hradil, *Inelastic neutron and x-ray scattering from incommensurate magnetic systems*, J. Phys. Condens. Matter, **23**, 254209–(1–9) (2011).
- [3] G. Brandl, R. Georgii, W. Häußler, S. Mühlbauer and P. Böni, *Large Scales - Long Times: Adding High Energy Resolution to SANS*, Nucl. Inst. Meth. A, **654**, 394–398 (2011).
- [4] H. Ceeh, S. Gärtner, C. Hugenschmidt, K. Schreckenbach, D. Schwalm and P. Thirolf, *Status report on the setup for the decay rate measurement of the negative positronium ion*, J. Phys. Conf. Ser., **262**, 012011 (2011).
- [5] H. Ceeh, C. Hugenschmidt, K. Schreckenbach, S. Gärtner, P. Thirolf, F. Fleischer and D. Schwalm, *Precision measurement of the decay rate of the negative positronium ion Ps-*, Phys. Rev. A, **84**, 062508 (2011).
- [6] S. R. Dunsiger, A. A. Aczel, C. Arguello, H. Dabkowska, A. Dabkowski, M.-H. Du, T. Goko, B. Javanparast, T. Lin, F. L. Ning, H. M. L. Noad, D. J. Singh, T. J. Williams, Y. J. Uemura, M. J. P. Gingras and G. M. Luke, *Spin Ice: Magnetic Excitations without Monopole Signatures Using Muon Spin Rotation*, Phys. Rev. Lett., **107**, 207207 (2011).
- [7] S. W. H. Eijt, H. Leegwater, H. Schut, A. Anastasopol, W. Egger, L. Ravelli, C. Hugenschmidt and B. Dam, *Layer-resolved study of the Mg to MgH<sub>2</sub> transformation in Mg-Ti films with short-range chemical order*, J. Alloys Compd., **509**, S567 – S571 (2011).
- [8] R. Georgii, G. Brandl, N. Arend, W. Häußler, A. Tischendorf, C. Pfeiderer, P. Böni and J. Lal, *Turn-key module for neutron scattering with sub-micro-eV resolution*, Appl. Phys. Lett., **98** (2011).
- [9] R. Gilles, M. Hofmann, F. Johnson, Y. Gao, D. Mukherji, C. Hugenschmidt and P. Pikart, *Analysis of antiphase domain growth in ternary FeCo alloys after different cooling rates and annealing treatments using neutron diffraction and positron annihilation*, J. Alloys Compd., **509**, 195–199 (2011).
- [10] D. Habs, M. Gross, P. G. Thirolf, and P. Böni, *Neutron halo isomers in stable nuclei and their possible application for the production of low energy, pulsed, polarized neutron beams of high intensity and high brilliance*, Appl. Phys. B, **103**, 485–499 (2011).
- [11] K.-U. Hess, A. Flaws, M. Mühlbauer, B. Schillinger, A. Franz, M. Schulz, E. Calzada, D. Dingwell and K. Bente, *Advances in high-resolution neutron computed tomography: Adapted to the earth sciences*, Geosphere, **7**, 1294–1302 (2011).
- [12] C. Hugenschmidt, *The status of the positron beam facility at NEPOMUC*, J. Phys. Conf. Ser., **262**, 012002 (2011).
- [13] P. C. Hungler, L. G. I. Bennett, W. J. Lewis, M. Schulz and B. Schillinger, *Neutron imaging inspections of composite honeycomb adhesive bonds*, Nucl. Inst. Meth. A (2011), in Press, Corrected Proof.
- [14] F. Kargl, M. Engelhardt, F. Yang, H. Weis, P. Schmakat, B. Schillinger, A. Griesche and A. Meyer, *In situ studies of mass transport in liquid alloys by means of neutron radiography*, J. Phys. Condens. Matter, **23**, 254201 (2011).
- [15] A. Komarek, P. Böni and M. Braden, *Parabolic versus elliptic focusing - Optimization of the focusing design of a cold triple-axis neutron spectrometer by Monte-Carlo simulations*, Nucl. Inst. Meth. A, **647**, 63–72 (2011).
- [16] R. W. Metzke, H. Runck, C. A. Stahl, B. Schillinger, E. Calzada, M. Mühlbauer, M. Schulz, M. Schneider, H.-J. Priebe, W. A. Wall and J. Guttmann, *Neutron computed tomography of rat lungs*, Phys. Med. Biol., **56**, N1 (2011).
- [17] S. Mühlbauer, C. Pfeiderer, P. Böni, E. M. Forgan, E. H. Brandt, A. Wiedenmann, U. Keiderling and G. Behr, *Time-resolved stroboscopic neutron scattering of vortex lattice dynamics in superconducting niobium*, Phys. Rev. B, **83** (2011).

- [18] A. Neubauer, J. Boeuf, A. Bauer, B. Russ, H. v. Loehneysen and C. Pfeiderer, *Ultra-high vacuum compatible image furnace*, Rev. Sci. Instrum., **82** (2011).
- [19] A. Paul, *Wavelength Resolution Options for a Reflectometer Using Vitess Code of Simulation*, Nucl. Inst. Meth. A, **646**, 158 (2011).
- [20] A. Paul, T. Krist, A. Teichert and R. Steitz, *Specular and Off-specular Scattering with Polarization and Polarization Analysis on Reflectometer V6 at BER II, HZB*, Physica B, **406**, 1598 (2011).
- [21] A. Paul, N. Paul and S. Mattauch, *Magnetization Reversal and Domain Correlation for a Noncollinear and Out-of-plane Exchange Coupled System*, New J. Phys., **13**, 063008 (2011).
- [22] C. Pfeiderer, *Magnetic Order Surfaces get hairy*, Nat. Phys., **7**, 673–674 (2011).
- [23] P. Pikart, C. Hugenschmidt, M. Horisberger, Y. Matsukawa, M. Hatakeyama, T. Toyama and Y. Nagai, *Positron annihilation in Cr, Cu, and Au layers embedded in Al and quantum confinement of positrons in Au clusters*, Phys. Rev. B, **84**, 014106 (2011).
- [24] C. Piochacz and C. Hugenschmidt, *The experimental determination of the phase space distribution of a positron beam*, J. Phys. Conf. Ser., **262**, 012049 (2011).
- [25] M. Schulz, P. Schmakat, C. Franz, A. Neubauer, E. Calzada, B. Schillinger, P. Böni and C. Pfeiderer, *Neutron depolarisation imaging: Stress measurements by magnetostriction effects in Ni foils*, Physica B, **406**, 2412 – 2414 (2011), proceedings of the 8th International Workshop on Polarised Neutrons for Condensed Matter Investigation.
- [26] D. A. Sokolov, R. Ritz, C. Pfeiderer, T. Keller and A. D. Huxley, *Neutron scattering studies of the lattice expansion in a ferromagnetic superconductor  $UGe_2$  under pressure*, in *J. Phys. Conf. Ser.*, vol. 273, 012085, IOP Publishing (2011).
- [27] J. Stahn, T. Panzner, U. Filges, C. Marcelot and P. Böni, *Study of a focusing, low-background neutron delivery system*, Nucl. Inst. Meth. A, **634**, S12–S16 (2011).
- [28] X. Xia, E. Metwalli, M. A., V. Körstgens, P. Busch, P. Böni and P. Müller-Buschbaum, *Nanostructured diblock copolymer films with embedded magnetic nanoparticles*, J. Phys. Condens. Matter, **23**, 254209–(1–9) (2011).
- [29] T. Adams, A. Chacon, M. Wagner, A. Bauer, G. Brandl, B. Pedersen, H. Berger, P. Lemmens and C. Pfeiderer, *Long-Wavelength Helimagnetic Order and Skyrmion Lattice Phase in  $Cu_2OSeO_3$* , Phys. Rev. Lett., **108**, 237204 (2012).
- [30] A. Bauer and C. Pfeiderer, *Magnetic phase diagram of  $MnSi$  inferred from magnetization and ac susceptibility*, Phys. Rev. B, **85** (2012).
- [31] P. M. Benson, M. J. Heap, Y. Lavallée, A. Flaws, K.-U. Hess, A. P. S. Selvadurai, D. B. Dingwell and B. Schillinger, *Laboratory simulations of tensile fracture development in a volcanic conduit via cyclic magma pressurisation*, Earth Planet. Sci. Lett., **349–350**, 231–239 (2012).
- [32] G. Brandl, J. Lal, J. Carpenter, L. Crow, L. Robertson, R. Georgii, P. Böni and M. Bleuel, *Tests of modulated intensity small angle scattering in time of flight mode*, Nucl. Inst. Meth. A, **667**, 1–4 (2012).
- [33] L. G. Butler, E. Lehmann and B. Schillinger, *Neutron radiography, tomography, and diffraction of commercial lithium-ion polymer batteries*, journal = *Physics Procedia* (2012).
- [34] K. Everschor, M. Garst, B. Binz, F. Jonietz, S. Mühlbauer, C. Pfeiderer and A. Rosch, *Rotating skyrmion lattices by spin torques and field or temperature gradients*, Phys. Rev. B, **86** (2012).
- [35] S. Haravifard, B. D. Gaulin, Z. Yamani, S. R. Dunsiger and H. A. Dabkowska, *Neutron scattering from the static and dynamic lattice of  $SrCu_2(BO_3)_2$  in its Shastry-Sutherland singlet ground state*, Phys. Rev. B, **85**, 134104 (2012).
- [36] T. D. Haynes, I. Maskery, M. W. Butchers, J. A. Duffy, J. W. Taylor, S. R. Giblin, C. Utfeld, J. Laverock, S. B. Dugdale, Y. Sakurai, M. Itou, C. Pfeiderer, M. Hirschberger, A. Neubauer, W. Duncan and F. M. Grosche, *Ferrimagnetism in Fe-rich  $NbFe_2$* , Phys. Rev. B, **85** (2012).
- [37] L. Helfen, T. F. Morgeneyer, F. Xu, M. N. Mavrogordato, I. Sinclair, B. Schillinger and T. Baumbach, *Synchrotron and neutron laminography for three-dimensional imaging of devices and flat material specimens*, Int. J. Mater. Res., 170–173 (2012).

- [38] R. M. Hengstler-Eger, P. Baldo, L. Beck, J. Dorner, K. Ertl, P. B. Hoffmann, C. Hugenschmidt, M. Kirk, W. Petry, P. Pikart and A. Rempel, *Heavy ion irradiation induced dislocation loops in AREVA's M5(R) alloy*, J. Nucl. Mater., **423**, 170–182 (2012).
- [39] C. Hugenschmidt, C. Piochacz, M. Reiner and K. Schreckenbach, *The NEPOMUC upgrade and advanced positron beam experiments*, New J. Phys., **14**, 055027 (2012).
- [40] C. Hugenschmidt, K. Schreckenbach, D. Habs and P. Thirolf, *High-intensity and high-brightness source of moderated positrons using a brilliant  $\gamma$  beam*, Appl. Phys. B, **106**, 241–249 (2012).
- [41] J. Kindervater, W. Häußler, A. Tischendorf and P. Böni, *Neutron-spin-echo from polarizing samples*, in J. Phys. Conf. Ser., vol. 340, 012030, IOP Publishing (2012).
- [42] J. D. Koralek, D. Meier, J. P. Hinton, A. Bauer, S. A. Parameswaran, A. Vishwanath, R. Ramesh, R. W. Schoenlein, C. Pfleiderer and J. Orenstein, *Observation of Coherent Helimagnons and Gilbert damping in an Itinerant Magnet*, Phys. Rev. Lett., **109**, 247204 (2012).
- [43] D. Korolkov, L. Willner, A. Schlachter, E. Kentzinger, H. Frielinghaus, A. Paul, M. Farle and T. Brückel, *The Analysis of Randomly Oriented Structures by Grazing Incidence Small Angle Neutron Scattering*, J. Appl. Cryst., **45**, 245 (2012).
- [44] C. Krey, S. Legl, S. R. Dunsiger, M. Meven, J. S. Gardner, J. M. Roper and C. Pfleiderer, *First Order Metamagnetic Transition in  $\text{Ho}_2\text{Ti}_2\text{O}_7$  Observed by Vibrating Coil Magnetometry at Milli-Kelvin Temperatures*, Phys. Rev. Lett., **108** (2012).
- [45] S. Legl, C. Krey, S. R. Dunsiger, H. A. Dabkowska, J. A. Rodriguez, G. M. Luke and C. Pfleiderer, *Vibrating-Coil Magnetometry of the Spin Liquid Properties of  $\text{Tb}_2\text{Ti}_2\text{O}_7$* , Phys. Rev. Lett., **109** (2012).
- [46] A. Neubauer, F. Jonietz, M. Meven, R. Georgii, G. Brandl, G. Behr, P. Böni and C. Pfleiderer, *Optical floating zone growth of high-quality  $\text{Cu}_2\text{MnAl}$  single crystals*, Nucl. Inst. Meth. A, **688**, 66–74 (2012).
- [47] A. Paul, *Grazing Incidence Polarized Neutron Scattering in Reflection Geometry from Nanolayered Spintronic Systems*, Pramana – J. Phys., **78**, 1 (2012).
- [48] A. Paul, N. Paul, C. Trautmann, J. Jutimoosik, R. Yimnirun, S. Rujirawat, B. Höpfner, I. Lauermann, M. Lux-Steiner, S. Mattauch and P. Böni, *Direct Manipulation of the Uncompensated Antiferromagnetic Spins in Exchange Coupled System by GeV Ion Irradiation*, Appl. Phys. Lett., **100**, 253102 (2012).
- [49] A. Paul, C. Schmidt, N. Paul, S. Mattauch, A. Ehresmann and P. Böni, *Magnetization Reversal in Ion-irradiated, Field Grown and/or Field Cooled Polycrystalline Exchange Coupled Systems*, Phys. Rev. B, **86**, 094420 (2012).
- [50] N. Paul, A. Paul, M. Kreuzer, R. Steitz and M. C. Lux-Steiner, *Selective Self Assembly of Neurotransmitter Molecules on Polyelectrolyte Multilayers*, J. Phys. Chem. B, **1116**, 4492 (2012).
- [51] M. Reiner, P. Pikart and C. Hugenschmidt, *Annealing of thin metallic films studied by depth dependent DB-spectroscopy and free Ps annihilation*, Physics Procedia, **35**, 104 (2012).
- [52] J. Repper, W. Häußler, A. Ostermann, L. Kredler, A. Chacón and P. Böni, *The new polarizer device at RESEDA*, J. Phys. Conf. Ser., **340**, 012036–(1–5) (2012).
- [53] K. Schörner, M. Goldammer, K. Stierstorfer, J. Stephan and P. Böni, *Scatter Correction Method by Temporal Primary Modulation in X-Ray CT*, IEEE Trans. Nucl. Sci., **59**, 3278–3285 (2012).
- [54] T. Schulz, R. Ritz, A. Bauer, M. Halder, M. Wagner, C. Franz, C. Pfleiderer, K. Everschor, M. Garst and A. Rosch, *Emergent electrodynamics of skyrmions in a chiral magnet*, Nat. Phys., **8**, 301–304 (2012).
- [55] K. M. Seemann, A. Bauer, J. Kindervater, M. Meyer, C. Besson, M. Luysberg, P. Durkin, W. Pyckhout-Hintzen, N. Budisa, R. Georgii, C. M. Schneider and P. Kögerler, *Polyoxometalate-Stabilized Water Dispersible  $\text{Fe}_2\text{Pt}$  Magnetic Nanoparticles*, Nanoscale (2012), accepted.
- [56] S. Seki, J.-H. Kim, D. Inosov, R. Georgii, B. Keimer, S. Ishiwata and Y. Tokura, *Formation and rotation of skyrmion crystal in a chiral-lattice insulator  $\text{Cu}_2\text{OSeO}_2$* , Phys. Rev. B, **85**, 220406 (2012).
- [57] T. Sunn Pedersen, J. R. Danielson, C. Hugenschmidt, G. Marx, X. Sarasola, F. Schauer, L. Schweikhard, C. M. Surko and E. Winkler, *Plans for the creation and studies of electron-positron plasmas in a stellarator*, New J. Phys., **14**, 035010 (2012).

- [58] R. Würschum, B. Oberdorfer, E.-M. Steyskal, W. Sprengel, W. Puff, P. Pikart, C. Hugenschmidt and R. Pippan, *Free volumes in bulk nanocrystalline metals studied by the complementary techniques of positron annihilation and dilatometry*, *Physica B*, **407**, 2670–2675 (2012).
- [59] A. Paul and S. Mattauch, *Induced Moment due to Perpendicular Field Cycling in Trained Exchange Bias System*, *Pramana – J. Phys.*, 9913 (2013).
- [60] A. Paul, N. Paul, J. Jutimoosik, R. Yimmirun, S. Rujirawat, B. Höpfner, I. Lauermann, M. Lux-Steiner, S. Mattauch and P. Böni, *Change in Interface-Magnetism of an Exchange Coupled System due to the Presence of Non-Magnetic Spacers*, *Phys. Rev. B*, **87**, 014431 (2013).
- [61] N. Paul, M. Müller, A. Paul, E. Günther, I. Lauermann, P. Müller-Buschbaum and M. C. Lux-Steiner, *Molecularly Imprinted Conductive Polymers for Controlled Trafficking of Neurotransmitter at Solid-liquid Interfaces*, *Soft Matter*, **9**, 1364 (2013).

## Conferences, Workshops and Seminar Contributions

- [1] T. Adams, *Role of magnetic anisotropies for the skyrmion lattice in MnSi*, Talk. Frühjahrstagung der Deutschen Physikalischen Gesellschaft, Berlin, Germany (2012).
- [2] T. Adams, *Neutron scattering studies of skyrmion lattices in chiral magnets*, Talk. Dresden, Germany (2012).
- [3] T. Adams, *Impurities and Textures in Unconventional Magnets*, Talk. (2012).
- [4] T. Adams, *Neutron scattering studies of skyrmion lattices in chiral magnets*, Talk. Korea International conference on magnetism, Busan, Korea (2012).
- [5] T. Adams, *Neutron scattering studies of skyrmion lattices in chiral magnets*, Talk. Sapporo, Japan Sagamore (2012).
- [6] A. Bauer, T. Adams, C. Franz, A. Neubauer, M. Hirschberger, C. Krey, R. Georgii, P. Böni, M. Garst and C. Pfleiderer, *Quantum Phase Transitions in  $Mn_{1-x}Fe_xSi$  and  $Mn_{1-x}Co_xSi$* , Talk. Frühjahrstagung der Deutschen Physikalischen Gesellschaft, Dresden, Germany (2011).
- [7] A. Bauer, *Next Generation of nuclear power plants*, Talk. TRR80 Young Researcher Workshop, Kleinwiesertal, Austria (2011).
- [8] A. Bauer, C. Franz, R. Korntner, D. Mallinger, L. Offermann, S. Gottlieb-Schönmeyer and C. Pfleiderer, *Progression Report on Project A1: Single Crystal Growth of Metals with Complex Order*, Talk. Retreat Meeting TRR80, Freising, Germany (2011).
- [9] A. Bauer, *Single Crystal Growth and Low Temperature Properties of Metals with Complex Order*, Talk. E21 Doktorandenseminar, Garching, Germany (2011).
- [10] A. Bauer, T. Adams, C. Dollinger, C. Franz, W. Münzer, A. Neubauer, S. Mühlbauer, F. Jonietz, R. Georgii, P. Böni, B. Pedersen, A. Rosch and C. Pfleiderer, *Skyrmion lattice in the doped semiconductor  $Fe_{1-x}Co_xSi$* , Poster. Strongly Correlated Electron Systems, Cambridge, UK (2011).
- [11] A. Bauer, A. Regnat, S. Gottlieb, K. Mittermüller, C. Blum, S. Wurmehl and C. Pfleiderer, *Single Crystal Growth of  $CrB_2$  and  $YMn_2$* , Poster. International Workshop Functionality from Heterostructures, Obergurgl, Austria (2011).
- [12] A. Bauer, A. Regnat, S. Gottlieb-Schönmeyer, M. Wagner, C. Blum, S. Wurmehl, B. Büchner and C. Pfleiderer, *Single Crystal Growth and Low Temperature Properties of the Itinerant Antiferromagnet  $Cr^{11}B_2$* , Talk. Seminar am Institut für Werkstofforschung, Dresden, Germany (2012).
- [13] A. Bauer, A. Regnat, S. Gottlieb-Schönmeyer, M. Wagner, C. Blum, S. Wurmehl, B. Büchner and C. Pfleiderer, *Hot Tungsten Crucibles for the Single Crystal Growth of the Itinerant Antiferromagnet  $Cr^{11}B_2$* , Talk. TRR80 Young Researchers Forum, Garching, Germany (2012).
- [14] A. Bauer, A. Neubauer, S. Gottlieb-Schönmeyer, C. Franz, M. Wagner, R. Bozhanova, D. Mallinger, K. Mittermüller, R. Korntner, G. Benka, M. Weber and C. Pfleiderer, *Progression Report on Project A1: Single Crystal Growth of Metals with Complex Order*, Talk. Retreat Meeting TRR80, Freising, Germany (2012).
- [15] A. Bauer and C. Pfleiderer, *On the magnetic phase diagram of B20 compounds inferred from magnetisation and ac susceptibility*, Talk. Frühjahrstagung der Deutschen Physikalischen Gesellschaft, Berlin, Germany (2012).
- [16] A. Bauer, A. Regnat, S. Gottlieb-Schönmeyer, M. Wagner, C. Blum, S. Wurmehl, B. Büchner and C. Pfleiderer, *High-Quality Single Crystal Growth of the Itinerant Antiferromagnet  $Cr^{11}B_2$* , Talk. Frühjahrstagung der Deutschen Physikalischen Gesellschaft, Berlin, Germany (2012).
- [17] A. Bauer, *On the Route to Skyrmionics*, Talk. E21 Doktorandenseminar, Garching, Germany (2012).
- [18] A. Bauer, *Emergent electrodynamics of skyrmions in chiral magnets*, Invited Talk. SPIE Optics and Photonics, San Diego, USA (2012).
- [19] A. Bauer, *Emergent electrodynamics of skyrmions in chiral magnets*, Talk. Seminar of the CONCEPT Group, Berkeley, USA (2012).

- [20] A. Bauer, A. Regnat, S. Gottlieb-Schönmeyer, M. Wagner, C. Blum, S. Wurmehl, B. Büchner and C. Pfeleiderer, *Itinerant antiferromagnetism in high-quality single crystal Cr<sup>11</sup>B<sub>2</sub>*, Poster. International Conference on Magnetism, Busan, Korea (2012).
- [21] P. Böni, *Superspiegelbeschichtungen für die Neutronenoptik*, Invited Talk. Kolloquium, Leibniz-Institut für Oberflächenmodifizierung e. V., Leibniz-Institut für Oberflächenmodifizierung, Leipzig, Germany (2011).
- [22] P. Böni, *Neutron Imaging and Scattering under Extreme Conditions*, Invited Talk. Seminar, Bayerisches Geoinstitut, Universität Bayreuth, Bayreuth, Germany (2011).
- [23] P. Böni, *Excitations in Incommensurate Magnetic Materials - Experiments with Neutrons*, Invited Talk. Stuttgarter Physikalisches Kolloquium, Max-Planck-Institut für Festkörperforschung und Intelligente Systeme, Stuttgart, Germany (2011).
- [24] P. Böni, *Chromium: Unraveling its Intriguing Properties*, Invited Talk. Ruhr-Universität Bochum, Germany (2011).
- [25] P. Böni, *Imaging with Neutrons: Scientific Applications*, Invited Talk. STAP-Meeting Imaging, European Spallation Source, Lund, Sweden (2012).
- [26] P. Böni, *Neutron Guides and Optics*, Invited Talk. Workshop on Second Guide Hall for OPAL, ANSTO, Sydney, Australia (2012).
- [27] P. Böni, *Neutronenoptik*, Interview. 7. Aargauer Wirtschaftstag, Unternehmenspreisverleihung, Wettingen, Switzerland (2012).
- [28] P. Böni, *Optische Komponenten für die Neutronenstreuung*, Invited Talk. Doktorandenseminar, Technische Universität München, Garching, Germany (2012).
- [29] G. Brandl, *MIEZE: A Larmor precession technique for  $\mu\text{eV}$  resolution in magnetic fields*, Talk. European Conference for Neutron Scattering, Prague, Czech Republic (2011).
- [30] G. Brandl, J. Krüger and E. Faulhaber, *NICOS: Flexibles Experimentieren an Großforschungsgeräten dank Python*, Talk. PyCon DE, Leipzig, Germany (2011).
- [31] G. Brandl, *MIEZE: Adding high energy resolution to magnetic small-angle scattering*, Talk. FRM-II User Meeting, Garching, Germany (2012).
- [32] G. Brandl, T. Weber, W. Häußler, S. Weichselbaumer, R. Georgii and P. Böni, *Monte-Carlo simulations for the optimization of a MIEZE spin-echo instrument at the ESS*, Poster. PNCMI, 2012, Paris, France (2012).
- [33] G. Brandl, *Time resolution of a MIEZE instrument*, Talk. MIEZE@ESS Satellite Meeting, PNCMI 2012, Paris, France (2012).
- [34] G. Brandl, M. Kugler, R. Georgii and P. Böni, *The new triple-axis option at MIRA and first measurements of the helimagnons in MnSi*, Invited Talk. G-A1 Group Seminar, Helmholtz Zentrum Berlin, Germany (2012).
- [35] H. Ceeh, J. Weber, C. Hugenschmidt and P. Böni, *Determination of the electronic structure using positrons*, Poster. TRR80 Retreat Meeting, Freising, Germany (2011).
- [36] H. Ceeh, *A new 2D-ACAR spectrometer at the NEPOMUC positron facility*, Poster. PSD11, Delft, Netherlands (2011).
- [37] H. Ceeh, M. Leitner, J. Weber, C. Hugenschmidt and P. Böni, *Determination of the electronic structure using positrons*, Poster. International Workshop Functionality from Heterostructures, Obergurgl, Austria (2011).
- [38] H. Ceeh, *First 2D-ACAR measurements on Fe<sub>2</sub>TiSn*, Talk. ACIT Workshop, Augsburg, Germany (2011).
- [39] H. Ceeh, *Positron Physics at the FRM II*, Talk. Young Neutron Researcher Seminar, Garching, Germany (2011).
- [40] H. Ceeh, *Positron Physics at NEPOMUC*, Talk. Young Neutron Researcher Seminar, Garching, Germany (2011).
- [41] H. Ceeh, *Experimental Search for Dark Matter*, Talk. TRR80 Young Researcher Workshop, Kleinwiesertal, Austria (2011).

- [42] H. Ceeh, *First measurements on Cr with the new 2D-ACAR spectrometer at NEPOMUC*, Talk. *ICPA16, Bristol, UK* (2012).
- [43] H. Ceeh, *Temperature dependent 2D-ACAR measurements on Cr*, Talk. *TRR80 Summer School, Frauenchiemsee, Germany* (2012).
- [44] S. Dunsiger, *Coupled Vibrational and Magnetic Response in Multiferroic Perovskites*, Oral Presentation. Neutronen in Forschung und Industrie, Garching, Germany (2011).
- [45] S. Dunsiger, *Investigation of Ferromagnetic Semiconductors through Depth Resolved Spin Resonance Techniques*, Invited Seminar. Karlsruher Institut für Technologie (KIT), Physikalisches Institut, Karlsruhe, Germany (2011).
- [46] S. Dunsiger, *Melting Spin Ice*, Oral Presentation. Korrelationstage 2011, Max-Planck-Institut für Physik komplexer Systeme, Dresden, Germany (2011).
- [47] S. Dunsiger, *Melting Spin Ice*, Invited Oral Presentation. 2nd Advanced Science Research Center International Workshop on Magnetic Materials and Nanostructures, Tokai, Japan (2012).
- [48] S. Dunsiger, *Spin Liquid and Spin Ice*, Invited Seminar. Royal Holloway, University of London, UK (2012).
- [49] S. Dunsiger, *Spin Liquid and Spin Ice*, Invited Seminar. Oxford University, UK (2012).
- [50] S. Dunsiger, *Melting Spin Ice*, Invited Oral Presentation. The International Conference on Highly Frustrated Magnetism 2012, Hamilton, USA (2012).
- [51] S. Dunsiger, *Melting Spin Ice*, Invited Oral Presentation. The 19th International Conference on Magnetism with Strongly Correlated Electron Systems, Busan, Korea (2012).
- [52] S. Dunsiger, *Spin Liquid and Spin Ice*, Invited Oral Presentation. Plenary session of the 4th Joint Meeting of the International Conference on Hyperfine Interactions and the International Symposium on Nuclear Quadrupole Interactions (HFI/NQI 2012), Beijing, China (2012).
- [53] K. Everschor-Sitte, *Current-Induced Dynamics of Chiral Magnetic Structures; Skyrmions, Emergent Electrodynamics and Spin-Transfer Torques*, Talk. Science Master Class with Prof. Albert Fert at the 62nd Lindau Nobel Laureate Meeting (Physics), Lindau, Germany (2012).
- [54] K. Everschor-Sitte, *Rotating skyrmion lattices by spin torques and field or temperature gradients*, Invited Talk. 520. Wilhelm und Else Heraeus Seminar, Physikzentrum Bad Honnef, Germany (2012).
- [55] C. Franz, A. Regnat, A. Bauer, S. Gottlieb-Schönmeyer, K. Mittermüller and C. Pfeleiderer, *Single Crystal Properties of non-centrosymmetric CeAuAl<sub>3</sub>*, Poster. Cambridge, UK (2011).
- [56] R. Georgii, W. Häußler, G. Brandl, N. Martin, S. Dunsiger and P. Böni, *The scientific case for a MIEZE-NRSE Spectrometer at the ESS*, Poster. ESS Science & Scientists Meeting, Berlin, Germany (2012).
- [57] W. Häußler, G. Brandl, R. Georgii, T. Weber, S. Weichselbaumer and P. Böni, *A MIEZE-NRSE Spectrometer for the ESS*, Poster. ESS Science & Scientists Meeting, Berlin, Germany (2012).
- [58] C. Hugenschmidt, *Positrons Probing Matter – Novel Applications of the Low-Energy High-Intensity Positron Beam at NEPOMUC*, Invited Talk. Physikalisches Kolloquium, Technische Universität und Karl-Franzens Universität Graz, Austria (2011).
- [59] C. Hugenschmidt, *Surface Segregation of Cu in Pd studied by Time-Resolved Positron-Annihilation-Induced Auger Electron Spectroscopy*, Invited Talk. PSD-11, 11th International Workshop on Positron Studies of Defects 2011, Delft University of Technology, Delft, Netherlands (2011).
- [60] C. Hugenschmidt, *Positron Beam Experiments at NEPOMUC and Time-Dependent PAES*, Invited Talk. PPC-10, 10th International Workshop on Positron and Positronium Chemistry, Smolenice, Slovakia (2011).
- [61] C. Hugenschmidt, *Positrons Probing Matter: Bulk and Thin Film Studies Using the Low-Energy Positron Beam at NEPOMUC*, Invited Talk. Frühjahrstagung der Deutschen Physikalischen Gesellschaft, Berlin, Germany (2012).
- [62] C. Hugenschmidt, *The Upgrade of the Positron Source NEPOMUC and Advanced Positron Beam Studies of Surfaces and Thin Films*, Invited Talk. ICPA-16, The XVIth International Conference on Positron Annihilation, Bristol, UK (2012).

- [63] C. Hugenschmidt, *Strahlen aus Antiteilchen: Was macht das Positron in Materie*, Talk. Café & Kosmos, Munich, Germany (2012).
- [64] J. Kindervater, W. Häußler, A. Tischendorf and P. Böni, *Neutron Spin Echo from Polarizing Samples*, Poster. European Conference On Neutron Scattering, Prague, Czech Republic (2011).
- [65] J. Kindervater, W. Häußler, A. Tischendorf, C. Pfeiderer and P. Böni, *Helimagnets studied with NSE at RESEDA*, Poster. Frühjahrstagung der Deutschen Physikalischen Gesellschaft, Berlin, Germany (2011).
- [66] J. Kindervater, *Polarization analysis with MiniMuPAD: Investigation of a fluctuation induced first-order transition*, Talk. Polarised Neutrons in Condensed Matter Investigations, Paris, France (2012).
- [67] C. Krey, *Vibrating Coil Magnetometry of the Spin Ice State in  $\text{Ho}_2\text{Ti}_2\text{O}_7$  at mK-Temperatures*, Talk. Frühjahrstagung der Deutschen Physikalischen Gesellschaft, Dresden, Germany (2011).
- [68] C. Krey, *On-Chip Refrigeration at sub-Kelvin Temperatures*, Talk. TRR80 Young Researcher Workshop, Kleinwiesertal, Austria (2011).
- [69] C. Krey, *Vibrating Coil Magnetometry of the Spin Ice State in  $\text{Ho}_2\text{Ti}_2\text{O}_7$* , Poster. TRR80 Retreat Meeting, Freising, Germany (2011).
- [70] C. Krey, *Vibrating Coil Magnetometry of the Spin Ice State in  $\text{Ho}_2\text{Ti}_2\text{O}_7$* , Poster. Cambridge University, UK (2011).
- [71] C. Krey, *Search for quantum spin ice in  $\text{Tb}_2\text{Ti}_2\text{O}_7$  at milli-Kelvin temperatures*, Talk. Frühjahrstagung der Deutschen Physikalischen Gesellschaft, Berlin, Germany (2012).
- [72] S. Mühlbauer, C. Pfeiderer, P. Böni, T. Adams, F. Jonietz, A. Bauer, E. M. Forgan, U. Keiderling, E. H. Brandt and A. Wiedemann, *Time Resolved Stroboscopic Small Angle Neutron Scattering and TIS-ANA on Vortex Lattices in Superconductors and Skyrmion Lattices in Chiral Magnets*, Talk. SAS12, 15th International Small Angle Scattering Conference 2012, Sydney, Australia (2012).
- [73] A. Paul, *Division of Superconductivity and Magnetism*, Seminar. Institute for Experimental Physics II University of Leipzig, Leipzig, Germany (2011).
- [74] A. Paul, *Polarized neutron scattering in magnetic nano-layered systems*, Physik-Kolloquium. Fachbereich Physik der Freien Univ. Berlin, Berlin, Germany (2011).
- [75] A. Paul, *Polarized neutron scattering in magnetic nano-layered systems*, Physik-Kolloquium. Forschungszentrum Dresden-Rossendorf, Dresden, Germany (2011).
- [76] A. Paul, *Polarized neutron scattering in magnetic nano-layered systems*, Experimentalphysik/Festkörperphysik Seminar. Ruhr-Universitaet, Bochum, Germany (2011).
- [77] A. Paul, *Polarized neutron scattering in magnetic nano-layered systems*, E21 Experimentalphysik Seminar. Technische Universitaet München, Garching, Germany (2011).
- [78] A. Paul, *Polarized neutron scattering in magnetic nano-layered systems*, Invited talk. Synchrotron Light Research Institute, Nakhon Ratchasima, Thailand (2011).
- [79] A. Paul, *Polarized neutron scattering in magnetic nano-layered systems*, Invited talk. Bhabha Atomic Research Centre, Solid state Physics Division, Mumbai, India (2011).
- [80] A. Paul, *Polarized neutron scattering in magnetic nano-layered systems*, Invited talk. Indian Institute of Technology Delhi, Physics Department, Delhi, India (2011).
- [81] A. Paul, *Polarized neutron scattering in magnetic nano-layered systems*, Invited talk. Indian Institute of Technology Kanpur, Physics Department, Kanpur, India (2011).
- [82] A. Paul, *Domain structure correlation for non-collinear, out-of-plane Exchange coupled system by polarized neutron scattering*, Oral presentation. ESS Workshop "Science Vision for the European Spallation Source", Bad Reichenhall, Germany (2011).
- [83] A. Paul, *Vertical correlation of domains due to non-collinear and out-of-plane exchange-coupling*, Oral presentation. 4th FRM2 user meeting, Graching bei München, Germany (2012).
- [84] A. Paul, *Correlation of domains in exchange-coupled systems*, Invited talk. Workshop on New Opportunities for Research on Hard and Soft Matter Nanostructures using Neutron Reflectometry, Berlin, Germany (2012).

- [85] A. Paul, *Low angle polarized neutron scattering from nano-layered systems*, Vorstellungsvortrag zur Habilitation. Technische Universität München, Garching, Germany (2012).
- [86] C. Pfeleiderer, *Topological Insulator in a Heusler Compound*, Talk. 3. TUM Nanomagnetik-Workshop, Technische Universität München, Garching, Germany (2011).
- [87] C. Pfeleiderer, *Skyrmions – an emergent phenomenon in condensed matter systems*, Invited Talk. 22. Edgar-Lüscher Seminar, Klosters, Switzerland (2011).
- [88] C. Pfeleiderer, *Spin transfer torques in MnSi at Ultra-low Current Densities*, Invited Talk. Korrelationstage 2011, Max Planck Institut für komplexe Systeme, Dresden, Germany (2011).
- [89] C. Pfeleiderer, *Higher-order scattering in the skyrmion lattice of MnSi*, Talk. Frühjahrstagung der Deutschen Physikalischen Gesellschaft, Dresden, Germany (2011).
- [90] C. Pfeleiderer, *Skyrmion Lattices in Chiral Magnets*, Invited Talk. March Meeting of the American Physical Society, Dallas, USA (2011).
- [91] C. Pfeleiderer, *Larmor Diffraction under Extreme Conditions*, Invited Talk. Present Status and Perspectives of Neutron Research in High Magnetic Fields (Workshop), HMI Berlin, Germany (2011).
- [92] C. Pfeleiderer, *Topological Spin Solitons in Chiral Magnets*, Colloquium. Physikalisches Kolloquium, Universität Konstanz, Germany (2011).
- [93] C. Pfeleiderer, *Topological Spin Solitons in Chiral Magnets*, Invited Talk. European Conference on Neutron Scattering, Prague, Czech Republic (2011).
- [94] C. Pfeleiderer, S. Dunsiger, T. Adams, A. Bauer, C. Franz, C. Krey, A. Regnat, R. Ritz and M. Wagner, *Magnetische Materialien für neue technische Anwendungen*, Poster. Tag der Physik, Garching, Germany (2011).
- [95] C. Pfeleiderer, *Topological Phases and Spin Torque Effects in Chiral Magnets*, Invited Talk. International Conference on Strongly Correlated Electron Systems, University of Cambridge, UK (2011).
- [96] C. Pfeleiderer, *Topological Phases and Spin Torque Effects in Chiral Magnets*, Invited Talk. Workshop on Topological Materials, Institute Laue Langevin, Grenoble, France (2011).
- [97] C. Pfeleiderer, *Emergent Electrodynamics of Skyrmions in Chiral Magnets*, Invited Talk. First QS2C Workshop on Emergent Phenomena in Correlated Materials, Okinawa, Japan (2011).
- [98] C. Pfeleiderer, *Spin-Transfer Torques at Ultralow Current Densities*, Invited Talk (Presentation by Skype). ASRC Workshop, Tokai, Japan (2012).
- [99] C. Pfeleiderer, *Emergent Electrodynamics of Skyrmions in Chiral Magnets*, Invited Talk. Physikalisches Kolloquium, Universität Braunschweig, Germany (2012).
- [100] C. Pfeleiderer, *Topologische Eigenschaften stark korrelierter Elektronensysteme*, Talk. Universität Augsburg, Germany (2012).
- [101] C. Pfeleiderer, *Emergent Electrodynamics of Skyrmions in Chiral Magnets*, Invited Talk. Magnetic Small Nano Workshop 2012, Les Houches, France (2012).
- [102] C. Pfeleiderer, *Emergent Electrodynamics of Skyrmions in Chiral Magnets*, Invited Talk. Frühjahrstagung der Deutschen Physikalischen Gesellschaft, Berlin, Germany (2012).
- [103] C. Pfeleiderer, *Emergent Electrodynamics of Skyrmions in Chiral Magnets*, Invited Talk. Sino-German Bilateral Workshop on Emergent Phases in Correlated and Topological Matter, Zhejiang University, Hangzhou, China (2012).
- [104] C. Pfeleiderer, *Topologische Eigenschaften stark korrelierter Elektronensysteme*, Talk. Karlsruhe Institute for Technology, Germany (2012).
- [105] C. Pfeleiderer, *Emergent Electrodynamics of Chiral Magnets*, Invited Talk. General Assembly of the Institute of Advanced Study, Technische Universität München, Schloss Hohenkammer, Germany (2012).
- [106] C. Pfeleiderer, *Emergent Electrodynamics of Skyrmions in Chiral Magnets*, Invited Talk. International Symposium on the Dynamics of Domain Walls 2012, Universität Hamburg, Germany (2012).

- [107] C. Pfeleiderer, *Emergent Electrodynamics of Skyrmions in Chiral Magnets*, Presentation. International Conference on Highly Frustrated Magnetism 2012, McMaster University, Hamilton, Canada (2012).
- [108] C. Pfeleiderer, *Condensed Matter Particle Physics (Teilchenphysik im Festkörper)*, Ringvorlesung. Technische Universität München, Garching, Germany (2012).
- [109] C. Pfeleiderer, *Emergent Electrodynamics of Skyrmions in Chiral Magnets*, Invited Talk. Workshop on Micromagnetic Theory and SANS, Technische Universität München, Garching, Germany (2012).
- [110] C. Pfeleiderer, *Emergent Phenomena in Complex Electronic Materials*, Presentation. Deutsche Neutronentagung 2012, Bonn, Germany (2012).
- [111] C. Pfeleiderer, *Incipient Ferromagnetic Quantum Criticality in the Zero-Gap Semiconductor  $Fe_2TiSn$* , Talk. MPI CPfS, Dresden, Germany (2012).
- [112] C. Pfeleiderer, *Emergent Electrodynamics of Skyrmions in Chiral Magnets*, Invited Talk. Conference on Exotic Phases of Frustrated Magnets, KITP, Santa Barbara, USA (2012).
- [113] M. Rahn, T. Adams, G. Brandl, J.Repper, P. Böni, C. Pfeleiderer and R. Georgii, *Testing the Practicability of Elliptic Neutron Focusing*, Talk. TRR80 Summer School, Frauenchiemsee, Germany (2012).
- [114] M. Reiner, *Depth resolved Doppler broadening spectroscopy in thin metallic films*, Talk. Frühjahrstagung der Deutschen Physikalischen Gesellschaft, Dresden, Germany (2011).
- [115] M. Reiner, *Annealing of thin metallic films studied by depth dependent DB-spectroscopy and the investigation of Ps annihilation*, Talk. Workshop Ionen- und Positronenstrahlen, Neubiberg, Germany (2011).
- [116] M. Reiner, *Studies on the annealing of thin metallic films by depth dependent DB-spectroscopy and the investigation of Ps annihilation*, Talk. PSD-11, Delft, Netherlands (2011).
- [117] M. Reiner, *Interdiffusion in Au/Cu thin films studied by depth dependent CDBS*, Talk. Frühjahrstagung der Deutschen Physikalischen Gesellschaft, Berlin, Germany (2012).
- [118] M. Reiner, *Interdiffusion at an Au-Cu interface studied by depth dependent and in-situ CDBS*, Talk. ICPA-16, The XVIth International Conference on Positron Annihilation, Bristol, UK (2012).
- [119] R. Ritz, *Piston-Cylinder-Cells for Magnetization, Transport and Neutron Scattering*, Contributed Talk. High Pressure Experiments at FRM II: Future Perspectives and Developments, Munich, Germany (2011).
- [120] R. Ritz, *Larmor Diffraction on the Ferromagnetic Superconductor  $UGe_2$* , Contributed Talk. Frühjahrstagung der Deutschen Physikalischen Gesellschaft, Dresden, Germany (2011).
- [121] R. Ritz, *Emergent electrodynamics of skyrmions in a chiral magnet*, Contributed Talk. 4. TUM Nanomagnetik-Workshop, Munich, Germany (2012).
- [122] R. Ritz, *Emergent electrodynamics of skyrmions in a chiral magnet*, Invited Talk. March Meeting of the American Physical Society, Boston, USA (2012).
- [123] R. Ritz, *Pressure dependence of the topological Hall effect in  $MnSi$* , Contributed Talk. Frühjahrstagung der Deutschen Physikalischen Gesellschaft, Berlin, Germany (2012).
- [124] W. Schirmacher, A. Omran, L. Schulz, S. Valloppilly, P. Böni, W. Petry and P. Müller-Buschbaum, *Magnetoelastic effects of magnetic nanoparticles in a copolymer matrix*, Poster. Frühjahrstagung der Deutschen Physikalischen Gesellschaft, Dresden, Germany (2011).
- [125] P. Schmakat, *Neutron Depolarization Imaging: Low Temperature Study on the Kondo-Cluster-Glass  $CePd_{1-x}Rh_x$* , Talk. Frühjahrstagung der Deutschen Physikalischen Gesellschaft, Dresden, Germany (2011).
- [126] P. Schmakat, *Manipulation of the neutron polarisation at the spin echo spectrometer RESEDA*, Talk. ECNS, Prague, Czech Republic (2011).
- [127] P. Schmakat, *Neutron Depolarization Imaging: Low Temperature Study of the Kondo-Cluster-Glass Formation in  $CePd_{1-x}Rh_x$* , Talk. FOR960 Meeting, Karlsruhe, Germany (2011).
- [128] P. Schmakat, *Neutron Depolarization Imaging: Low Temperature Study of the Kondo-Cluster-Glass Formation in  $CePd_{1-x}Rh_x$* , Talk. FRM II User Meeting, Munich, Germany (2011).

- [129] P. Schmakat, *Neutron Depolarization Imaging: Low Temperature Study of the Kondo-System  $CePd_{1-x}Rh_x$* , Talk. SCES, Cambridge, UK (2011).
- [130] P. Schmakat, *A Chopper System for the Imaging Beamline at the European Spallation Source*, Talk. IKON 2, Malmö, Sweden (2012).
- [131] P. Schmakat, *Polarisation Analysis at POLI-HEIDI: Magnetic Anisotropy of the Kondo Lattice  $CePd_{1-x}Rh_x$* , Talk. Frühjahrstagung der Deutschen Physikalischen Gesellschaft, Berlin, Germany (2012).
- [132] P. Schmakat, *Wavelength Frame Multiplication Chopper System for the Multi-Purpose Imaging Beamline at the ESS*, Talk. ESS Science Symposium, Berlin, Germany (2012).
- [133] P. Schmakat, *Polarisation Analysis at POLI-HEIDI: Magnetic Anisotropy of the Kondo Lattice  $CePd_{1-x}Rh_x$* , Talk. FRM II User Meeting, Munich, Germany (2012).
- [134] P. Schmakat, *Neutron Depolarization Imaging: Low Temperature Study of the Kondo-System  $CePd_{1-x}Rh_x$* , Talk. NIUS, Bad Zurzach, Switzerland (2012).
- [135] P. Schmakat, *Neutron Depolarisation Imaging of the Kondo-Cluster-Glass formation in  $CePd_{1-x}Rh_x$* , Talk. FRM II Neutronen-Seminar, Munich, Germany (2012).
- [136] P. Schmakat, *Wavelength Frame Multiplication Chopper System for the Multi-Purpose Imaging Beamline at the ESS*, Talk. IKON 3, Lund, Sweden (2012).
- [137] A. Schmeh, T. Mairoser, A. Melville, T. Heeg, L. Canella, P. Böni, W. Zahnder, J. Schubert, D. E. Shai, E. J. Monkman, K. M. Shen, D. G. Schlom and J. Mannhart, *Curie temperature of electron doped  $EuO$  - is there an intrinsic limit?*, Talk. APS March Meeting, Dallas, USA (2011).
- [138] M. Schneider, T. Panzner, Y. Bodenthin, U. Filges, J. Stahn, C. Schanzer, M. Kenzelmann and P. Böni, *Adaptive Optics for Neutrons*, Poster. ECNS'2011, Prague, Czech Republic (2011).
- [139] K. Schreckenbach, *How precisely do we know the reactor antineutrino spectra?*, Invited Talk. Beyond3Nu, Grand Sasso Laboratory, Italy (2011).
- [140] K. Schreckenbach, *Cumulated beta spectrum measurements of fission products at ILL and FRM II*, Invited Talk. SNAC 11, Virginia Tech, USA (2011).
- [141] K. Schreckenbach, *Monte Carlo Methoden*, Talk. Ausbildungsseminar Reaktorbetrieb FRM II (2011).
- [142] K. Schreckenbach, *Wie und Warum: Planung, Bau und nukleare Inbetriebsetzung des FRM II*, Talk. Ausbildungsseminar Reaktorbetrieb FRM II (2012).
- [143] M. Schulz, *Quantum Criticality: Radiography with Polarised Neutrons*, Talk. European Conference on Neutron Scattering, Prague, Czech Republic (2011).
- [144] M. Schulz, *Quantum Criticality: Radiography with Polarised Neutrons*, Talk. TIPSII Workshop, Sønderborg, Denmark (2011).
- [145] M. Schulz, *Imaging with Polarized Neutrons*, Invited Talk. PSI, ASQ-Seminar, Villigen, Switzerland (2011).
- [146] M. Schulz, *ANTARES Upgrade*, Invited Talk. Neutron Imaging User Symposium, Bad Zurzach, Switzerland (2012).
- [147] M. Schulz, *A Chopper Concept for the Imaging Beam Line at ESS*, Invited Talk. International Topical Meetin on Neutron Radiography, Kingston, Canada (2012).
- [148] M. Schulz, *Neutron Depolarisation Imaging of the Kondo-Cluster-Glass formation in  $CePd_{1-x}Rh_x$* , Invited Talk. International Topical Meetin on Neutron Radiography, Kingston, Canada (2012).
- [149] M. Wagner, *Incipient quantum criticality in single-crystal  $Fe_2TiSn$* , Talk. Frühjahrstagung der Deutschen Physikalischen Gesellschaft, Dresden, Germany (2011).
- [150] M. Wagner, *Incipient Quantum Criticality in Zero-Gap Semiconductor  $Fe_2TiSn$* , Talk. SCES, Cambridge, UK (2011).
- [151] M. Wagner, *Experimental signatures of a topological insulator in a Heusler compound*, Talk. Institutsseminar MPI FKF, Stuttgart, Germany (2011).

- [152] M. Wagner, *Incipient Quantum Criticality in Zero-Gap Semiconductor  $Fe_2TiSn$* , Poster. International Workshop Functionality from Heterostructures, Obergurgl, Austria (2011).
- [153] M. Wagner, *Experimental Signatures of a Topological Insulator in a Heusler compound*, Poster. TRR Retreat Meeting Freising, Germany (2011).
- [154] M. Wagner, *Search for topological spin order in the multiferroic insulator  $Cu_2OSeO_3$* , Poster. ICM Busan, Korea (2012), Best Poster Award.
- [155] J. A. Weber, *A New 2D-ACAR Spectrometer at the NEPOMUC Positron Facility*, Poster. International Workshop Functionality from Heterostructures, Obergurgl, Austria (2011).
- [156] J. A. Weber, *ACAR Data Processing - From Measurement to Fermi Surface*, Presentation. Retreat Meeting, TRR 80, Freising, Germany (2012).
- [157] J. A. Weber, *2D-ACAR measurement on  $Fe_2TiSn$* , Poster. ICPA-16, The XVIth International Conference on Positron Annihilation, Bristol, UK (2012).
- [158] J. A. Weber, *2D-ACAR measurement on  $Fe_2TiSn$* , Poster. TRR80 Summer School, Frauenchiemsee, Germany (2012).
- [159] B. Wiedemann, A. Bauer, J. Weber, J. Kindervater and P. Schmakat, *Vorstellung E21*, Talk. E21 Doktorandenseminar, Garching, Germany (2012).

## Seminar “Neutronen in Industrie und Forschung” 2011

Date	Title	Speaker
10-01-2011	Coupled Vibrational and Magnetic Response in Multiferroic Perovskites	Dr. S. R. Dunsiger
17-01-2011	Structure and dynamics of biomacromolecules in solution: recent developments and future perspectives in SANS/SAXS and neutron spectroscopy	Dr. F. Gabel
24-01-2011	Neutron Spin Echo on MnSi	A. Tischendorf
31-01-2011	Flagship experiments at the ESS	K. Lomachenko
07-02-2011	Swygenhoven-Moens Radiation Biology and the Linear-Quadratic Model	S. Huber
14-02-2011	Micromechanics and Microstructures - X-rays, Neutrons and Computation	Prof. Dr. H. Van
02-05-2011	Vorbesprechung für das Sommersemester 2011	Dr. W. Häußler
09-05-2011	In operando neutron scattering studies on Li-ion batteries	Dr. A. Senyshyn
14-05-2011	Diffusion and Point Defects in Solids – Experiments with Neutron and X-ray Reflectometry	Prof. Dr. H. Schmidt
16-05-2011	Getting to grips with the short-time dynamics of cell membrane models	S. Busch
23-05-2011	Ultra-Cold Neutrons at the FRM II – Current Status and Recent Developments	Dr. A. Frei
30-05-2011	ISAGE - a lunar mission with In-Situ-NAA	Dr. X. Li
20-06-2011	The multiple dimensions of PGAA measurements	Dr. L. Canella
27-06-2011	Vibrational Properties of NiMnGa Ferromagnetic Shape Memory Alloys	S. Ener
04-07-2011	Searching for theta13 with reactor neutrinos	Dr. M. Göger
11-07-2011	McStas Simulationen für RESEDA	L. Kredler
25-07-2011	Magnetism in MPS_3 (M=Mn, Fe, Co, Ni), a family of quasi-two dimensional antiferromagnets	Dr. A. Wildes
26-09-2011	Mammoths and Meteorites	Dr. R. B. Firestone
17-10-2011	Vorbesprechung für das Wintersemester 2011/2012	Dr. W. Häußler
24-10-2011	Auf dem Weg zu hochdichten Uranbrennstoffen für Forschungsreaktoren I, Metallurgie hochdichter UMo Brennstoffe unter Bestrahlung	R. Jungwirth
07-11-2011	Evolution of U-Mo fuel design and fabrication	W. Schmid
14-11-2011	Magnetic excitations in superlattices and a thin film of rare-earths measured with neutron three-axis-spectroscopy	Dr. A. Grünwald
21-11-2011	Dynamics in interstitial and complex hydrides	Dr. A. Borgschulte
28-11-2011	Long-range crystalline nature of the skyrmion lattice in MnSi	T. Adams
05-12-2011	Search for neutrinoless double beta decay of Ge-76 with the GERmaniumDetector Array “GERDA”	Dr. J. Janicsko
19-12-2011	Bound Beta-Decay: BOB	Dr. J. McAndrew

## Seminar “Neutronen in Industrie und Forschung” 2012

Date	Title	Speaker
09-01-2012	Combining small-angle scattering of neutrons and X-rays to determine the low-resolution structure of membrane proteins	Prof. L. Arleth
16-01-2012	Quasicrystal dynamics: phonons and phasons	Dr. M. de Boissieu
23-01-2012	Precision Measurements of Neutron Decay Correlation Coefficients with Perkeo III and PERC	Dr. B. Märkisch
30-01-2012	Depth Resolved Dynamics Studied with NSE under Grazing Incidence: Surface Influence on Membrane Fluctuations	Dr. O. Holderer
06-02-2012	New $\gamma$ -Beams, New $\gamma$ -Optics, New Secondary Beams: Neutrons, Positrons, Neutrinos	Prof. D. Habs
13-02-2012	Neutron imaging in materials research	Dr. N. Kardjilov
12-03-2012	Concept for a reflectometer using focusing guides	Dr. J. Stahn
23-04-2012	Vorbereitung für das Sommersemester 2012	Dr. W. Häußler
07-05-2012	NRSE & MIEZE at ESS: Status	Dr. W. Häußler
14-05-2012	Diffusion and Point Defects in Solids – Experiments with Neutron and X-ray Reflectometry	Prof. Dr. H. Schmidt
21-05-2012	Expansion of Research Facilities at the NIST Center for Neutron Research	Dr. R. M. Lindstrom
02-06-2012	Thermal properties of reactor fuel with lower enrichment	T. Huber
04-06-2012	Commissioning of the CASCADE detector at MIRA	K. Kahl
11-06-2012	Structural and dynamic study of several magnetic systems by means of Neutron Resonant Spin Echo techniques	N. Martin
18-06-2012	Macromolecular crystallography at the European Spallation Source	Dr. E. Oksanen
25-06-2012	Neutron depolarisation imaging of kondo cluster glasses in weak magnetic fields	P. Schmakat
11-07-2012	Dynamic nature of Proteins probed by X-ray and Neutron scattering	Dr. J. Lal
30-07-2012	Investigation of T-Odd Effects in Fission Induced by Polarized Neutrons	Dr. Yu. N. Kopatch
10-09-2012	Survey of Russian (Soviet) Research Reactors	Dr. D. Chubreev
15-10-2012	Vorbereitung für das Wintersemester 2012/2013	Dr. W. Häußler
22-10-2012	Quantum Criticality and Frustration	Dr. V. Fritsch
29-10-2012	Current R&D topics concerning fuel assembly and fuel rod design at EON Kernkraft	Dr. M. Seidl
05-11-2012	Neutronic design of the ESS target-moderator-reflector system	Dr. L. Zanini
12-11-2012	Niedrigdosenwirkung und Langzeitbetrachtung	S. Oswald
19-11-2012	Detector requirements for the ESS and potential of the B-10 Multi-Grid detector for large-area applications	Dr. A. Khaplanov
26-11-2012	Boron-10 based detectors as an alternative for the He-3 tubes in large-area neutron detectors for neutron scattering applications	Dr. I. Stefanescu
03-12-2012	Molecular dynamics explored with slow neutrons and fast computers	H. Morhenn
10-12-2012	What S(q) can do for you	Dr. H. Fischer
17-12-2012	POWTEX - High-Intensity Neutron TOF Diffractometer	Dr. A. Houben

## Services to the Community

### Peter Böni

- Member of the TUM-Advisory Board for the FRM-II, Garching, Germany.
- Vice-Chairman of the ESS Scientific Advisory Committee (ESS-SAC) of the European Spallation Source ESS, Lund, Sweden.
- Chairman of the ESS Scientific Advisory Committee for Instrumentation (ESS-iSAC) of the European Spallation Source ESS, Lund, Sweden.
- Associate Coordinator of the Transregio TRR 80, Augsburg/Munich/Stuttgart, Germany.
- Member of the Scientific and Technical Advisory Panel (STAP) for Imaging, European Spallation Source ESS, Lund, Sweden.
- Member of the Executive Programme Committee for ICNS2013, Edinburgh, UK.
- Chairman of the JCNS Proposal Selection Panel for Hard Condensed Matter 2011/2012, Garching, Germany.
- Member of the International Advisory Committee for the Workshop on Neutron Optics and Detectors NOP&D-2013, Ismaning, Germany.
- Member of the International Advisory Committee for the Workshop on Polarized Neutrons for Condensed Matter Investigations (PNCMI) 2012, Paris, France.
- Member of the Praktikumskommission at the Physik-Department, Technische Universität München, Garching, Germany.
- Vertrauensdozent of the Crystal Laboratory at the Physik-Department, Technische Universität München, Garching, Germany.

### Christian Pfeiderer

- Associate Member of Commission C5 in Commission C9 (Magnetism) of the International Union for Pure and Applied Physics (IUPAP), since 10/2012
- German Representative in Commission C5 (Low Temperatures) of the International Union for Pure and Applied Physics (IUPAP), since 05/2012
- Member of the Beam Time Committee, SINQ, Paul-Scherer Institut, since 2011
- Member of the Scientific Advisory Council, European Spallation Source, Lund, Sweden, since 2010
- Founding Member of the Scientific Advisory Panel, Nature Communications, since 03/2010
- Deputy Chair, Komitee Forschung für Neutronen (KFN), 2008-2011
- Member of Beam Time Committee, Jülich Center for Neutron Science, 2008-2011
- Vertrauensdozent of the Studienstiftung des deutschen Volkes, since 2007
- Founding Member of the Steering Committee of DFG-TR80, since 2009
- Head of the Board of the Further Training Unit of DFG-TR80, since 2009
- Member of the International Advisory Committee for the International Conference on Strongly Correlated Electron Systems in Cambridge, UK, September 2011.
- Member of the International Advisory Committee for the International Conference on Strongly Correlated Electron Systems in Tokyo, Japan, August 2013.
- Chairman of the MSc Prüfungsausschuss at the Physik-Department, Technische Universität München, Garching, Germany, since 2010.
- Vice-Chairman of the BSc Prüfungsausschuss at the Physik-Department, Technische Universität München, Garching, Germany, since 2010.
- Spokesman of the Fachbereich kondensierte Materie at the Physik-Department, Technische Universität München, Garching, Germany, since 10/2012.
- Schriftführer des Vereins der Freunde der Physik, e.V., since 2010.
- Member of the Department Advisory Board at the Physik-Department, Technische Universität München, Garching, Germany, since 10/2010.

## Accomplished Ph.D. Theses

<b>Ralph Bundschuh</b>	Improving Quantification in Combined Positron Emission and Computed Tomography in Oncology
<b>Melanie Hohberg</b>	Monte Carlo Simulation Studies and Image Reconstruction Methods for a Small Animal PET Scanner
<b>Florian Jonietz</b>	Spin Transfer Torques and Spin Fluctuations in Helimagnets
<b>Karsten Schörner</b>	Development of Methods for Scatter Artifact Correction in Industrial X-ray Cone-beam Computed Tomography

## Accomplished Master's and Diploma Theses

<b>Ralitsa Bozhanova</b>	Single Crystal Growth Of f-Electron Compounds with Unusual Low Temperature Properties (2012)
<b>Alfonso Chacon</b>	Neutron Scattering and Susceptibility Studies of Skyrmion Lattices under Uniaxial Pressure (2011)
<b>Marco Halder</b>	Präzisionsmessung der Magnetisierung an Systemen mit komplexer Ordnung (2012)
<b>Maximilian Hirschberger</b>	Transverse Ising Quantum Phase Transitions in $Nb_{1-y}Fe_{2+y}$ (2011)
<b>Jonas Kindervater</b>	From Heli- to Paramagnetism in MnSi: Polarization Analysis with MiniMuPAD
<b>Ralf Korntner</b>	Suche nach topologischen Effekten in intermetallischen Verbindungen (2011)
<b>Christopher Krey</b>	Spulen-Vibrationsmagnetometrie an frustrierten Magneten bei mK-Temperaturen (2011)
<b>Kilian Mittermueller</b>	Tieftemperatur-Röntgenpulverdiffraktometrie von komplexen metallischen Verbindungen (2011)
<b>Markus Reiner</b>	Depth resolved Doppler broadening spectroscopy of thin metallic films with a mono energetic positron beam
<b>Philipp Schmakat</b>	Neutronen-Depolarisationsmessungen am Kondo-System $CePd_{1-x}Rh_x$ bei tiefen Temperaturen
<b>Christoph Schnarr</b>	Spin Transfer Torque Effekte in chiralen Magneten (2012)
<b>Tomek Schulz</b>	Untersuchung von Spin-Torque-Effekten in chiralen Magneten (2011)
<b>Tobias Weber</b>	MIEZE in Theory, Simulation and Experiment (2012)

## Accomplished Bachelor's Theses

<b>Julia Frisch</b>	Monte-Carlo-Simulationen für die Optimierung fokussierender Neutronenleiter (2011)
<b>Christian Fuchs</b>	Fertigungskonstruktion und FEM-Simulationen einer Hochfrequenzspule (Hochschule München, 2012)
<b>Karina Kahl</b>	Charakterisierung eines Cascade-Detectors am MIRA, FRM II
<b>Fabian Koessel</b>	Vielseitiges Miniatur-AC-Suszeptometer für Anisotropiestudien bei sehr tiefen Temperaturen (2011)
<b>Lukas Kredler</b>	Monte-Carlo simulations for RESEDA: The new CASCADE detector and planned extensions
<b>Martin Rutzinger</b>	Design und Charakterisierung eines Gas-Electron-Multiplier (GEM) Detektors zum orts aufgelösten Nachweis von 511 keV Gammastrahlung (2012)
<b>Jan Spallek</b>	Apparatur für kryogenfreie Experimente bei Temperaturen bis 1 mK (2011)

## Accomplished Term Papers

**Christian Fuchs**                      Konstruktion einer neuen HF-Spule für einen NRSE Flipper (Hochschule München, 2011)

## Accomplished Extended Essays / “Facharbeiten”

**Pascal Gehlert**                      How does temperature affect the magnetization (magnetic moment) of a neodymium magnet?

**Philipp Baur**                        Neutronenstrukturmessung von Glukosekristallen (Otto-von-Taubengymnasium, Gauting, 2011)

## Accomplished “Zulassungsarbeiten”

**Christoph Dollinger**                Drehmomentmagnetisierung von chiralen Magneten(2011)

**Katharina Lochner**                Thermische Leitfähigkeit itineranter Ferromagnete (2011)

**Dorothea Mallinger**                Differential-Thermoanalyse von Materialsystemen mit hohem Dampfdruck (2011)

## E21 Members

Phone/Fax prefix: +49-(0)89-289-

### Secretary

Name	Room	Phone	Fax	Email
Astrid Mühlberg	PH 1, 2211	14712	14713	astrid.muehlberg@frm2.tum.de

### Professors

Name	Room	Phone	Fax	Email
Prof. Dr. Peter Böni	PH 1, 2213	14711	14713	peter.boeni@frm2.tum.de
Prof. Dr. Christian Pfeiderer	PH 1, 2205	14720	14724	christian.pfeiderer@frm2.tum.de

### Scientists

Name	Room	Phone	Fax	Email
Dr. Sarah Dunsiger	PH 1, 2207	14722	14724	sarah.dunsiger@frm2.tum.de
Dr. Karin Everschor-Sitte		+49 (0)221 470-4212		karin.everschor@frm2.tum.de
Dr. Robert Georgii (FRM II)	UYH 0336	14986	14989	robert.georgii@frm2.tum.de
Dr. Alexander Grünwald	UYA 0342	10754	14620	alexander.gruenwald@frm2.tum.de
Dr. Wolfgang Häußler (FRM II)	UYH 0334	14921	14911	wolfgang.haeussler@frm2.tum.de
Dr. Christoph Hugenschmidt (FRM II)	Flachbau, 9	14609	14620	chugenschmidt@frm2.tum.de
Dr. Wolfgang Kreuzpaintner	PH 1, 2207	14740	14724	wolfgang.kreuzpaintner@frm2.tum.de
Dr. Anna Kusmartseva	PH1, 2201	12476	14724	anna.kusmartseva@frm2.tum.de
Dr. Nicolas Martin (FRM II)	RESEDA	14760	14911	nicolas.martin@frm2.tum.de
Dr. Christoph Morkel	PH 1, 2214	12157	14724	christoph.morkel@frm2.tum.de
Dr. Amitesh Paul	PH 1, 2203	14717	14724	amitesh.paul@frm2.tum.de
Dr. Christian Piochacz (FRM II)	NEPOMUC	12179	14620	christian.piochacz@frm2.tum.de
Dr. Burkhard Schillinger (FRM II)	RS 127	12185	13776	burkhard.schillinger@frm2.tum.de
Dr. Michael Schulz (FRM II)	UYA 0343	14718	13776	michael.schulz@frm2.tum.de
Dr. Klaus Seemann (FRM II)	UYH 0345	14668		klaus.seemann@frm2.tum.de

### PhD Students

Name	Room	Phone	Fax	Email
Tim Adams	PH1, 2373	12515	14724	tim.adams@frm2.tum.de
Andreas Bauer	PH 1, 2367	12512	14724	andreas.bauer@frm2.tum.de
Georg Brandl (FRM II)	UYA 0345	11754	14620	georg.brandl@frm2.tum.de
Alfonso Chacon	PH 1, 2367	12512	14724	alfonso.chacon@frm2.tum.de
Hubert Ceeh	UYD 0325	14568	14620	hubert.cee@frm2.tum.de
Christian Franz	PH 1, 2341	14515	14724	christian.franz@frm2.tum.de
Jonas Kindervater	PH 1, 2341	14253	14724	jonas.kindervater@frm2.tum.de
Marco Halder	PH 1, 2367	12512	14724	marco.halder@frm2.tum.de
Christopher Krey	PH 1, 2373	12515	14724	christopher.krey@frm2.tum.de
Osama Othman	UYA 0367	14641	14724	othman.osama@gmail.com
Philip Pikart	Flachbau, 10	12161	14620	philip.pikart@frm2.tum.de
Alexander Regnat	PH 1, 2341	14515	14724	alexander.regnat@frm2.tum.de
Markus Reiner	UYD 0325	11761	14620	markus.reiner@frm2.tum.de
Tommy Reimann	UYA 0345	11769		tommy.reimann@frm2.tum.de
Robert Ritz	PH 1, 2373	12515	14724	robert.ritz@frm2.tum.de
Benjamin Rohrmoser	RCM 107	13951	14347	benjamin.rohrmoser@radiochemie.de
Christina Schäffler	PH 1, 2367	14253	14724	christina.schaeffler@frm2.tum.de
Philipp Schmakat (FRM II)	BG 125a	12106	14724	philipp.schmakat@frm2.tum.de
Michael Schrapp	Siemens AG	089-63641065		michael.schrapp@siemens.com
Michael Wagner	PH 1, 2341	14515	14724	michael.wagner@frm2.tum.de
Josef-Andreas Weber	UYD 0325	14568	11760	josef-andreas.weber@frm2.tum.de
Birgit Wiedemann	PH 1, 2214	14725	14724	birgit.wiedemann@frm2.tum.de

## Students

Name	Room	Phone	Fax	Email
Georg Benka	PH1, 2341	14253	14724	georg.benka@frm2.tum.de
Marcel Brändlein	PH1, 2341	14515	14723	marcel.braedlein@frm2.tum.de
Martin Dehn	PH1, 2207	14722	14724	martin.dehn@frm2.tum.de
Stefan Doege	UCN Labor	14309		stefandoege@gmail.com
Elias Erdnüss	Flachbau	14631		elias.erdnuss@frm2.tum.de
Marlies Gangl	2201	12476		marlies.gangl@frm2.tum.de
Thomas Gigl	UYL 0235	14582	14620	thomas.gigl@frm2.tum.de
Frederik Görg	PH1, 2341	14515	14724	frederik.goerg@frm2.tum.de
Raphael Goll				
Max Kugler	UYA 0367	14515	14724	max.kugler@frm2.tum.de
Florian Lippert	UYL 0230	12129	14620	florian.lippert@frm2.tum.de
Sina Mayr	PH1, 2207	14740	14724	sina.mayr@frm2.tum.de
Saumya Mukherjee	PH 1, 2341	14515	14724	saumya.mukherjee@frm2.tum.de
Christoph Schnarr	PH1, 2341	14253	14724	christoph.schnarr@frm2.tum.de
Jan Spallek	PH1, 2341	14515	14724	jan.spallek@frm2.tum.de
Marein Rahn	PH1, 2341	14253	14724	marein.rahn@frm2.tum.de
Christoph Reitinger	PH1, 2367	12512	14724	christoph.reitinger@frm2.tum.de
Felix Rucker	PH1, 2341	14253	14724	felix.rucker@frm2.tum.de
Martin Rutzinger	UYL 0235	14568	14620	martin.rutzinger@frm2.tum.de
Markus Strobl	PH1, 2341	14515	14724	markus.strobl@frm2.tum
Tobias Weber	UYA 0367	14641	14724	tobias.weber@frm2.tum.de
Patrick Ziegler	PH1, 2341	14253	14724	patrick.ziegler@frm2.tum.de
Samantha Zimnik	UYL 0230	12137	14620	samantha.zimnik@frm2.tum.de

## Technical Personnel

Name	Room	Phone	Fax	Email
Rainer Bierbaum (FRM II)	RESEDA	10751	14874	rainer.bierbaum@frm2.tum.de
Stefan Giemsa (Uni Köln)	UYA 0342	14737	14724	stefan.giemsa@frm2.tum.de
Andreas Mantwill		14887		andreas.mantwill@frm2.tum.de
Gabriel Reingen	PH 1, 1321	12656		
Barbara Russ	PH 1, 2203	14717	14724	barbara.russ@frm2.tum.de
Reinhard Schwikowski (FRM II)	UYH 0336	14915	14989	reinhard.schwikowski@frm2.tum.de

## Guests

Name	Room	Phone	Fax	Email
Dr. Roland Gähler		+33-476-207189	+33-476-483906	gahler@ill.fr
Dr. Thomas Keller	RS 106	12164	13776	thomas.keller@frm2.tum.de

## Professors Emeriti

Name	Room	Phone	Fax	Email
Prof. Dr. emerit.	FRM-II UBA 0325	12150	12191	klaus.boening@frm2.tum.de
Klaus Böning				
Prof. Dr. emerit.	PH 1, 2281	12183	14724	wglaeser@ph.tum.de
Wolfgang Gläser				
Prof. Dr. emerit.	PH 1, 2281	12183	14724	klaus.schreckenbach@frm2.tum.de
Klaus Schreckenbach				

## Alumni

Name	Group	Email
Dr. Thomas Hils	Hils Consult GmbH, Ing.-Büro für Bauphysik	info@hils-consult.de
Dr. Martin Stadlbauer	MTU Aero Engines	martin.stadlbauer@mtu.de
Dr. Marc Janoschek	Condensed Matter and Magnet Science Group, Los Alamos National Laboratory	mjanoschek@lanl.gov
Dr. Sebastian Mühlbauer	FRM II - SANS-1	sebastian.muehlbauer@frm2.tum.de
Dr. Stefan Legl	Ter Meer, Steinmeister & Partner GbR	legl@termeer.de
Dr. Andreas Neubauer	Bundesanstalt für Materialforschung und -prüfung	andreas.neubauer@bam.de
Dr. Florian Jonietz	Areva	florian.jonietz@frm2.tum.de
Dr. Johannes Brunner	TIS innovation park	johannes.brunner@tis.bz.it

## Facilities

### FRM II Instruments

Instrument	Room	Phone	Email
Antares	Experimental hall	14815	burkhard.schillinger@frm2.tum.de
MIRA	Neutron guide hall	14877	robert.georgii@frm2.tum.de
NEPOMUC	Experimental hall	14774	christoph.hugenschmidt@frm2.tum.de
Panda	Experimental hall	14869	astrid.schneidewind@frm2.tum.de
Reseda	Neutron guide hall	14874	wolfgang.haeussler@frm2.tum.de

### E21 Laboratories

Laboratory	Room	Phone
Crystal laboratory	PH 1, 2362	14721
ADR laboratory	PH 1, 1752	14723
Magnet laboratory	PH 1, 1742	14762
X-ray laboratory	PH 1, 2173	14719
VSM laboratory	PH 1, 2352	12579
PPMS laboratory	PH 1, 2361	14738
Seminar room	PH 1, 2224	14736

## Group Photo



- |                     |                       |                     |                          |
|---------------------|-----------------------|---------------------|--------------------------|
| (1) A. Regnat       | (13) W. Kreuzpaintner | (25) M. Tischler    | (37) M. Wagner           |
| (2) B. Rienäcker    | (14) S. Vohburger     | (26) C. Pfeiderer   | (38) C. Morkel           |
| (3) T. Gigl         | (15) H. Ceeh          | (27) D. Bausenwein  | (39) M. Rahn             |
| (4) C. Piochacz     | (16) M. Reiner        | (28) R. Ritz        | (40) B. Schillinger      |
| (5) C. Hugenschmidt | (17) J.-A. Weber      | (29) T. Reimann     | (41) M. Schulz           |
| (6) S. Zimmnik      | (18) F. Rucker        | (30) C. Franz       | (42) M. Seifert          |
| (7) A. Chacon       | (19) A. Mantwill      | (31) M. Strobl      | (43) P. Böni             |
| (8) R. Schwikowski  | (20) A. Paul          | (32) W. Häußler     | (44) T. Vannieuwenhuysse |
| (9) S. Mayr         | (21) A. Bauer         | (33) G. Brandl      | (45) R. Georgii          |
| (10) S. Dunsiger    | (22) M. Gangl         | (34) A. Mühlberg    | (46) K. Seemann          |
| (11) G. Benka       | (23) C. Krey          | (35) J. Spallek     | (47) T. Adams            |
| (12) B. Wiedemann   | (24) F. Lippert       | (36) J. Kindervater |                          |